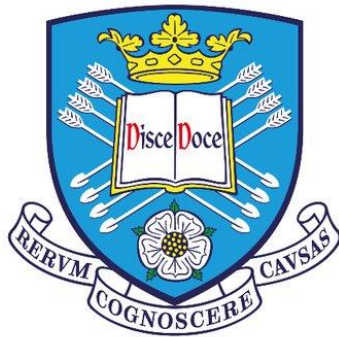


Mitochondrial dysfunction in LRRK2-G2019S Parkinson's disease



Ruby Mae Macdonald

Thesis submitted for the degree of Doctor of Philosophy (PhD)

December 2020

Sheffield Institute for Translational Neuroscience

The University of Sheffield

Abstract

Parkinson's disease (PD) is a progressive, neurodegenerative, motor disorder affecting around 1% of the over 60 population. Leucine-Rich Repeat Kinase 2 (LRRK2) mutations are the most common cause of familial PD and have been associated with mitochondrial dysfunction. For example, our research group has previously found reduced ATP levels and mitochondrial complex IV activity in patient fibroblasts. We wanted to investigate these mitochondrial abnormalities in more detail in both patient fibroblasts and a dopaminergic (DA) neuron-like model derived from induced neuronal progenitor cells (iNPCs). We hypothesised that mitochondrial deficiencies are present in both fibroblasts and a neuron-like cell model, and that complex IV assembly is affected, leading to reduced mitochondrial functionality. We measured mitochondrial function and morphology in LRRK2-G2019S manifesting, non-manifesting, and control fibroblasts, as well as LRRK2-G2019S and control iNPC-derived DA neuron-like cells. We assessed ATP levels, mitochondrial membrane potential, mitochondrial and cytosolic reactive oxygen species, and mitochondrial and cytosolic copper. We also assessed protein expression levels of mitochondrial morphology factors, OPA1 and DRP1, mitochondrial complex subunits, and mitochondrial complex assembly factors, BCS1L and SCO2 in fibroblasts. We found reduced ATP levels in some LRRK2-G2019S fibroblast cell lines as well as changes in ATP throughout the differentiation in the LRRK2-G2019S iNPC-derived neuron-like cells. We also found a significant reduction in protein expression of complex IV assembly factor SCO2, which is involved in copper insertion into complex IV in both LRRK2-G2019S manifesting fibroblasts and the LRRK2-G2019S iNPC-derived neuron-like cell model. We found changes in labile copper levels in the LRRK2-G2019S iNPC-derived neuron-like cell model. This data supports our hypothesis that mitochondrial deficiencies are present in both patient fibroblasts and iNPC-derived DA neuron-like cells and that assembly of complex IV may play a role in this.

Acknowledgements

There are many people that I would like to thank for their support during my PhD.

Firstly, and foremostly, I would like to thank my primary supervisor Dr Heather Mortiboys. Heather is not only a brilliant scientist but a fantastically supportive mentor. Her dedication is second to none and I couldn't have asked for a better supervisor. Heather believed in me when I did not believe in myself and I will forever be grateful for her support throughout my PhD journey. I would also like to thank my secondary supervisor Professor Oliver Bandmann, for his experience, guidance and encouragement throughout my PhD. Oliver has always been very positive about my work and is a fantastic clinician and scientist. I express my gratitude to both the University of Sheffield and the Rosetrees Trust for the funding of this project.

I am very grateful to the participants who donated their skin biopsies, without which this research would not have been possible, and our collaborators in Norway, Professor Jan Aasly and Professor Gunnar Brønstad, for their provision of these. I would also like to thank our collaborators in Australia and the USA, Professor Elizabeth New and Professor Christopher Chang, for providing live cell imaging probes which have been vital for this project.

Thank you to the past and present members of the Mortiboys lab for their scientific support and for being a pleasure to work with. In particular, Aurelie Schwartzenruber, Christopher Hastings, Katy Barnes, Simon Bell and Camilla Boschian. I will look back on our times both inside and outside the lab fondly, from playing cheesy music in tissue culture, to discussing science at the pub, to playing board games. I would also like to thank previous MSc students

Harry Cooper and Andre Djalalvandi, and summer placement student Olivia Cracknell for their support in this project.

I would like to thank those at the Sheffield Institute for Translational Neuroscience who supported me during my PhD, in particular, Chloe Allen and Noemi Gatto for their continuing friendship and support. I would also like to thank my childhood friends Eve Ousby and Laura Lovelock for always being there for me. Finishing writing my thesis during a global pandemic has not been the easiest and they always lifted my spirits.

I would not have been able to complete this journey without the support of my family. As well as making sure I that was doing ok, they always asked about my 'babies', i.e. the cells I was growing. My family mean more to me than I can ever express.

And last, but certainly not least, I would like to thank my husband Sam. Although we were living in different cities while completing lab work, we went through the highs and lows of the PhD together. He is a constant source of support, love and inspiration, and I will forever be thankful to have him by my side.

I dedicate this thesis to my Grandad Len, the bravest man I know.

Table of contents

| | |
|---|-------------|
| Abstract | i |
| Acknowledgements | ii |
| Table of contents | iv |
| List of figures | ix |
| List of tables | xii |
| List of abbreviations | xiii |
| Chapter 1 Introduction | 1 |
| 1.1 Mitochondrial biology | 1 |
| 1.1.1 History and structure of the mitochondria..... | 1 |
| 1.1.2 Oxidative phosphorylation | 2 |
| 1.1.3 Oxidative phosphorylation: Complex I and II..... | 4 |
| 1.1.4 Oxidative phosphorylation: Complex III..... | 4 |
| 1.1.5 Oxidative phosphorylation: Complex IV | 5 |
| 1.1.6 Oxidative phosphorylation: Complex V | 6 |
| 1.1.7 Mitochondrial complex assembly | 6 |
| 1.1.8 Mitochondrial complex assembly: Complex I | 9 |
| 1.1.9 Mitochondrial complex assembly: Complex II | 10 |
| 1.1.10 Mitochondrial complex assembly: Complex III..... | 11 |
| 1.1.11 Mitochondrial complex assembly: Complex IV | 12 |
| 1.1.12 Mitochondrial complex assembly: Complex V | 13 |
| 1.1.13 Other mitochondrial functions..... | 14 |
| 1.1.14 Mitochondrial fusion and fission | 14 |
| 1.1.15 Mitophagy | 16 |
| 1.2 Parkinson's disease..... | 17 |
| 1.2.1 Clinical characteristics | 17 |

| | | |
|------------------|---|-----------|
| 1.2.2 | Pathology | 18 |
| 1.2.3 | Treatment of Parkinson's disease..... | 21 |
| 1.2.4 | Genetic forms of Parkinson's disease..... | 21 |
| 1.2.5 | Structure of LRRK2 | 22 |
| 1.2.6 | LRRK2 non-mitochondrial function and dysfunction..... | 25 |
| 1.3 | Mitochondria and Parkinson's disease..... | 26 |
| 1.3.1 | Sporadic Parkinson's disease..... | 26 |
| 1.3.2 | Familial Parkinson's disease..... | 27 |
| 1.3.3 | LRRK2 Parkinson's disease | 30 |
| 1.3.4 | LRRK2 PD treatments | 31 |
| 1.3.5 | Treatments targeting mitochondrial dysfunction in PD | 32 |
| 1.4 | Project rationale and aims | 33 |
| Chapter 2 | Materials and methods..... | 35 |
| 2.1. | Patient and control lines used..... | 35 |
| 2.2. | Cell Culture..... | 37 |
| 2.2.1. | Cell culture of fibroblasts | 37 |
| 2.2.2. | Generation of induced neural progenitor cells..... | 37 |
| 2.2.3. | iNPC cell culture | 38 |
| 2.2.4. | iNPC-derived DA neuron-like cell model differentiation protocol | 38 |
| 2.3. | ATP assays | 41 |
| 2.4. | Mitochondrial membrane potential and lysosome assays | 42 |
| 2.5. | Copper and reactive oxygen species probes | 43 |
| 2.6. | Drug treatments..... | 44 |
| 2.7. | Western blotting..... | 45 |
| 2.7.1. | Protein quantification | 45 |
| 2.7.2. | Preparing and running gels..... | 47 |
| 2.7.3. | Transfer | 48 |

| | | |
|------------------|---|----|
| 2.7.4. | Antibodies..... | 48 |
| 2.7.5. | Densitometry | 49 |
| 2.8. | Brightfield imaging of iNPC-derived DA neuron-like cells..... | 51 |
| 2.9. | Immunofluorescent staining | 51 |
| 2.10. | siRNA knockdown experiments..... | 52 |
| 2.11. | Opera Phenix image analysis..... | 53 |
| 2.12. | Statistical analysis..... | 54 |
| | | |
| Chapter 3 | Analysis of mitochondrial dysfunction in LRRK2-G2019S fibroblasts | |
| | 56 | |
| 3.1 | Introduction | 56 |
| 3.1.1 | Aims and objectives..... | 57 |
| 3.2 | Results | 58 |
| 3.2.1 | ATP levels in LRRK2-G2019S manifesting, non-manifesting, and control fibroblasts | 58 |
| 3.2.2. | Mitochondrial membrane potential in LRRK2-G2019S manifesting, non-manifesting, and control fibroblasts..... | 61 |
| 3.2.3. | Mitochondrial and cytosolic reactive oxygen species | 63 |
| 3.2.4. | Protein expression of mitochondrial complex subunits..... | 68 |
| 3.2.5. | Protein expression of complex III and IV assembly factors | 70 |
| 3.2.6. | Assessment of mitochondrial morphology..... | 72 |
| 3.2.7. | Protein expression of mitochondrial morphology and fission/fusion factors | 75 |
| 3.2.8. | DRP1 localisation | 78 |
| 3.2.9. | Potential mechanisms of UDCA and UCA | 83 |
| 3.3. | Discussion | 87 |
| 3.3.2. | ATP levels | 87 |
| 3.3.3. | MMP..... | 89 |
| 3.3.4. | ROS | 89 |

| | | |
|------------------|---|------------|
| 3.3.5. | Mitochondrial complexes | 90 |
| 3.3.6. | Mitochondrial morphology..... | 92 |
| 3.3.7. | Future studies..... | 93 |
| Chapter 4 | Assessing mitochondrial function in LRRK2-G2019S induced neural progenitor cell derived dopaminergic neuron-like cells | 96 |
| 4.1. | Background | 96 |
| 4.1.1. | Aims and objectives..... | 98 |
| 4.2. | Results | 98 |
| 4.2.1. | iNPC-derived DA neuron-like cell characterisation..... | 98 |
| 4.2.2. | ATP levels throughout differentiation | 101 |
| 4.2.3. | Mitochondrial membrane potential and mitochondrial number | 105 |
| 4.2.4. | Lysosomal phenotype and mitophagy..... | 108 |
| 4.2.5. | Mitochondrial and cytosolic reactive oxygen species | 110 |
| 4.3. | Discussion | 116 |
| Chapter 5 | Assessing mechanisms underlying mitochondrial complex IV deficiency in LRRK2-G2019S manifesting cells | 120 |
| 5.1. | Introduction..... | 120 |
| 5.1.1. | Complex IV assembly and the role of SCO2..... | 120 |
| 5.1.2. | Aims | 122 |
| 5.2. | Results | 122 |
| 5.2.1. | SCO2 expression in LRRK2-G2019S iNPC-derived DA neuron-like cells 122 | |
| 5.2.2. | SCO2 knockdown optimisation | 124 |
| 5.2.3. | Mitochondrial copper in fibroblasts and iNPC-derived DA neuron-like cells 125 | |
| 5.2.4. | Cytosolic copper in fibroblasts and iNPC-derived DA neuron-like cells .. | 129 |
| 5.2.5. | Other mitochondrial complex IV assembly factors | 131 |
| 5.3. | Discussion | 133 |

| | | |
|-----------|---|------------|
| 5.3.1. | LRRK2-G2019S SCO2 protein expression | 133 |
| 5.3.2. | LRRK2-SCO2 interaction..... | 134 |
| 5.3.3. | SCO2 deficient patients and conditions associated with copper dyshomeostasis | 134 |
| 5.3.4. | Copper in PD..... | 135 |
| 5.3.5. | Methods for assessing copper in cells | 137 |
| 5.3.6. | Future directions..... | 138 |
| 6. | General Discussion | 140 |
| | References | 145 |
| | Appendix A..... | 188 |
| | Appendix B..... | 196 |

List of figures

| | |
|--|----|
| Figure 1.1. Structure of the mitochondria..... | 2 |
| Figure 1.2. Oxidative phosphorylation process..... | 3 |
| Figure 1.3. Mitochondrial fission and fusion..... | 16 |
| Figure 1.4. Parkinson's disease pathology..... | 20 |
| Figure 1.5. Domain structures of LRRK2..... | 22 |
| Figure 2.1. Neuron-like cell model differentiation protocol..... | 40 |
| Figure 2.2. Example image of mitochondrial segmentation and DRP1 'spots' found within the mitochondria..... | 54 |
| Figure 3.1. ATP levels in LRRK2-G2019S manifesting, non-manifesting and control fibroblasts..... | 60 |
| Figure 3.2. Mitochondrial membrane potential in LRRK2-G2019S manifesting, non-manifesting and control fibroblasts..... | 63 |
| Figure 3.3. Mitochondrial reactive oxygen species levels in LRRK2-G2019S manifesting, non-manifesting and control fibroblasts..... | 66 |
| Figure 3.4. Cytosolic reactive oxygen species levels in LRRK2-G2019S manifesting, non-manifesting and control fibroblasts..... | 67 |
| Figure 3.5. Protein expression of OXPHOS complex subunits in LRRK2-G2019S manifesting, non-manifesting and control fibroblasts..... | 69 |
| Figure 3.6. Protein expression of BCS1L in LRRK2-G2019S manifesting, non-manifesting and control fibroblasts..... | 71 |
| Figure 3.7. Protein expression of SCO2 in LRRK2-G2019S manifesting, non-manifesting and control fibroblasts..... | 72 |
| Figure 3.8. Mitochondrial morphology parameters from TMRM staining in LRRK2-G2019S manifesting, non-manifesting and control fibroblasts..... | 74 |
| Figure 3.9. Protein expression of OPA1 in LRRK2-G2019S manifesting, non-manifesting and control fibroblasts..... | 76 |
| Figure 3.10. Protein expression of DRP1 in LRRK2-G2019S manifesting, non-manifesting and control fibroblasts..... | 77 |
| Figure 3.11. DRP1 localisation staining of LRRK2-G2019S manifesting, non-manifesting and control fibroblasts..... | 81 |
| Figure 3.12. Quantification of DRP1 staining..... | 82 |

| | |
|--|-----|
| Figure 3.13. Protein expression of TSPO in LRRK2-G2019S manifesting, non-manifesting and control fibroblasts. | 84 |
| Figure 3.14. Protein expression of SCO2, BCS1L and OPA1 in UDCA and UCA treated fibroblasts..... | 86 |
| Figure 3.15. Effect of UDCA and UCA on mitochondrial and cytosolic reactive oxygen species in LRRK2-G2019S manifesting, non-manifesting and control fibroblasts. | 86 |
| Figure 4.1. Brightfield imaging of LRRK2-G2019S manifesting and control iNPC-derived DA neurons during the third stage of differentiation. | 100 |
| Figure 4.2. Tuj1 and TH staining of LRRK2-G2019S manifesting and control iNPC-derived DA neuron-like cells at day 27 of neuronal differentiation. | 101 |
| Figure 4.3. ATP levels of LRRK2-G2019S manifesting and control iNPC-derived DA neuron-like cells throughout differentiation. | 103 |
| Figure 4.4. ATP levels of LRRK2-G2019S manifesting and control iNPC-derived DA neuron-like cells in different media types..... | 104 |
| Figure 4.5. TMRM staining of LRRK2-G2019S manifesting and control iNPC-derived DA neuron-like cells throughout neuronal differentiation..... | 106 |
| Figure 4.6. Quantification of mitochondrial characteristics of LRRK2-G2019S manifesting and control iNPC-derived DA neuron-like cells throughout neuronal differentiation. | 107 |
| Figure 4.7. LysoTracker staining of LRRK2-G2019S manifesting and control iNPC-derived DA neuron-like cells throughout neuronal differentiation..... | 109 |
| Figure 4.8. Quantification of lysosome characteristics of LRRK2-G2019S manifesting and control iNPC-derived DA neuron-like cells throughout neuronal differentiation. | 110 |
| Figure 4.9. Mitochondrial reactive oxygen species probe NpFR2 staining of LRRK2-G2019S manifesting and control iNPC-derived DA neuron-like cells throughout neuronal differentiation..... | 112 |
| Figure 4.10. Quantification of mitochondrial reactive oxygen species probe NpFR2 staining of LRRK2-G2019S manifesting and control iNPC-derived DA neuron-like cells throughout neuronal differentiation..... | 113 |
| Figure 4.11. Mitochondrial reactive oxygen species probe FRR2 staining of LRRK2-G2019S manifesting and control iNPC-derived DA neuron-like cells at day 27 of neuronal differentiation..... | 114 |
| Figure 4.12. Cytosolic reactive oxygen species probe NpFR1 staining of LRRK2-G2019S manifesting and control iNPC-derived DA neuron-like cells at day 27 of neuronal differentiation..... | 115 |

| | |
|---|-----|
| Figure 5.1. Complex IV assembly model. | 121 |
| Figure 5.2. The role of SCO2 in CuA incorporation..... | 121 |
| Figure 5.3. SCO2 protein expression in LRRK2-G2019S and control iNPC-derived DA neuron-like cells. | 123 |
| Figure 5.4. SCO2 knockdown optimisation in control iNPC-derived DA neuron-like cells. | 124 |
| Figure 5.5. Mitochondrial copper in LRRK2-G2019S manifesting, non-manifesting and control fibroblasts. | 126 |
| Figure 5.6. Mitochondrial copper in LRRK2-G2019S manifesting and control iNPC-derived DA neuron-like cells. | 128 |
| Figure 5.7. Quantification of mitochondrial copper in LRRK2-G2019S manifesting and control iNPC-derived DA neuron-like cells..... | 129 |
| Figure 5.8. Cytosolic copper in LRRK2-G2019S manifesting, non-manifesting and control fibroblasts..... | 130 |
| Figure 5.9. Cytosolic copper in LRRK2-G2019S manifesting and control iNPC-derived DA neuron-like cells. | 131 |
| Figure 5.10. COX15 protein expression in LRRK2-G2019S manifesting, non-manifesting and control fibroblasts. | 132 |

List of tables

| | |
|--|----|
| Table 1.1. Mitochondrial complex subunits/assembly factors and disease associated mutations. | 7 |
| Table 2.1. Details of fibroblast lines generated from LRRK2 G2019S manifesting, LRRK2 G2019S non-manifesting, and control patient biopsies. | 35 |
| Table 2.2. Details of LRRK2-G2019S manifesting and control fibroblast lines used to generate induced neural progenitor cells. | 38 |
| Table 2.3 4x sample buffer | 46 |
| Table 2.4 Resolving gel (12%) | 46 |
| Table 2.5 Stacking gel | 46 |
| Table 2.6 Running buffer (10 L)..... | 47 |
| Table 2.7 Transfer buffer (1 L)..... | 47 |
| Table 2.8 TBST (10 L)..... | 47 |
| Table 2.9 Antibodies used for western blotting | 50 |
| Table 2.10. Primary antibodies used for immunofluorescent staining | 52 |

List of abbreviations

| | |
|---------------|--|
| APS | Ammonium persulfate |
| ATP | Adenosine triphosphate |
| BCS1L | Ubiquinol-cytochrome c reductase complex chaperone |
| BDNF | Brain-derived neurotrophic factor |
| BSA | Bovine serum albumin |
| CCCP | Carbonyl cyanide m-chlorophenyl hydrazone |
| DA | Dopaminergic |
| DMEM | Dulbecco's Modified Eagle Medium |
| DRP1 | Dynamin related protein 1 |
| DTT | Dithiothreitol |
| DxA | Density x area |
| ECL | Enhanced chemiluminescence |
| FBS | Foetal bovine serum |
| FGF | Fibroblast growth factor |
| GDNF | Glial cell line-derived neurotrophic factor |
| HBSS | Hank's balanced salt solution |
| HRP | Horseradish peroxidase |
| iNPC | Induced neural progenitor cell |
| LRRK2 | Leucine-rich repeat kinase 2 |
| MEM | Minimum essential medium |
| MMP | Mitochondrial membrane potential |
| OPA1 | OPA1 mitochondrial dynamin like GTPase |
| OXPHOS | Oxidative phosphorylation |

| | |
|--------------------------|---|
| PBS | Phosphate-buffered saline |
| PBST | Phosphate-buffered saline with Tween 20 |
| PD | Parkinson's disease |
| PVDF | Polyvinylidene difluoride |
| RIPA | Radioimmunoprecipitation assay |
| SAG | Smoothened Agonist |
| SCO2 | SCO cytochrome c oxidase assembly protein 2 |
| SDS | Sodium dodecyl sulfate |
| SDS-PAGE | Sodium dodecyl sulfate polyacrylamide gel electrophoresis |
| TBST | Tris-buffered saline with Tween 20 |
| TEMED | Tetramethylethylenediamine |
| TGF-B₃ | Transforming growth factor-beta 3 |
| TMRM | Tetramethylrhodamine methyl ester |
| TSPO | Translocator protein |
| UCA | Ursocholic acid |
| UDCA | Ursodeoxycholic acid |

Chapter 1 **Introduction**

This chapter includes material from sections written by the author that have been published in a review paper (Mortiboys *et al.*, 2018). The co-authors of the paper and the journal have given permission for the text to be used in this thesis (**Appendix A**).

1.1 Mitochondrial biology

1.1.1 History and structure of the mitochondria

The earliest descriptions of mitochondria-like structures date to the 1840s. In 1890 Richard Altmann recognised the ubiquitous nature of these structures and named them ‘bioblasts’. The term ‘mitochondrion’ was first coined by Carl Benda in 1898, originating from the Greek ‘mitos’ (thread) and ‘chondros’ (granule) (Ernster and Schatz, 1981). The most widely accepted theory of mitochondrial evolution, the endosymbiotic theory, suggests that mitochondria evolved from bacterial progenitors which were endocytosed by early eukaryotic cells (Gray, 2012).

The development of electron microscopy in 1931 allowed a clearer insight into the structure of the mitochondria. The mitochondria are a double membraned structure consisting of both an outer and inner mitochondrial membrane (**Figure 1.1.**). The area between these is named the intermembrane space. The invaginations of the inner mitochondria membrane - the cristae - contain the protein complexes of the electron transport chain. The cristae lumen contains large amounts of the electron carrier cytochrome c, which is involved in oxidative phosphorylation. Cytochrome c also triggers apoptosis if released into the cytoplasm. The mitochondrial matrix has a high pH and is involved in many fundamental processes such

as; DNA replication, transcription, and protein biosynthesis, as well as the enzymatic reactions of the citric acid cycle (Kühlbrandt, 2015).

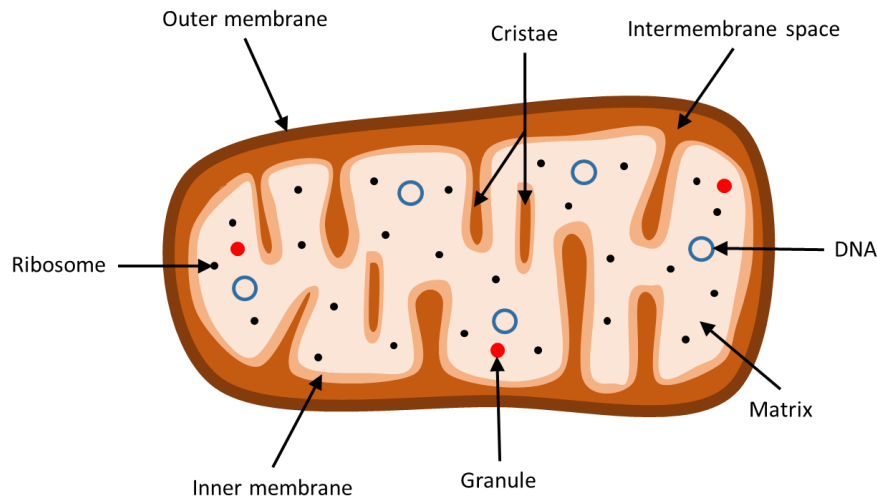


Figure 1.1. Structure of the mitochondria.

Diagram of the ultrastructural features of the mitochondria.

1.1.2 Oxidative phosphorylation

Although small amounts of ATP are produced by glycolysis in the cytoplasm, oxidative phosphorylation within the mitochondria produces the majority of ATP within the cell. In mammalian cells, there are five protein complexes that carry out this process, named Complex I-V (Hames and Hooper, 1997). The basic process of oxidative phosphorylation is the transfer of electrons through the electron transport chain. The energy from the electron movement is used to pump protons from the mitochondrial matrix into the intermembrane space. The proton gradient then flows back into the mitochondrial matrix through Complex V, also known as ATP synthase, leading to the mechanical turning of its components. This mechanical energy then drives ATP synthesis (Hames and Hooper, 1997; Berg, Tymoczko and Stryer, 2012). **Figure 1.2.** describes this process in more detail.

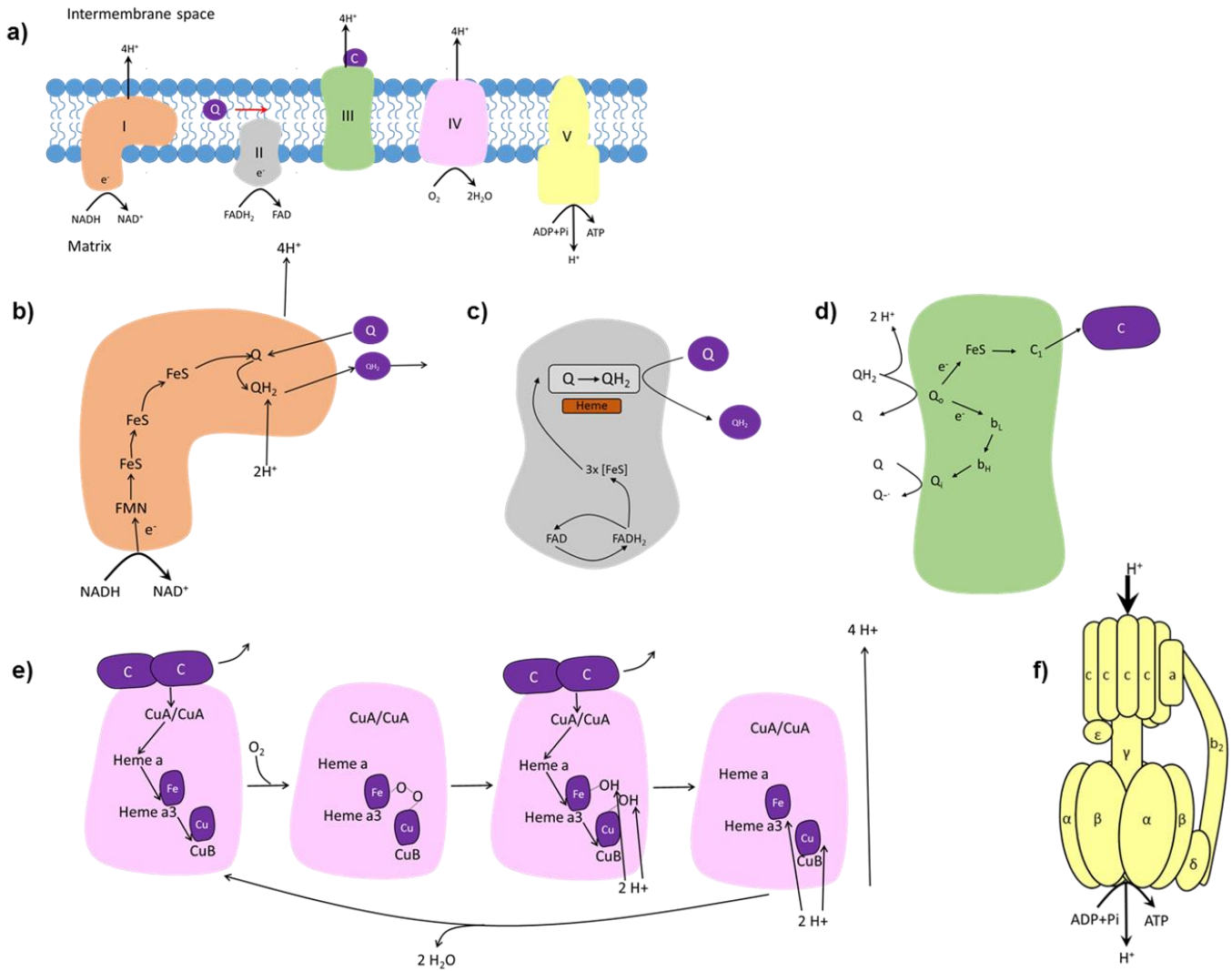


Figure 1.2. Oxidative phosphorylation process.

(a) the oxidative phosphorylation complexes embedded within the inner mitochondrial membrane. (b) complex I electron transport (c) complex II electron transport (d) complex III electron transport. A second ubiquinol binds to the Q0 complex III site with the electrons being transferred in the same process apart from the second electron binds to the semiquinone radical anion at the Q0 site after being transferred by cytochrome bH (e) complex IV electron transport (f) complex V ATP synthesis. Ubiquinone (Q); ubiquinol (QH₂), cytochrome c (C) cytochrome b low affinity (b_L) cytochrome b high affinity (b_H). Adapted from (Hames and Hooper, 1997; Berg, Tymoczko and Stryer, 2012)

1.1.3 Oxidative phosphorylation: Complex I and II

Complex I, also known as NADH-Q-oxidoreductase, oxidises nicotinamide adenine dinucleotide (NADH) to NAD⁺, resulting in two electrons being transported to flavin mononucleotide (Hames and Hooper, 1997; Berg, Tymoczko and Stryer, 2012). Next, the electrons are transferred to a series of iron-sulfur clusters, before being passed to ubiquinone which becomes ubiquinol (Lenaz *et al.*, 2006). This process results in the transfer of four hydrogen ions into the intermembrane space. Complex I receives its NADH from both glycolysis and the Krebs cycle, with the oxidation of NADH to NAD⁺ recycling the molecule for re-use in these processes (Hames and Hooper, 1997; Berg, Tymoczko and Stryer, 2012). Next, complex II, also known as succinate-Q reductase, oxidises flavin adenine dinucleotide (FADH₂) to FAD. Interestingly, complex II contains succinate dehydrogenase (SDH), an enzyme essential to the Krebs cycle, which reduces FAD to FADH₂ (Wojtovich *et al.*, 2013). Therefore, there is a continuous oxidation and reduction of FADH₂ and FAD at complex II. Similar to complex I, complex II also contains iron-sulfur clusters to which the electrons are passed before being transferred to ubiquinone (Hames and Hooper, 1997; Berg, Tymoczko and Stryer, 2012). However, unlike complex I, complex II is not a proton pump (Wojtovich *et al.*, 2013).

1.1.4 Oxidative phosphorylation: Complex III

The primary function of complex III, also known as Q-cytochrome c oxidoreductase, is to transfer electrons from the electron carrier, ubiquinol, to another electron carrier, cytochrome c. A fundamental difference between ubiquinol and cytochromes is that ubiquinol is a two electron carrier, whilst cytochromes can only carry one electron (Hames and Hooper, 1997). Therefore, ubiquinol binding occurs as a two-stage process. First, ubiquinol binds to the Q₀ site on complex III and donates its two electrons, thereby releasing

two hydrogen ions into the intermembrane space. One electron is donated to an iron-sulfur complex, transferred to cytochrome c1, and then to cytochrome c. The other electron is transferred to cytochrome b low affinity (bL), then cytochrome b high affinity (bH), before binding to an additional ubiquinone at the complex III Q1 site. This electron binding causes the ubiquinol to become a semiquinone radical anion (Hames and Hooper, 1997; Berg, Tymoczko and Stryer, 2012). A second ubiquinol binds to the Q0 complex III site with the electrons being transferred in the same process as previously described, apart from the second electron binds to the semiquinone radical anion at the Q0 site after being transferred by cytochrome bH. This allows the semiquinone to take up two hydrogen ions from the mitochondrial matrix to become ubiquinol (Hames and Hooper, 1997; Berg, Tymoczko and Stryer, 2012).

1.1.5 Oxidative phosphorylation: Complex IV

In complex IV, also known as cytochrome c oxidase, oxygen is the final electron acceptor (Papa *et al.*, 2012). Here, two cytochrome c bind and transfer their electrons through the following molecules; CuA/CuA, to heme a, to heme a3 to CuB, one electron stopping at heme a3 and the other at CuB. Oxygen then accepts the electrons and forms a peroxide bridge between heme a3 and CuB (Hames and Hooper, 1997; Berg, Tymoczko and Stryer, 2012). Next, two more cytochrome c bind to complex IV and the ion-oxygen groups are reduced to OH groups. Finally, two more hydrogen ions from the mitochondrial matrix react allowing the release of two water molecules (Hames and Hooper, 1997; Berg, Tymoczko and Stryer, 2012). Overall, four electrons from cytochrome c and four hydrogen ions allow molecular oxygen to form two water molecules, and a net of four hydrogen ions are pumped into the intermembrane space (Hames and Hooper, 1997; Berg, Tymoczko and Stryer, 2012).

1.1.6 Oxidative phosphorylation: Complex V

Proton-motive force, the sum of the pH gradient and the mitochondrial membrane potential produced by the electron transport chain, drives complex V (Hames and Hooper, 1997; Berg, Tymoczko and Stryer, 2012). Complex V contains two functional units, F1 and F0. F1 is composed of three α , three β , one γ , one δ , and one ϵ subunits, whilst F0 composes of 10-14 c subunits in a ring-like structure, and an a and two b subunits which connect F0 to F1 (Jonckheere, Smeitink and Rodenburg, 2012). As the protons flow through complex V, this causes the c ring to spin, thereby rotating the γ/ϵ stalk inside the static α/β ring. Each β subunit can bind adenosine diphosphate (ADP) and inorganic phosphate (Hames and Hooper, 1997; Berg, Tymoczko and Stryer, 2012). The mechanical energy produced by each 360° turn of the stalk allows the synthesis of three ATP molecules, the rotation speed causing the formation of over 1000 ATP molecules per second (Hames and Hooper, 1997).

1.1.7 Mitochondrial complex assembly

The different mitochondrial complex subunits are encoded either by nuclear or mitochondrial DNA. Nuclear encoded proteins are imported into the mitochondria by translocases in both the outer (TOM complex) and inner mitochondrial membranes (TIM complex) (Muro *et al.*, 2003). The mitochondria have a circular genome, which is ~16.6 kb in size, contains a heavy and light strand, and is usually maternally inherited in humans (Chinnery and Hudson, 2013). Mitochondrial DNA encodes 37 genes; 13 protein subunits of the electron transport chain, 22 transfer RNA, and 2 ribosomal RNA. Complex II is the only complex of the electron transport chain with purely nuclear encoded subunits (Chinnery and Hudson, 2013). The different mitochondrial subunits and assembly factor mutations associated with disease are summarised in Table 1.1.

Table 1.1. Mitochondrial complex subunits/assembly factors and disease associated mutations.

Information compiled from <https://omim.org/> (McKusick-Nathans Institute of Genetic Medicine, Johns Hopkins University) and Fernández-Vizarra et al. 2009. Leber hereditary optic neuropathy (LHON), mitochondrial encephalomyopathy, lactic acidosis, and stroke-like episodes (MELAS), growth retardation, aminoaciduria, cholestasis, iron overload, lactic acidosis, and early death (GRACILE).

| | | Number | Known disease associated mutations |
|-------------------|--------------------------------|--------|---|
| Complex I | Mitochondrial encoded subunits | 7 | Complex I deficiency – NDUFV1 NDUFV2 NDUFS1 NDUFS2 NDUFS3 NDUFS4 NDUFS6 NDUFS7 |
| | Nuclear encoded subunits | 37 | NDUFA1 NDUFB11 B17.2L HRPAP20 C20ORF7 NUBPL NDUFAF1 TMEM126B |
| | Assembly factors | ~13 | NDUFS8 NDUFA2 NDUFA11 NDUFAF3 NDUFA10 NDUFB3 NDUFB9 MTND1 MTND2 MTND3 MTND4 MTND4 MTND6 |
| | | | Most patients present with LHON, Leigh syndrome, MELAS |
| Complex II | Mitochondrial encoded subunits | 0 | Complex II deficiency – |
| | Nuclear encoded subunits | 4 | SDHA SDHD |
| | Assembly factors | ~4 | SDHAF1 |

| | | | |
|--------------------|---|-------------------------------|---|
| | | | Variable phenotype, with some cases involving multiple systems, whilst others involve cardiac or muscle systems |
| Complex III | <p>Mitochondrial encoded subunits</p> <p>Nuclear encoded subunits</p> <p>Assembly factors</p> | <p>1</p> <p>10</p> <p>~5</p> | <p>Complex III deficiency –</p> <p>BCS1L</p> <p>MTCYB</p> <p>TTC19</p> <p>UQCRB</p> <p>UQCRQ</p> <p>UQCRC2</p> <p>CYC1</p> <p>UQCC2</p> <p>LYRM7</p> <p>UQCC3</p> <p>Patients have presented with GRACILE syndrome, Björnstad syndrome, myopathy with ragged red fibers, Leigh syndrome</p> |
| Complex IV | <p>Mitochondrial encoded subunits</p> <p>Nuclear encoded subunits</p> <p>Assembly factors</p> | <p>3</p> <p>10</p> <p>~20</p> | <p>Complex IV deficiency –</p> <p>MTCO1</p> <p>MTCO2</p> <p>MTCO3</p> <p>COX10</p> <p>COX6B1</p> <p>SCO1</p> <p>C12ORF62</p> <p>COX20</p> |

| | | | |
|------------------|--|---------------|--|
| | | | COX8A COA3 SCO2 COX15 COA5 COA6 SURF1 LRPPRC Patients present with fatal infantile cardioencephalomyopathy, Leigh syndrome, French Canadian Leigh syndrome |
| Complex V | Mitochondrial encoded subunits Nuclear encoded subunits Assembly factors | 2 14 ~2 | Complex V deficiency – ATPAF2 TMEM70 ATP5E ATP5A1 MTATP6 MTATP8 Patients present with neonatal-onset hypotonia, lactic acidosis, hyperammonemia, hypertrophic cardiomyopathy, 3-methylglutaconic aciduria |

1.1.8 Mitochondrial complex assembly: Complex I

Complex I is the largest of the mitochondrial complexes and is 'L' shaped, with one hydrophobic arm embedded within the mitochondrial inner membrane and the other hydrophilic peripheral arm in the matrix (Hames and Hooper, 1997). The complex contains

at least 44 subunits, of which 7 are mitochondrially encoded (Murray *et al.*, 2003; Carroll *et al.*, 2006; Fernández-Vizarra, Tiranti and Zeviani, 2009). Table 1.1. shows the mitochondrial complex subunits. Complex I is composed of three functional modules; the dehydrogenase modules which oxidises NADH and the hydrogenase module which transfers electrons to ubiquinone, both of which are located in the peripheral arm, and a hydrogen ion translocation module located in the membrane arm (Fernández-Vizarra, Tiranti and Zeviani, 2009). There are two models describing complex I assembly. One model suggests that the peripheral and membrane arm sub-assemblies are formed and then joined together in the last step of assembly (Ugalde *et al.*, 2004). The other model suggests that the two arm sub-assemblies are joined before their full formation (Fernández-Vizarra, Tiranti and Zeviani, 2009). Current evidence suggests that at least 13 assembly factors, which are encoded by the nucleus, are involved in complex I formation. It is thought that more assembly factors are involved, as some patients present with a complex I deficiency but with no previously identified mutations found, suggesting that the mutations may not have been identified yet (Fernández-Vizarra, Tiranti and Zeviani, 2009).

1.1.9 Mitochondrial complex assembly: Complex II

Complex II is the smallest of the mitochondrial complexes and its subunits are encoded entirely by nuclear DNA. Complex II is composed of four subunits; the two soluble proteins SDHA (a flavoprotein) and SDHB (an iron-sulfur protein), and two membrane subunits SDHC and SDHD (Cecchini, 2003; Sun *et al.*, 2005). The SDHA protein houses the site where succinate is oxidised (Ghezzi and Zeviani, 2012). Evidence in *E.coli* suggest complex II subunit matures separately and then combined together to form the complex, though assembly in mammalian is poorly understood (Ghezzi and Zeviani, 2012). Four complex II assembly factors have been identified in humans so far, SDHAF1-4 (Ghezzi and Zeviani, 2012). However, the current complex II assembly models are based on data from yeast and

bacterial models meaning further research is needed in mammalian cells, as some assembly factors differ in their functions between organisms.

1.1.10 Mitochondrial complex assembly: Complex III

Complex III is composed of 10 nuclear-encoded subunits and one subunit encoded by the mitochondrial genome (Fernández-Vizarra, Tiranti and Zeviani, 2009). Three of the complex III subunits have been found to be involved in electron transfer; MTCYB which is encoded by mitochondrial DNA, and CYC1 and UQCRFS1 (Rieske protein) which are encoded by nuclear DNA (Fernández-Vizarra, Tiranti and Zeviani, 2009). The function of the remaining subunits remains to be fully elucidated. So far five assembly factors for human complex III have been identified, BCS1L, TTC19, LYRM7, UQCC1, and UQCC2 (Hinson *et al.*, 2007; Ghezzi and Zeviani, 2012; Sánchez *et al.*, 2013; Tucker *et al.*, 2013). Complex III assembly is not as fully defined as the other complexes. One major difference is that one of its assembly factors TTC19 has no ortholog in *S.cerevisiae*, the main model used for studying mitochondrial assembly. Additionally, mammalian mitochondria have an additional subunit compared with yeast (Fernández-Vizarra, Tiranti and Zeviani, 2009). Mutations in complex III are also very rare meaning that there are fewer complex III deficient patients to study.

The models concerning complex III assembly have been established using data from yeast, but it is thought that the process is similar in mammalian cells (Fernández-Vizarra, Tiranti and Zeviani, 2009). The first step in complex III assembly is MTCYB being released from the mitochondrial ribosomes, by the assembly factors UQCC1 and UQCC2 (Fernández-Vizarra, Tiranti and Zeviani, 2009; Tucker *et al.*, 2013). It has been shown in yeast that following this, the complex III subunits form subcomplexes, which then form a pre-complex III (Fernández-Vizarra, Tiranti and Zeviani, 2009). Rieske protein is then added to this to mature the complex. The functionally active form of complex III is a dimer and dimerization

is thought to occur before the CIII monomer has fully been completed. The last subunit to be added is UQCR11 to form a mature complex III dimer (Fernández-Vizarra, Tiranti and Zeviani, 2009).

BCS1L is the most well-studied complex III assembly, primarily because it is the most common mutation leading to complex III deficiency (Hinson *et al.*, 2007; Fernández-Vizarra, Tiranti and Zeviani, 2009). It is thought that BCS1L is involved in the later stages of complex III formation by incorporating the Rieske protein (Hinson *et al.*, 2007). TTC19 has an at present unknown function in complex III assembly.

1.1.11 Mitochondrial complex assembly: Complex IV

Complex IV is one of the most well-defined mitochondrial complexes. It consists of 13 subunits to form a heteromeric structure. MTCO1, MTCO2, and MTCO3 are encoded by the mitochondria (Fernández-Vizarra, Tiranti and Zeviani, 2009). The remaining subunits are nuclear encoded and are imported by the translocase of the inner membrane (TIM)23 complex into the mitochondria (Dennerlein and Rehling, 2015). TIM21, a subunit of TIM23, transfers early complex IV subunits to the mitochondrial translation regulation assembly intermediate of complex IV (MITRAC) (Dennerlein and Rehling, 2015). Nuclear-encoded subunits may be involved in the stabilisation of complex IV and have regulatory functions (Fernández-Vizarra, Tiranti and Zeviani, 2009). Complex IV assembly is a multiple step process requiring over 20 assembly factors. SURF1 is an essential assembly factor, with mutations linked to an accumulation of complex IV sub-assemblies (Fernández-Vizarra, Tiranti and Zeviani, 2009). Other assembly factors include COX10 and COX15, which are enzymes involved in the heme a biosynthetic pathway (Barros and Tzagoloff, 2002). In addition, the assembly factors SCO1 and SCO2 regulate the insertion of copper into complex IV, essential for MTCO1 and MTCO2 maturation (Horng *et al.*, 2005). Finally,

LRPPC is an assembly factor involved in the maturation of MTCO1 and MTCO3 mRNAs (Fernández-Vizarra, Tiranti and Zeviani, 2009).

The current model for complex IV assembly begins with MTCO1 being implanted into the inner mitochondrial membrane. This is called assembly intermediate S1 (Fernández-Vizarra, Tiranti and Zeviani, 2009). Next, assembly intermediate S2, composed of CO4 and COX5A is added. It is likely that heme a is inserted at around this stage (Fernández-Vizarra, Tiranti and Zeviani, 2009). After, SCO1 and SCO2 incorporate copper into MTCO2, which is then integrated with the nascent complex IV. It is thought that the heme a₃ and Cu_B are inserted together before MTCO2 binding. Next MTCO3 incorporation starts a cascade of most other complex IV subunits being added. The last step in complex IV assembly is its dimerisation (Fernández-Vizarra, Tiranti and Zeviani, 2009).

1.1.12 Mitochondrial complex assembly: Complex V

The basic structure of complex V has been described in the previous section of this review. Although many assembly factors have been identified in yeast, only two have been identified in humans, ATP11 and ATP12 (Ackerman, 2002; Fernández-Vizarra, Tiranti and Zeviani, 2009). These are involved in the assembly of the $\alpha\beta$ ring of the F1 module by providing a shield for the subunits' hydrophobic surfaces (Ackerman, 2002). No human assembly factors have been identified which interact with the F0 module, perhaps due to the module's high turnover, making it problematic to isolate (Fernández-Vizarra, Tiranti and Zeviani, 2009). The model of how complex V assembles in humans is not entirely clear but it is thought that the F0 and F1 are constructed separately before forming together as a mature complex V (Fernández-Vizarra, Tiranti and Zeviani, 2009).

1.1.13 Other mitochondrial functions

As well as the production of ATP, the mitochondria are involved in several other functions; such as apoptosis, reactive oxygen species (ROS) production, and calcium handling (Wang and Youle, 2009; Zorov, Juhaszova and Sollott, 2014; De Stefani, Rizzuto and Pozzan, 2016). The process of oxidative phosphorylation itself produces reactive oxygen species, which are thought to be detrimental to the cell (Auten and Davis, 2009). However, there is some recent evidence to suggest that ROS are important signalling molecules (Sies and Jones, 2020). The functions of the mitochondria have been reviewed extensively by Murphy et al. 2016.

1.1.14 Mitochondrial fusion and fission

The mitochondria are highly dynamic and are constantly undergoing fission and fusion. These dynamics are essential in regulating mitochondria number, size and cellular positioning, which can help the cell respond to things such as nutrient availability and the cell's metabolic needs (Westermann, 2010). The processes of mitochondrial fusion and fission are complex and have not been fully elucidated (**Figure 1.3.**).

One of the main proteins involved in mitochondrial fission is dynamin-related protein 1 (Drp1), also referred to as dynamin-like protein 1. Drp1 is a large GTPase which is located mainly in the cytosol and then is recruited by mitochondrial fission factor (Mff) and mitochondrial dynamics 49 and 51 (MiD49, MiD51) (Osellame *et al.*, 2016). Drp1 forms a ring-like structure around the outer mitochondrial membrane, and GTP hydrolysis further increases this constriction (Kamerkar *et al.*, 2018). The GTPase Dnm2 is then recruited and is thought to cause the scission of the mitochondria (Lee *et al.*, 2016). Inner mitochondrial membrane fission is much more poorly understood but is thought to be independent of Drp1 and precede outer mitochondrial membrane fission (Chan, 2006). Recent evidence

suggests that inner mitochondrial membrane fission may be a calcium dependent process (Cho *et al.*, 2017; Chakrabarti *et al.*, 2018).

Mfn1 and Mfn2 are involved in the fusion of the outer mitochondrial membrane and accumulate at contact areas between mitochondria. Optic atrophy 1 (OPA1) is involved in inner mitochondrial membrane fusion and has both long and short isoforms, L-OPA1 and S-OPA1 respectively, whose roles have not been fully described (Anand *et al.*, 2014). Originally it was thought that both isoforms were needed for mitochondrial fusion. But recently, it has been shown that it is indeed L-OPA1, which is tethered to the inner mitochondrial membrane, that is more important in the fusion process (Anand *et al.*, 2014). Interestingly, S-OPA1 might play a role in mitochondrial fission and OPA1 processing mediates the balance between fusion and fission (Anand *et al.*, 2014). OPA1 mediated fusion is dependent on Mfn1 and not Mfn2 (Cipolat *et al.*, 2004). There is also an interaction between Opa1 and cardiolipin involved in mitochondria fusion (Ban *et al.*, 2017, 2018).

Interestingly, many of these proteins involved in mitochondrial fusion/fission are not mitochondrial specific and have similar functions at the peroxisome and other cellular compartments (Passmore *et al.*, 2020).

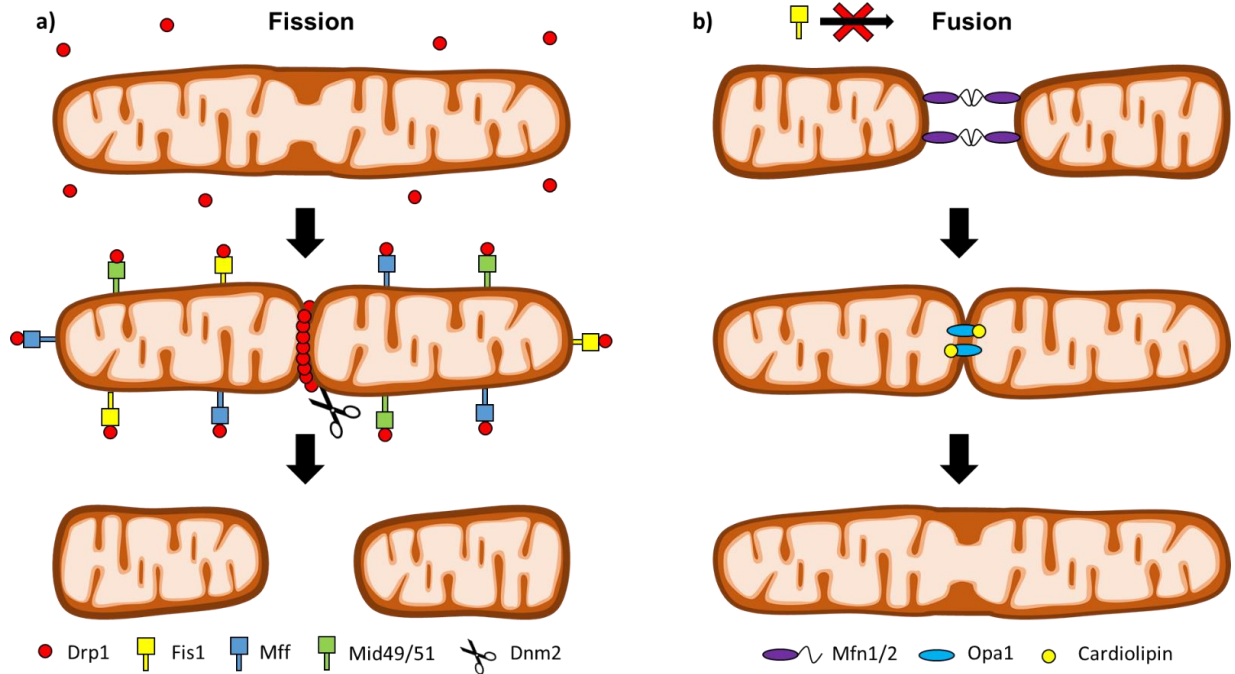


Figure 1.3. Mitochondrial fission and fusion.

Diagram of (a) mitochondrial fission and (b) mitochondrial fusion. Drp1, dynamin-related protein 1; Fis1, fission 1; Mff, mitochondrial fission factor, Mid, mitochondrial dynamics protein; Dnm2, dynamin 2; Mfn, mitofusins; Opa1, optic atrophy 1.

1.1.15 Mitophagy

The purpose of mitophagy is to remove damaged or excess mitochondria from the cell (Youle and Narendra, 2011). Interestingly two genes, PINK1 and Parkin, whose mutations are linked to Parkinson's disease, are important for mitophagy (Youle and Narendra, 2011). As well as the PINK1/Parkin pathway, there are other pathways by which mitophagy can occur. For example, several proteins interact with LC3 independently of Parkin such as NIX, BNIP3, FUNDC1 and Cardiolipin (Liu *et al.*, 2014). The different mitophagy pathways have been reviewed extensively elsewhere (Liu *et al.*, 2019). Studies have suggested that mitochondrial dysfunction can impact lysosomal function, as well as autophagic dysfunction affecting mitochondrial homeostasis (Park *et al.*, 2018).

1.2 Parkinson's disease

1.2.1 *Clinical characteristics*

First described by James Parkinson in 1817, Parkinson's disease (PD) is a progressive, neurodegenerative, motor disorder which affects ~1% of the over 60 population (Parkinson, 1817; de Lau and Breteler, 2006). PD is characterised by the degeneration of dopaminergic neurons within the substantia nigra pars compacta, leading to symptoms of bradykinesia (slowness of movement), resting tremor and muscle rigidity (Kalia and Lang, 2015). The disease can also present with non-motor symptoms, such as sleep dysfunction, cognitive impairment and depression (Kalia and Lang, 2015). Olfactory dysfunction is also present in the majority of PD patients (Doty, Deems and Stellar, 1988; Haehner *et al.*, 2009). Some of these non-motor symptoms may precede motor symptoms by many years and be markers for the pre-clinical stages of PD (Ross *et al.*, 2008; Postuma *et al.*, 2019).

While increasing age is the most prevalent risk factor for PD, environmental risk factors including exposure to pesticides such as paraquat, and high dairy intake have been associated with the disease (Ascherio and Schwarzschild, 2016). Melanoma patients also have an increased risk of PD, as well as PD patients having an increased risk of melanoma (Ascherio and Schwarzschild, 2016). Sex differences are also present within PD, with men being approximately 1.5 times more likely as women to develop idiopathic PD (Wooten *et al.*, 2004). There is some evidence to suggest women also have a more benign phenotype in the early stages of PD, which is proposed to be an effect of increased levels of oestrogens (Haaxma *et al.*, 2007). However, the protective effect of oestrogen is inconsistent between studies, with some showing no association between oestrogen and PD (Rugbjerg *et al.*, 2013). Interestingly, there is evidence that tobacco smoking and coffee drinking, which are risk factors for a multitude of other diseases, could be protective in PD (Ascherio and

Schwarzschild, 2016). These risk and protective factors have been reviewed in more detail by Ascherio and Schwarzschild 2016.

PD is very heterogenous and there is some evidence that clinical subtyping may be useful in estimating PD progression. For example, a recent study which classified PD patients into three subtypes based on severity of both motor and non-motor symptoms, showed differences in rate of disease progression between different subtypes (De Pablo-Fernández *et al.*, 2019). Age of onset can also be variable in different genetic forms of PD; for example, Parkin-related PD is associated with early disease onset (20-40 years of age), whilst Leucine-Rich Repeat Kinase 2 (LRRK2) PD tends to have a similar age of onset to idiopathic PD (>50 years of age) (Brüggemann and Klein, 1993; Healy *et al.*, 2008). Together, these differences mark an important need for patient stratification when assessing disease mechanisms and testing potential therapeutics.

1.2.2 Pathology

PD causes the selective degeneration of dopaminergic neurons within the substantia nigra pars compacta (Kalia and Lang, 2015). There are four main dopaminergic pathways: the mesocortical pathway projecting from the ventral tegmental area to the prefrontal cortex which is involved in working memory, learning and emotion; the mesolimbic pathway projecting from the ventral tegmental area to the nucleus accumbens which is associated with reward; the tuberoinfundibular pathway projecting from the hypothalamus to the pituitary gland which is involved with the secretion of the hormone prolactin; and the nigrostriatal pathway projecting from the substantia nigra pars compacta to the dorsal striatum, composed of the putamen and caudate nucleus, which is associated with movement (Ayano, 2016). The nigrostriatal pathway is the pathway affected in PD. **Figure 1.4** shows the difference between healthy and PD nigrostriatal pathways. There is a clear

depigmentation of the substantia nigra pars compacta in PD due to loss of dopaminergic neurons which produce the pigment neuromelanin (Dauer and Przedborski, 2003). Interestingly, the motor symptoms of PD are typically not present until 50-70% of nigral dopaminergic neurons are degenerated, meaning that early diagnosis and intervention is critical (Cheng, Ulane and Burke, 2010).

As well as nigral dopaminergic neuron lost, eosinophilic cytoplasmic inclusions termed Lewy bodies are present in most PD patients (Figure 3C). Aggregates of alpha-synuclein are the main component of these Lewy bodies (Spillantini *et al.*, 1997). The precise function of alpha-synuclein is not clearly defined, though it has been associated with several different cellular processes, including mitochondrial activity, vesicle transport and neurotransmitter release, membrane lipid content and curvature, and regulation of gene expression (Heras-Garvin and Stefanova, 2020). Immunohistochemical studies have shown that in addition to alpha-synuclein, there are more than 90 components of Lewy bodies including ubiquitin, PD linked-gene products, such as LRRK2 and Parkin, and mitochondrial proteins such as COXIV (Lowe *et al.*, 1988; Schlossmacher *et al.*, 2002; Greggio *et al.*, 2006; Bedford *et al.*, 2008; Wakabayashi *et al.*, 2013).

Braak staging describes Lewy body pathology throughout PD (Braak *et al.*, 2003, 2004). In the pre-symptomatic phases 1 and 2, Lewy bodies are present in the medulla oblongata/pontine tegmentum and the olfactory bulb/anterior olfactory nucleus. In phases 3 and 4 the pathology spreads to the substantia nigra and other nuclear grays of midbrain and forebrain. At these stages, most patients are symptomatic. In phases 5 and 6 the mature neocortex is affected (Braak *et al.*, 2004). Although supported both *in vitro* and *in vivo*, Braak staging may only apply to a specific subset of patients who have early onset PD with a long disease duration (Rietdijk *et al.*, 2017). The alternative threshold theory suggests that PD pathology does not ascend throughout the brain, but that pathology exists in multiple

systems which reach their threshold for symptoms at different rates (Engelender and Isacson, 2017). Indeed, it is unsure whether Lewy bodies are in fact cytotoxic, or merely a consequence of PD itself (Parkkinen *et al.*, 2011).

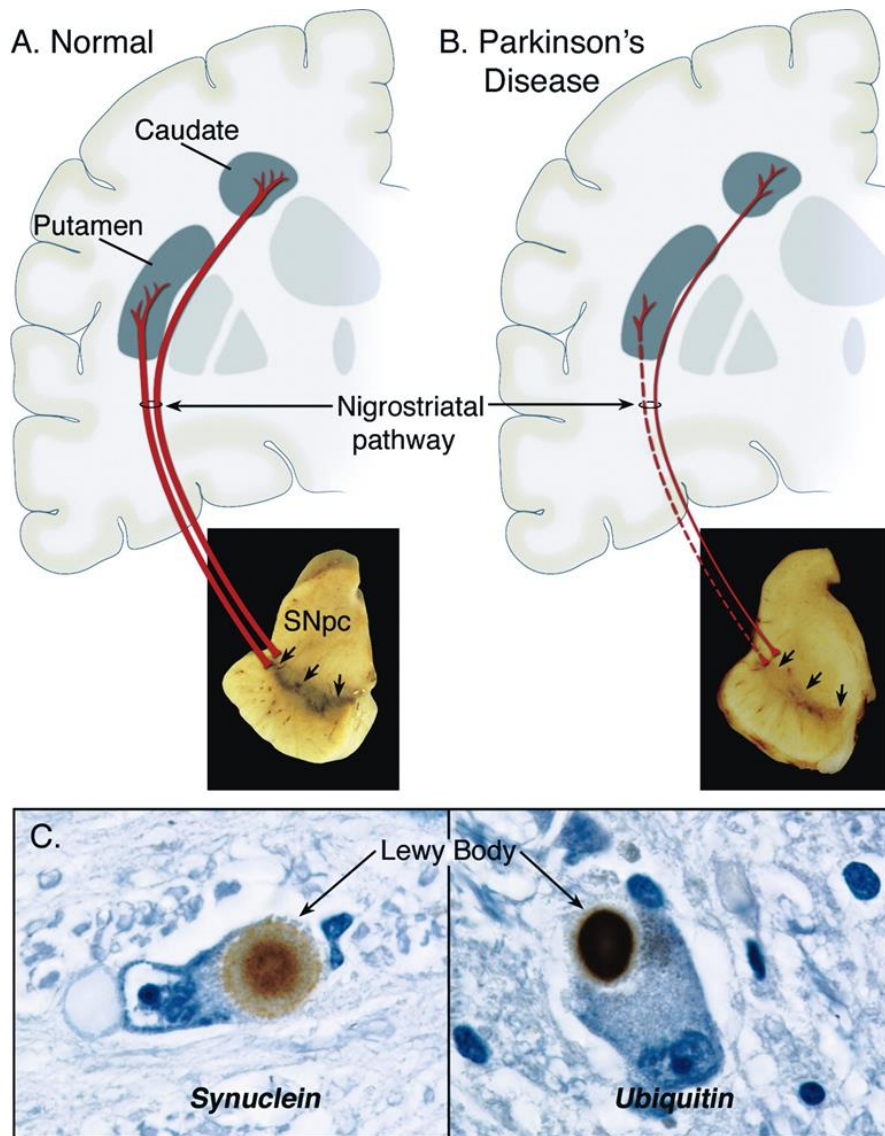


Figure 1.4. Parkinson's disease pathology.

A diagram of a healthy nigrostriatal pathway. B) A diagram of a Parkinson's disease nigrostriatal pathway. C) Immunohistochemical staining of Lewy bodies in a substantia nigra

pars compacta dopaminergic neuron. (left) Immunohistochemical staining against alpha-synuclein. (right) Immunohistochemical staining against ubiquitin. Figure reproduced with permission (Dauer and Przedborski, 2003).

1.2.3 Treatment of Parkinson's disease

Currently there is no disease-modifying treatment for PD which would slow down or even halt the progression of the disease. Treatments only control the symptoms of the disease. The most common treatment for PD is levodopa, a precursor to dopamine, which can cross the blood brain barrier and be converted to dopamine by DOPA decarboxylase (Nishijima and Tomiyama, 2016). Levodopa can be very effective in reducing PD symptoms but often leads to dyskinesias and motor fluctuations with continued treatment (Pandey and Srivanitchapoom, 2017). Dopamine agonists can be used in the early stages of PD to delay the onset of levodopa treatment and provide a modest improvement in PD symptoms (Stowe *et al.*, 2008). Other treatments include catechol-O-methyltransferase inhibitors and monamine-oxidase inhibitors, which reduce the breakdown of levodopa and dopamine, respectively (Riederer and Laux, 2011; Müller, 2015). The main surgical option is deep brain stimulation, which is usually targeted to either the subthalamic nucleus or the globus pallidus interna, and can be effective for patients who suffer from motor fluctuations and dyskinesias (Martinez-Ramirez *et al.*, 2015). The optimal treatment for PD would be to prevent the further degeneration of dopaminergic neurons, rather than be a symptomatic treatment. Therefore, it is imperative that the mechanisms underlying the disease are more clearly understood in order to find potential drug targets

1.2.4 Genetic forms of Parkinson's disease

The majority of PD cases are sporadic, with about 10% of PD patients reporting a positive family history. The first mutation to be associated with PD was found in 1997 in the SNCA

gene, which encodes alpha-synuclein. PD can be inherited through autosomal dominant, autosomal recessive and X-linked modes of inheritance. Typically, the autosomal dominant inherited forms of PD more closely resemble idiopathic PD, while the autosomal recessive forms of PD tend to have an earlier age of onset or a more atypical clinical phenotype. Mutations in LRRK2 account for the majority of genetic cases of PD (Klein and Westenberger, 2012).

1.2.5 Structure of LRRK2

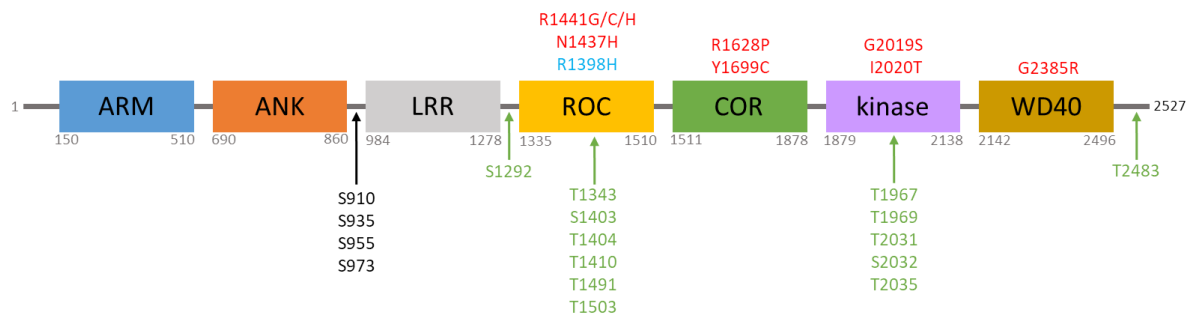


Figure 1.5. Domain structures of LRRK2.

Armadillo (ARM); Ankyrin (ANK); Leucine-Rich Repeat (LRR); Ras in complex protein (ROC); C-terminal of ROC (COR); cellular phosphorylation sites shown in black; autophosphorylation sites shown in green; Parkinson's disease pathogenic mutations and susceptibility polymorphisms shown in red. Protective Parkinson's disease variant shown in blue. Adapted from Wallings et al. 2015 (Wallings, Manzoni and Bandopadhyay, 2015).

The LRRK2 gene is composed of 51 exons, encoding 2527 amino acids which form a 286 kD protein (Lill and Klein, 2017). LRRK2 mutations were first implicated in PD in 2004 (Zimprich *et al.*, 2004). Mutations within the LRRK2 gene have also been associated with the inflammatory bowel disease Crohn's disease, suggesting a potential link between the two diseases (Hui *et al.*, 2018).

LRRK2 is composed of several functional domains, including two enzymatic cores; a ROC-COR GTPase domain, and a serine/threonine kinase domain (Wallings, Manzoni and Bandopadhyay, 2015). The action of the GTPase domain is to hydrolyse GDP to GTP, whilst the kinase domain phosphorylates target proteins (Wallings, Manzoni and Bandopadhyay, 2015). The N terminus of LRRK2 contains Armadillo, ankyrin and LRR domains. The functions of these domains are not clearly understood but it is thought that the LRR and Armadillo domains might be important structural frameworks for the formation of protein-protein interactions (Guaitoli *et al.*, 2016). It has been shown that the kinase activity of LRRK2 is not affected by mutants lacking the LRR, Armadillo or Ankyrin domains, though other evidence suggests that the ankyrin domain may have been involved in the inhibition of LRRK2's kinase activity due to its similarity in structure to other inhibitory ankyrin domains (Mills *et al.*, 2014). The C terminus of LRRK2 contains a WD40 domain which is required for LRRK2 induced neurotoxicity and is essential in LRRK2 kinase activity (Jaleel *et al.*, 2007; Jorgensen *et al.*, 2009). Interestingly, LRRK1 – a paralog of LRRK2 – lacks the armadillo and WD40 domains which may explain why LRRK1 is not implicated in PD (Haugarvoll *et al.*, 2007; Civiero *et al.*, 2012). However, research into LRRK1 function is lacking and warrants further investigation.

Seven confirmed pathogenic mutations have been found within the enzymatic core of LRRK2; N1437H, Y1699C, R1441C, R1441G and R1441H found within the GTPase domain, and I2020T and G2019S found within the kinase domain (Wallings, Manzoni and Bandopadhyay, 2015). This highlights importance of enzymatic function in understanding PD pathogenesis. As well as pathogenic mutations, there are also coding variants, G2385R and R1628P, found within the WD40 domain and GTPase domain respectively, which increase PD risk (Fu *et al.*, 2013). The G2019S mutation is the common LRRK2 mutation and is present worldwide in 1% of sporadic PD cases, and 4% of familial cases (Healy *et*

al., 2008). This frequency is dramatically increased in certain populations, such as North African Arabs (sporadic 39%, familial 36%) and Ashkenazi Jews (sporadic 10%, familial 28%) but very rarely observed in Asian populations (<0.1%) (Tan *et al.*, 2005; Healy *et al.*, 2008; Benamer and De Silva, 2010).

Evidence has shown that LRRK2 mutations have incomplete penetrance (Latourelle *et al.*, 2008). The levels of LRRK2-G2019S penetrance vary among studies but have been shown to increase with age, with ~28% penetrance at 59 years up to ~67–74% at the maximum age ranges studied (Healy *et al.*, 2008; Latourelle *et al.*, 2008). However, there is much disagreement in the literature as to the penetrance of LRRK2. This incomplete penetrance means that it is important to study populations who have a LRRK2 mutation but have not currently developed PD (non-manifesting), as well as those who have a mutation and are diagnosed with PD (manifesting) to gain understanding into which changes are pathogenic. It also suggests that there could be some potential rescue mechanisms. Interestingly, genetic studies have observed that the R1398H variant may be protective against PD. Mechanistic data shows the R1398H variant has the opposite effect to pathogenic LRRK2 GTPase domain mutations (Nixon-Abell *et al.*, 2016).

LRRK2 can be autophosphorylated at several residues and elevated urinary levels of LRRK2 phosphorylated at Ser-1292 have been shown to predict LRRK2 mutation status and PD risk (Fraser *et al.*, 2016). Additionally, evidence suggests that LRRK2-G2019S mutated primary astrocytes have enlarged lysosomes, which are dependent on LRRK2's kinase activity and autophosphorylation at Ser-1292 (Henry *et al.*, 2015). However, other LRRK2 mutations have either shown no effect on phosphorylation, or show a decrease, suggesting that phosphorylation status may not be an accurate biomarker for all forms of LRRK2 PD (Ito *et al.*, 2014; Reynolds *et al.*, 2014).

1.2.6 LRRK2 non-mitochondrial function and dysfunction

The highest expression of LRRK2 is in the lung, brain and kidney (Araki, Ito and Tomita, 2018), however the expression levels throughout the brain are unclear. It has been found that LRRK2 expression is higher in neurons than in astrocytes and microglia (Miklossy *et al.*, 2006). LRRK2 is mainly expressed in cytoplasm but, interestingly it has also been associated with the mitochondria. For example, in cells overexpressing LRRK2, 10% of LRRK2 was present in mitochondrial fractions (Biskup *et al.*, 2006). In addition, LRRK2 colocalises with the outer mitochondrial membrane and associate subunits of the translocase of outer mitochondrial membrane (TOM) complex (Neethling *et al.*, 2019). This association with TOM complex subunits is also present in cells overexpressing with the LRRK2-G2019S mutation (Neethling *et al.*, 2019). LRRK2 has been found to be present in 10-80% of alpha-synuclein positive Lewy bodies (Alegre-Abarrategui *et al.*, 2008).

LRRK2 is involved in several functions such as the modulation of cellular dynamics, autophagy and the immune system (Wallings, Manzoni and Bandopadhyay, 2015). Of note, LRRK2 is associated with lysosomal dysfunction. The knockout of LRRK2 has been shown to lead to an enlargement of lysosomes, however the effect of the LRRK2-G2019S mutation is variable between studies (Herzig *et al.*, 2011; Henry *et al.*, 2015; Schapansky *et al.*, 2018). Recently LRRK2 has been shown to phosphorylate members of the Rab family of proteins, which are involved in vesicle trafficking, suggesting that LRRK2 regulates this process (Steger *et al.*, 2016). Indeed, LRRK2 has been shown to interact with Rab7 and Rab8a to impair trafficking of the epidermal growth factor receptor (Gómez-Suaga *et al.*, 2014; Rivero-Ríos *et al.*, 2019). Interestingly pathogenic LRRK2 mutations have been shown to enhance the ability of LRRK2 to phosphorylate Rabs. As well as Rabs that are downstream from LRRK2, such as Rab8 and Rab10, Rab29 has been shown to function upstream (Kuwahara and Iwatsubo, 2020).

Several papers have also demonstrated that LRRK2 can phosphorylate tau, a protein associated with microtubules (Lin *et al.*, 2010; Bailey *et al.*, 2013; Shanley *et al.*, 2015). Interestingly, a recent study has shown that tau pathology is prominent in LRRK2 PD, with tau pathology being present in 100% of LRRK2 mutation carriers studied, while alpha-synuclein pathology was only present in 63.6% carriers (Henderson *et al.*, 2019). It has also been found that LRRK2-G2019S increases the neuron-to-neuron transmission of tau in mice compared with endogenous LRRK2 which is not required for this process (Nguyen *et al.*, 2018).

1.3 Mitochondria and Parkinson's disease

1.3.1 Sporadic Parkinson's disease

Mitochondria were first implicated in the pathogenesis of PD when it was discovered that exposure to 1-methyl-4-phenyl-1,2,3,6-tetrahydropyridine (MPTP), which metabolises to the complex I inhibitor MPP⁺, induces a Parkinsonian phenotype and loss of dopaminergic neurons in the SN. Neurons are particularly susceptible to mitochondrial dysfunction, largely due to their extremely high metabolic requirements. Nigral neurons – the cell type predominantly affected in PD – have a higher rate of basal oxidative phosphorylation compared to ventral tegmental area neurons, which are unaffected in PD (Haddad and Nakamura, 2015). This may lead to higher levels of oxidative stress, due to the production of reactive oxygen species (ROS) by the respiratory chain complexes (Haddad and Nakamura, 2015). These neurons also have a higher density of axonal mitochondria which may confer a further increase in risk (Pacelli *et al.*, 2015).

Reduced complex I activity was first observed in sporadic PD postmortem brain tissue (Schapira *et al.*, 1989), and platelets (Parker, Boyson and Parks, 1989). mtDNA may

be more susceptible than nuclear DNA to damage due to its higher exposure to ROS generated by oxidative phosphorylation (Yakes and Van Houten, 1997). Selective mtDNA damage has been found in nigral, but not cortical neurons, in PD postmortem brain tissue (Sanders *et al.*, 2014). There is also an increase in mtDNA somatic point mutations, especially in genes encoding mitochondrial complex IV (Coxhead *et al.*, 2016). Additionally, there are higher levels of mtDNA deletions in PD compared with age-matched controls (Bender *et al.*, 2006), which is associated with decreased complex IV activity. Decreased complex IV activity has been observed in patient fibroblasts (Carling *et al.* 2020) mtDNA deletions also occur during normal ageing; however, the mtDNA copy number increases to compensate for this in healthy controls (Dölle *et al.*, 2016). This upregulation of copy number does not occur in PD, indicating that mtDNA homeostasis is dysregulated (Dölle *et al.*, 2016).

In addition to impaired clearance of damaged mitochondria, the generation of new mitochondria may also be impaired in PD. Peroxisome proliferator-activated receptor gamma coactivator 1-alpha (PGC1- α) regulates mitochondria biogenesis by inducing the expression of several key biogenesis proteins (Corona and Duchen, 2015). PGC1- α knockdown increases α -synuclein aggregation in human neuronal cells, and overexpressing PGC1- α reduces the mitochondrial deficiencies seen in MPP+ treated SH-SY5Y cells, such as reduced ATP levels (Ebrahim, Ko and Yen, 2010; Ye *et al.*, 2016). *Drosophila* primary neurons treated with MPP+ also show a reduction in size, number, and an increase in fragmentation prior to cell death (Wiemerslage, Ismael and Lee, 2016).

1.3.2 Familial Parkinson's disease

As well as in sporadic cases, mitochondrial dysfunction has been implicated in both autosomal recessive forms of PD (with mutations in *parkin*/PARK2, *PINK1*/PARK6 and *DJ-*

1/PARK7) and autosomal dominant forms of PD (with mutations in *alpha-synuclein*/PARK1/4 and *LRRK2*/PARK8) (Bose and Beal, 2016). For example, fibroblasts derived from patients with *parkin* mutations show a distinct complex I deficiency, resulting in reduced ATP levels (Mortiboys *et al.*, 2008). Oxygen consumption is also reduced in *parkin* mutant *Drosophila* larvae (Vincent *et al.*, 2012); *parkin* knockdown zebrafish embryos also have lowered complex I activity (Flinn *et al.*, 2009). Interestingly, many of the genes associated with familial PD are involved in maintaining normal mitochondrial function. For example, PINK1 and PARKIN are important for mitophagy (Nguyen, Padman and Lazarou, 2016) and Dj-1 is thought to be a redox sensor and can protect cells from oxidative stress (Giroto *et al.*, 2012).

Interestingly, not only have individual mitochondrial complex dysfunctions been implicated in PD but also the supercomplexes that they form. Supercomplexes are thought to increase the efficiency of electron carrier transport and the oxidation of multiple substrates, decrease ROS production and are essential in complex I stability (Lapiente-Brun *et al.*, 2013; Chaban, Boekema and Dudkina, 2014). The disorganisation of mitochondrial supercomplexes has been observed in *PINK1* mutant human fibroblasts and *Pink1* mutant mouse primary neurons, as well as in *Dj1* mutant mouse primary neurons and brain tissue (Lopez-Fabuel *et al.*, 2017). A *pink* mutant zebrafish line also has specific decrease in complex I and III activity (Flinn *et al.*, 2013). Inactivation of the mitochondrial calcium uniporter rescues this complex I deficiency in *pink1* mutant zebrafish, suggesting that mitochondrial calcium homeostasis is crucial for maintaining normal function of the mitochondrial respiratory chain (Soman *et al.*, 2017).

The regulation of mitochondrial morphology is a tightly controlled process that can be affected in both sporadic and genetic forms of PD. For example, mitochondria in postmortem biopsy samples of the caudate nucleus and skeletal muscle of sporadic PD

patients are more variable in size and shape (Ahlqvist, Landin and Wroblewski, 1975; Lach *et al.*, 1992). However, morphology changes are difficult to assess in detail in postmortem PD brain tissue due to the limited preservation of mitochondrial ultrastructural details (Bose and Beal, 2016). Interestingly, increased mitochondrial branching has been described in *parkin* mutant human fibroblasts (Mortiboys *et al.*, 2008). In addition, morphological abnormalities, such as swollen mitochondrial cristae and a decrease in density of normal mitochondria, have been found in induced pluripotent stem cell-derived *parkin* mutant neurons (Imaizumi *et al.*, 2012). Changes in mitochondrial morphology have also been observed in various PD animal models. For example, an early study looking at mitochondrial abnormalities in *Parkin* mutants, observed that in *Parkin* null *Drosophila*, mitochondria are swollen and have severely disintegrated cristae (Greene *et al.*, 2003).

The removal of typically dysfunctional mitochondria, mitophagy, is a highly important cellular process, as the accumulation of dysfunctional mitochondria can lead to cellular damage. *PINK1* and *parkin*, two genes which have been associated with autosomal recessively inherited familial PD, encode proteins which are essential in mitophagy (Nguyen, Padman and Lazarou, 2016). *PINK1* acts upstream of *Parkin* (Clark *et al.*, 2006; Park *et al.*, 2006). *PINK1* phosphorylates both ubiquitin and *Parkin* at its ubiquitin-like domain, to activate *parkin* as an E3 ligase (Koyano *et al.*, 2014). This allows the ubiquitination of substrates such as *DRP1* and (H. Wang *et al.*, 2011; X. Wang *et al.*, 2011).

Miro is a protein found on the outer membrane of the mitochondria and connects them to dynein and kinesin motors, enabling microtubule-based transport (Tang, 2015). The *PINK1/Parkin* pathway targets *Miro* for proteasomal degradation prior to mitophagy (X. Wang *et al.*, 2011). Interestingly, *LRRK2* is also involved in *Miro* degradation. The disruption of both *Parkin* and *LRRK2* recruitment to damaged mitochondria coincides with the accumulation of *Miro*, and leads to a delay in mitophagy in fibroblasts from sporadic PD

patients (Hsieh *et al.*, 2016). This could be a potential pathway where both familial and sporadic PD converge.

1.3.3 LRRK2 Parkinson's disease

In LRRK2-G2019S mutant fibroblasts, Mortiboys *et al.* 2010, 2015 described a reduction ATP levels, mitochondrial membrane potential and oxygen consumption (Mortiboys *et al.*, 2010, 2015). In contrast, Papkovskaia *et al.* found an increase in oxygen consumption (Papkovskaia *et al.*, 2012). This may be due to the fibroblasts being grown in different media types, galactose containing and glucose containing respectively (Papkovskaia *et al.*, 2012; Mortiboys *et al.*, 2015). It has also been proposed that uncoupling proteins (UCPs) could be a biomarker for familial PD, as LRRK2-G2019S mutant fibroblasts have increased UCP2 mRNA expression (Papkovskaia *et al.*, 2012; Grünewald *et al.*, 2014). UCPs allow the passage of hydrogen ions from the intermembrane space to the matrix independent from complex V (Busiello, Savarese and Lombardi, 2015). It is thought that UCP2 is protective against mitochondrial ROS levels by reducing the mitochondrial proton gradient, this may therefore be a compensatory mechanism against oxidative stress (Grünewald *et al.*, 2014). LRRK2-G2019S mutant fibroblasts have reduced complex III and IV activity (Mortiboys *et al.*, 2015). In contrast, heterozygous knock-in LRRK2-G2019S mice show increases in complex V subunit ATP5A and complex III subunit UQCRC2 protein expression, while homozygous LRRK2-G2019S knock-in mice have reduced complex I subunit NDUFB8 expression (Yue *et al.*, 2015).

LRRK2-G2019S knock-in mouse models show altered mitochondrial morphology within the striatum including a beads-on-a-string-like appearance, condensation, reduction in number through autophagic degradation, and an approximately 10% increase in mitochondria length (Ramonet *et al.*, 2011; Cherra *et al.*, 2013; Yue *et al.*, 2015). Interestingly, LRRK2

phosphorylates DRP1, mediating mitochondrial fission. Disruptions to DRP1-mediated fission *via* LRRK2 mutations could lead to changes in mitochondrial dynamics (Uo *et al.*, 2009; Wang *et al.*, 2012; Y.-C. Su and Qi, 2013).

It is important that mitochondria can be transported effectively along the extended length of neurons and meeting the high energy demands of synapses at the axon terminals (Sheng and Cai, 2012). *LRRK2* mutations in the Roc-COR domain, LRRK2-R1441C and LRRK2-Y1699C, inhibit bidirectional axonal transport of mitochondria in both *Drosophila* larvae motor neurons, and rat cortical neuron cultures. However, this effect is not observed in LRRK2-G2019S mutant *Drosophila* (Godena *et al.*, 2014), suggesting that mutations in the different LRRK2 domains may result in distinct phenotypes. These models use ectopically expressed LRRK2 mutations; therefore, it would be important to also examine mitochondrial transport when these LRRK2 mutants are expressed at the endogenous locus. This could be achieved using techniques such as CRISPR/Cas9. A more detailed discussion of mitochondrial dysfunction in LRRK2 PD is included in the results chapters of this thesis.

1.3.4 LRRK2 PD treatments

As previously mentioned, there are currently no effective disease modifying treatments for PD. There has been substantial progress in recent years in developing therapeutics for LRRK2 PD. A toxic gain-of-function mechanism of LRRK2 PD pathogenesis has been proposed, therefore LRRK2 kinase inhibitors have been tested as potential therapeutics. Denali Therapeutics has tested two LRRK2 kinase inhibitors in Phase 1 trials, DNL201 and DNL151. At the time of writing this thesis, Denali Therapeutics had successfully completed a Phase 1 study of DNL201 in 122 healthy participants and a Phase 1b study in 28 PD patients, both sporadic and those with a LRRK2 mutation. Ongoing Phase 1 and Phase 1b

trials of DNL151 had also completed dosing of 162 healthy participants and 25 PD patients, respectively. Of the results obtained thus far, both drugs met safety, target engagement and biomarker goals. DNL151 has been selected to advance into late-stage studies in both LRRK2 PD and sporadic PD patients, with patient enrolment expected to commence in 2021. There have been some concerns regarding the safety of LRRK2 inhibitors, therefore dosing will need to be carefully monitored. Another strategy targeting LRRK2 PD, is the use of antisense oligonucleotides (ASOs). The aim of LRRK2 ASOs is to induce a long-term reduction in expression of LRRK2 to reduce LRRK2 kinase activity (Korecka *et al.*, 2020). At present, a phase I study of intrathecal administration of ASO BIIB094 is ongoing.

1.3.5 Treatments targeting mitochondrial dysfunction in PD

The majority of studies testing mitochondrial targeting therapeutics have focused on the treatment of sporadic PD. There are several strategies being used to target the mitochondrial dysfunction in PD, for example; mitochondrially targeted antioxidants, peptide strategies, strategies to manipulate mitochondrial control and dynamics, and deep brain stimulation strategies. These strategies have been reviewed in detail by Macdonald *et al.* 2018. One of the major challenges in developing treatments for PD is the heterogeneity of the condition and may explain why many clinical trials have produced negative results. For example, coenzyme Q10, a mitochondrial enhancer, was not shown to be neuroprotective in non-stratified PD patients. Therefore, a newer approach to clinical trials is to stratify patients based on their genetic 'mitochondrial risk burden' (Prasuhn *et al.*, 2019).

Increasingly, drug screening is focusing on testing naturally occurring compounds, and re-purposing pharmaceuticals already shown to be safe in humans. Using this approach, evidence from our group suggests that bile acids may improve some of the mitochondrial deficiencies seen in PD (Mortiboys, Aasly and Bandmann, 2013; Mortiboys *et al.*, 2015).

Ursocholic acid (UCA) and ursodeoxycholic acid (UDCA) were found to increase cellular ATP levels in both manifesting and non-manifesting LRRK2 G2019S fibroblasts, as well as reversing visual defects in LRRK2 G2019S transgenic flies (Mortiboys, Aasly and Bandmann, 2013; Mortiboys *et al.*, 2015). The mechanism of action of UDCA and UCA is unclear, but it is proposed to be Akt-mediated. At the time of writing this thesis, a phase II, two-centre, double-blind, randomised, placebo-controlled trial of UDCA at 30mg/kg in patients with PD is being led by Professor Oliver Bandmann, University of Sheffield (Trial registration number: NCT03840005). This trial is using ³¹Phosphorus MR Spectroscopy to assess the levels of ATP and other metabolites in the brain, as well as a motion sensor-based approach to quantify motor impairment (Payne *et al.*, 2020).

1.4 Project rationale and aims

There is evidence of mitochondrial dysfunction in LRRK2-G2019S PD. However, the mechanisms of this mitochondrial dysfunction are still unclear. It is important to assess the mitochondrial phenotype of LRRK2-G2019S PD in order to find and assess therapeutic targets. A specific decrease in mitochondrial complex III and IV activity was demonstrated in a study by Mortiboys *et al.* 2015. Therefore, one aim of this thesis was to characterise in further detail any changes in mitochondrial complexes in an expanded cohort of LRRK2-G2019S manifesting, non-manifesting and control fibroblasts. We also aimed to use some recently developed probes for reactive oxygen species and copper in our cells to see whether there were any changes in these parameters.

The phenotype of mitochondrial morphology in LRRK2 PD has conflicting findings within the literature, within some studies observing a 'beads-on-a-string'-like morphology suggesting impaired mitochondrial fission, while other studies report an increase in mitochondrial fission. Therefore, as well as functional changes in LRRK2-G2019S

fibroblasts, another aim of this thesis was to look at mitochondrial morphology and mitochondrial fusion and fission factor expression. In addition, UDCA and UCA have been shown to increase ATP levels in LRRK-G2019S fibroblasts: the effect of treatment of these drugs was assessed in some of the parameters tested, in order to further clarify any potential mechanism of actions for these therapeutics.

Fibroblasts are a commonly used model to study mitochondrial dysfunction as they are easily cultured and retain the genetic background of the donor. However, fibroblasts are not the degenerative cell type in people with PD. Therefore, a newly developed protocol by Schwartzenuber et al 2020 was used in this thesis to directly convert fibroblasts into induced neural progenitor cells, and subsequently differentiate these into dopaminergic neuron-like cells. Direct reprogramming methods such as this have the benefit that they retain the aged phenotype of the cells (Gatto *et al.*, 2020). The aged phenotype is something that is difficult to model in iPSC-derived dopaminergic neurons without lengthy culturing times. We aimed to characterise the mitochondrial phenotype throughout LRRK2-G2019S iNPC-derived dopaminergic neuron-like cell differentiation to assess both early and late changes in mitochondrial dysfunction, and whether there was any difference in the mitochondrial phenotype compared to the findings in fibroblasts.

In summary, the aims of this thesis were to further characterise mitochondrial dysfunction in LRRK2-G2019S fibroblasts and iNPC-derived dopaminergic neuron-like cells, by examining both functional and morphological characteristics.

Chapter 2 **Materials and methods**

2.1. Patient and control lines used

Skin biopsies were taken from LRRK2 manifesting (63.0 ± 9.0 years), LRRK2 non-manifesting (51.0 ± 15.9 years) and controls (61 ± 12.8 years; Table 2.1.) and were cultured until fibroblasts began to grow. These skin biopsies were set up by our collaborators Professor Jan Aasly (Department of Neurology, St Olav's Hospital, Trondheim, Norway) and Professor Gunnar Brønstad (Neurozym, Norway) in line with local ethics), as well as at the University of Sheffield (Ethical approval no. 4.2008.414). Some fibroblast lines were also obtained from the Coriell Cell repository.

Table 2.1. Details of fibroblast lines generated from LRRK2 G2019S manifesting, LRRK2 G2019S non-manifesting, and control patient biopsies.

| Number | Disease status | Age | Sex |
|---------------|------------------------------|------------|------------|
| TRD03 | LRRK2-G2019S manifesting | 55 | F |
| TRD04 | LRRK2-G2019S manifesting | 56 | M |
| TRD07 | LRRK2-G2019S manifesting | 77 | M |
| TRD11 | LRRK2-G2019S manifesting | 70 | M |
| NPFC-008 | LRRK2-G2019S manifesting | 65 | M |
| NPFC-028 (M2) | LRRK2-G2019S manifesting | 71 | M |
| NPFC-071 (M1) | LRRK2-G2019S manifesting | 52 | F |
| ND34198 | LRRK2-G2019S manifesting | 58 | M |
| TRD05 | LRRK2-G2019S non-manifesting | 64 | M |

| | | | |
|----------------|------------------------------|----|---|
| TRD12 | LRRK2-G2019S non-manifesting | 40 | M |
| NPFC-005 | LRRK2-G2019S non-manifesting | 55 | M |
| NPFC-025 | LRRK2-G2019S non-manifesting | 26 | F |
| NPFC-046 (NM3) | LRRK2-G2019S non-manifesting | 79 | F |
| NPFC-048 (NM2) | LRRK2-G2019S non-manifesting | 44 | F |
| NPFC-061 (NM1) | LRRK2-G2019S non-manifesting | 49 | M |
| NPFC-068 (NM4) | LRRK2-G2019S non-manifesting | 51 | F |
| TRD23 | Control | 73 | M |
| NPFC-006 | Control | 59 | M |
| NPFC-013 | Control | 58 | F |
| NPFC-024 | Control | 57 | M |
| NPFC-026 | Control | 66 | F |
| NPFC-027 | Control | 58 | F |
| NPFC-036 | Control | 71 | M |
| NPFC-041 | Control | 55 | F |
| NPFC-050 | Control | 72 | F |
| NPFC-051 | Control | 83 | M |
| NPFC-055 | Control | 44 | F |
| NPFC-060 | Control | 30 | F |
| NPFC-064 | Control | 57 | F |
| GM13335 | Control | 57 | M |
| GM02419 | Control | 54 | F |
| 8401 | Control | 75 | M |

2.2. Cell Culture

2.2.1. Cell culture of fibroblasts

All lines were grown in Eagle's Minimum Essential Medium (EMEM) (Lonza) supplemented with 10% Foetal Bovine Serum (FBS) (Biosera), 1% Minimum Essential Medium (MEM) vitamins (Lonza), 1% penicillin/streptomycin (Lonza), 1% sodium pyruvate (Sigma), 1% non-essential amino acids (Lonza), and 500 µl uridine (50 mg/ml; Sigma). Cells were routinely tested for mycoplasma and treated with ciprofloxacin if mycoplasma was detected.

In selected experiments, media containing galactose instead of glucose was used. For this Dulbecco's Modified Eagle's Medium (DMEM) without glucose (Gibco) was supplemented with 10% FBS (Biosera), 1% MEM vitamins (Lonza), 1% penicillin/streptomycin (Lonza), 1% sodium pyruvate (Sigma), 1% non-essential amino acids (Lonza), 500 µl uridine (50 mg/ml) (Sigma), and 0.9 mg/ml of galactose (Sigma).

Cells were passaged when near confluency by transferring their current media into a universal tube or 15 ml falcon tube, washing the cells twice with PBS, and adding 5 ml of trypsin/EDTA 1x (Lonza) per flask for 5-10 minutes until cells were detached. The cell/trypsin mixture was then neutralised with the previously set aside media and centrifuged at 500 rcf for 4 minutes to form a cell pellet. This pellet was resuspended in 10 ml of fresh media and transferred to a T75 flask (Greiner or Nunc). No cells higher than passage 20 were used and were passaged matched to within approximately 2 passages of each for all live experiments.

2.2.2. Generation of induced neural progenitor cells

Induced neural progenitor cells (iNPCs) were generated from LRRK2 G2019S manifesting, non-manifesting and control fibroblasts into iNPCs by Dr Heather Mortiboys using the

following protocol (Meyer *et al.*, 2014). 10⁴ fibroblasts were transduced with adenoviral non-integrating vectors for OCT3, Sox2, KLF4, Lin28 and Nanog. 48 h after transduction, cells were treated with NPC inducing factors (FGF-b, EGF and Heparin). iNPCs can be maintained ~30 passage. Fibroblasts were moved DMEM media supplemented with sodium pyruvate and penicillin/streptomycin prior to the start of iNPC generation. Table 2.2. describes the details of the cell lines that the iNPCs were generated from.

Table 2.2. Details of LRRK2-G2019S manifesting and control fibroblast lines used to generate induced neural progenitor cells

| Number | Disease status | Age | Sex |
|---------------|--------------------------|------------|------------|
| NPFC-071 | LRRK2-G2019S manifesting | 52 | F |
| ND29510 | Control | 55 | F |

2.2.3. iNPC cell culture

iNPCs were grown in Glutamax DMEM/F12 Ham (1:1) media supplemented with 1% N2, 1% B27 (Invitrogen) and 1% penicillin/streptomycin (Lonza), and FGFb (Peprotech) with incubation at 37°C, at 5% CO₂. iNPCs were grown on 10 cm² dishes coated with diluted 1/200 fibronectin diluted in PBS. Cell lines were split twice per week using accutase (Sigma) to detach the cells. Cells were not used beyond passage 23. For the DA neuron-like cell model differentiation, cells were plated in 6 well plates and the differentiation started at 75-85% confluency.

2.2.4. iNPC-derived DA neuron-like cell model differentiation protocol

Patients and controls were differentiated at the same time using the same protocol. Cells were grown in Glutamax DMEM/F12 Ham (1:1) media supplemented with 1% N2, 2% B27 (Invitrogen) and 1% penicillin/streptomycin (Lonza). The differentiation protocol has been

published by our group (Schwartzentruber et al. 2020; Carling et al. 2020). Briefly, DAPT (2.5 μ M; Tocris) was added for 2 days to prevent non-specific differentiation into astrocytes. After this, the cell media was changed every day with differentiation factors added. Cells were washed with PBS to prevent an accumulation of dead cells. FGF-8 (75 ng/ml; Peprotech) and Smoothed Agonist (SAG) (1 μ M; Millipore) were added for 10 days. On day 3 of FGF/SAG factors until the end of the protocol, ciprofloxacin (1 μ g/ml) was added to the media to prevent mycoplasma contamination. Previous work by the group (unpublished) has shown that this does not affect neuronal differentiation. At day 10 of FGF/SAG cells were replated into 96 well plates for ATP and imaging assays at a density of \sim 10,000 cells per well, accounting for cell death, using accutase to detach the cells. For western blotting experiments, cells were kept in 6 well plates at a density of \sim 200,000 per well. For assays throughout the differentiation protocol, cells were replated 1-2 days prior to this so that they could be assayed on the final day of FGF/SAG treatment. For a further 15 days after FGF/SAG treatment, unless otherwise stated, TGF- B_3 (2 mM), dCAMP (2 mM, Sigma), BDNF (30 ng/ml) and GDNF (30 ng/ml) were added to the cell media. (Peprotech). **Figure 2.1** describes the differentiation protocol and the time points of assays. Cell media was replaced each day from Phase 2 onwards.

For non-glucose/non-galactose media, or galactose media experiments Dulbecco's Modified Eagle's Medium (DMEM) without glucose (Gibco) was used. This was supplemented with the phase 3 neuronal differentiation factors. For the galactose containing media plus 0.9 mg/ml of galactose (Sigma) was added.

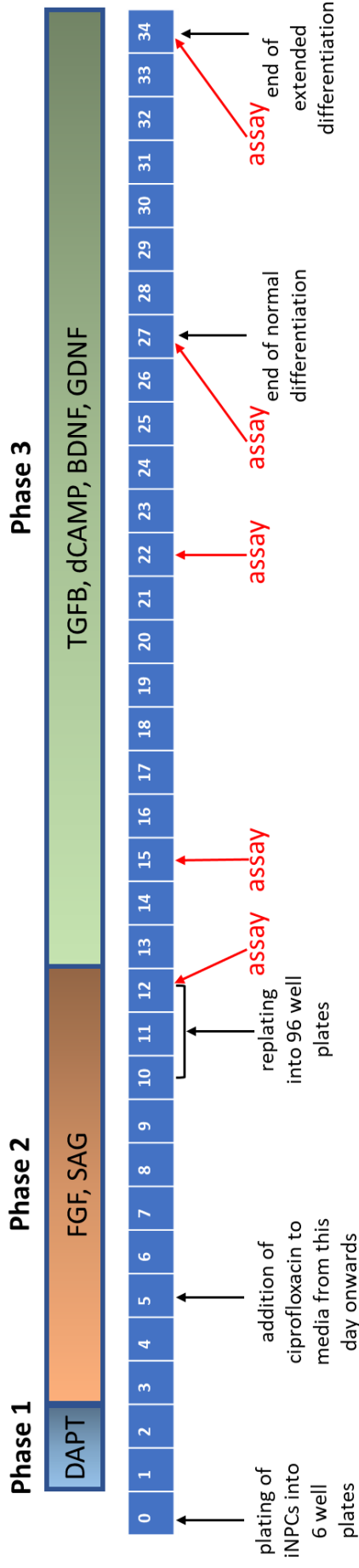


Figure 2.1. Neuron-like cell model differentiation protocol.

Figure shows the different phases of differentiation. iNPC-derived DA neuron-like cells were assayed at different time points throughout the differentiation, which is highlighted in red.

2.3. ATP assays

Fibroblasts were plated at ~5000 cells per well in EMEM media containing glucose in white-walled 96 well plates (Greiner Bio-one). Cells were left to adhere overnight, before adding galactose containing media to half of the wells. 24 hours later the ATP assay was completed using ATPlite kit (Perkin Elmer). In brief, cells were washed with 100 μ l PBS, before adding 100 μ l PBS then 50 μ l lysis buffer per well. The plate was then shaken at 700 rpm for 5 minutes, before adding 50 μ l substrate solution per well and shaking again (700 rpm, 5 minutes). The plate was dark adapted for 10 minutes and then read on the luminescence mode of the plate reader (PHERAstar FS, BMG Labtech, or Omega plate reader).

To be able to normalise between different cell lines for differences in plating, ATP values were normalised to cell number by quantifying the DNA content of the same wells. After the ATP measurement, 50 μ l Cyquant (ThermoFisher) per well was added (1.1 μ l Cyquant reagent, diluted per 1 ml HBSS or PBS) and incubated at 37°C for 1-3 hours before reading on the absorbance mode of the plate reader (497 nm excitation, 520 nm emission).

For both the ATP assay and Cyquant quantification, there were three blank wells containing no cells. The average value of these were taken away from each ATP and Cyquant value, respectively. ATP values were then normalised to the Cyquant values. To compare across experiments, each of these values were normalised to the control fibroblasts grown in EMEM media containing glucose.

For the iNPC-derived DA neuron-like cell model, the same protocol was used, however the plating was completed as described in section 1.6.4. and at the time points specified in **Figure 2.1**.

2.4. Mitochondrial membrane potential and lysosome assays

Fibroblasts were plated at ~2000 cells per well in EMEM media containing glucose (as described above) in black-walled 96 well plates (Perkin Elmer). Cells were left to adhere overnight, before adding galactose containing media to 50% of the wells for 24 h. For the iNPC-derived DA neuron-like cell model, plating was completed as described in section 1.6.4. and at the time points specified in **Figure 2.1**.

Media was replaced with either phenol-red free MEM (Lonza) or phenol-red free MEM with containing 10 μ M carbonyl cyanide m-chlorophenyl hydrazine (CCCP) (Sigma). The plate was then incubated for 1 hour at 37°C. Next, cell media was replaced with phenol-red free MEM with 80 nM tetramethylrhodamine, methyl ester (TMRM) (ThermoFisher) to stain the mitochondria and 1 μ M Hoechst (Sigma) to stain the nucleus. For lysosomal assays, 1 μ M LysoTracker Green (Invitrogen) was added. Cells that previously had CCCP added also had 10 μ M CCCP added to this mixture. Cells were then incubated at 37°C for an additional 1 hour. After, cells were washed with phenol-red free MEM and imaged.

Fibroblasts were imaged using the InCell 2000 high content imager microscope (GE Healthcare). During this imaging, cells were kept a temperature of 37°C using a plate heater. Any plates that contained over 36 wells of cells were also incubated at 5% CO₂. 20 fields of view were imaged per well which were randomised each experiment. Hoechst was imaged in the DAPI channel (350 nm excitation, 450-455 nm emission), and TMRM was imaged in the Cy3 channel (542 nm excitation, 604-664 nm emission). Images were analysed using a custom protocol in InCell Developer Toolbox (Diot *et al.*, 2015). In this, individual nuclei and mitochondria were segmented. Short mitochondria were defined as having a form factor >0.4 and long mitochondria were defined as having a form factor <0.4.

iNPC-derived neuron-like cells were imaged using an Opera Phenix High Content Screening System with 20-30 fields of view per well and z-stacks were taken across the cell. Hoechst was imaged in the DAPI channel (405 nm excitation, 435-480 nm emission), TMRM was imaged in the mCherry channel (562 nm excitation, 570-630 nm emission), and LysoTracker was imaged in the Alexa 488 channel (488 nm excitation, 500-550 nm emission).

2.5. Copper and reactive oxygen species probes

Fibroblasts were plated at ~2000 cells per well in EMEM media containing glucose in black 96-well plates (Perkin Elmer). Cells were left to adhere for 48 hours. For the iNPC-derived DA neuron-like cell model, the plating was completed as described in section 1.6.4. and at the time points specified in **Figure 2.1**. One cytosolic ROS probe (NpFR1), two mitochondrial ROS probes (NpFR2 and FRR2) and one copper probe (InCCu1) were used, which were kindly provided by our collaborator Dr Elizabeth New, University of Sydney, Australia (Yeow *et al.*, 2014a; Kaur *et al.*, 2015; Shen *et al.*, 2016). NpFR1, NpFR2 and FRR2 were used at a concentration of 40 μ M and InCCu1 at 200 nM, diluted in phenol-red free MEM media. Cells were incubated for 45 minutes with one of the probes plus Hoechst (1 μ M) before washing the cells with phenol-red free MEM and imaging using an Opera Phenix High Content Screening System. FRR2 and InCCu1 are ratiometric probes, though we were unable to visualise the second channel for normalisation. However, conclusions can still be drawn from the channel that visualises the mitochondria, as confirmed with our collaborator.

To measure cytosolic copper the cytosolic probe NS2-AI-SiR was used, which was kindly donated by our collaborator Professor Christopher Chang, University of California, Berkeley. For this probe, cells were incubated with Hoechst (1 μ M) diluted in phenol-red

free MEM media for 45 minutes. This was then removed, and cells were incubated with 1 μ M NS2-AI-SiR diluted in phenol-red free MEM media for 15 minutes. Cells were then imaged without washing.

15-20 fields of view were imaged per well for fibroblasts and 20-30 fields of view per well for iNPC-derived neuron-like cells. Z-stacks were taken across the cell. Hoechst was imaged in the DAPI channel (405 nm excitation, 435-480 nm emission), FRR2 and InCCu1 were imaged in the Alexa 568 channel (561 nm excitation, 570-630 nm emission), NpFR1 and NpFR2 were imaged in the Alexa 488 channel (488 nm excitation, 500-550 nm emission), and NS2-AI-SiR was imaged in the Alexa 647 channel (640 nm excitation, 650-7600 nm emission).

2.6. Drug treatments

Fibroblasts were grown in different treatment conditions for 24 hours before harvesting into cell pellets. The equivalent of one confluent flask per cell pellet was used. Cells were pelleted by transferring their current media into a universal tube, washing the cells twice with PBS, and adding 5 ml of trypsin (Lonza) per flask for 5-10 minutes until cells were detached. The cell/trypsin mixture was then neutralised with the previously set aside media and centrifuged at 500 rcf for 4 minutes to form a cell pellet. The supernatant was removed, the pellet resuspended with 1 ml of PBS, and the centrifugation step repeated to wash the cells. The supernatant was then removed again and the remaining pellet was stored at -80°C.

The different treatment conditions were either in glucose or galactose containing media and were as follows; untreated, DMSO (1:1000), 10 μ M UDCA, 100 nM UCA (Sigma). These concentrations of UDCA and UCA were chosen as they were the EC90 of ATP levels. This was the same for both live assays and western blots.

2.7. Western blotting

2.7.1. Protein quantification

Prior to the start of this study, previous optimisation by the group found that 10 µg of protein was optimal for the antibodies used. To quantify the amount of protein in the cell pellets prior to this, a Bradford assay was used. Cell pellets were lysed by adding a mixture of 50 µl RIPA buffer and 5 µl of protease inhibitor and incubated on ice for 30 minutes. Next, the lysed pellets were centrifuged for 10 minutes at 16,000 rcf. The supernatant was then transferred to a separate Eppendorf tube. To perform the Bradford assay, BSA standards were used to produce a standard curve (concentrations; 100, 125, 250, 500, 750, 1000, 1200 µg/µl). 5 µl of each BSA standard, plus a dH₂O control, was added in triplicate to a 96 well plate. Each sample was then added in triplicate to the plate at both a 2ul and 1ul volume. To each well, 250 µl coomassie blue was added and then the plate was read in the absorbance mode (595nm) of the plate reader. A standard curve was quantified in GraphPad Prism and used to estimate the protein content of the samples. A 1:5 ratio of sample buffer was then added to the samples, which were then stored at -80°C. Tables 2.3-2.8 provide the reagents of the various western blotting buffers.

Table 2.3 4x sample buffer

| Reagent | Supplier | Volume/Weight |
|---------------------------|-------------------|---------------|
| Tris HCl pH 8.0 | Melford | 0.62 g |
| Glycerol | Sigma-Aldrich | 8 ml |
| SDS | Fisher Scientific | 1.8 g |
| Bromophenol Blue | Sigma-Aldrich | 0.008 g |
| Dithiothreitol (DTT) | Sigma-Aldrich | 0.8 g |
| Nanopure H ₂ O | | 10 ml |

Table 2.4 Resolving gel (12%)

| Reagent | Supplier | Volume/Weight |
|-------------------------------------|----------------------|---------------|
| Tris HCl pH 8.8 | Melford | 2.5 ml |
| 30% Bis/acrylamide | National Diagnostics | 4 ml |
| Nanopure H ₂ O | | 3.3 ml |
| 10% SDS | Fisher Scientific | 100 µl |
| 10% ammonium persulfate (APS) | Sigma-Aldrich | 100 µl |
| Tetramethylethyl-enediamine (TEMED) | Melford | 4 µl |

Table 2.5 Stacking gel

| Reagent | Supplier | Volume/Weight |
|-------------------------------------|---------------|---------------|
| Tris HCl pH 6.8 | Melford | 666 µl |
| 30% Bis/acrylamide | Melford | 450 µl |
| Nanopure H ₂ O | | 1.5 ml |
| 10% ammonium persulfate (APS) | Sigma-Aldrich | 20 µl |
| Tetramethylethyl-enediamine (TEMED) | Melford | 5 µl |

Table 2.6 Running buffer (10 L)

| Reagent | Supplier | Volume/Weight |
|---------------------------|-------------------|-----------------|
| Tris Base | Melford | 30 g |
| Glycine | Sigma-Aldrich | 144 g |
| SDS | Fisher Scientific | 10 g |
| Nanopure H ₂ O | | Make up to 10 L |

Table 2.7 Transfer buffer (1 L)

| Reagent | Supplier | Volume/Weight |
|--|-------------------|---------------|
| Transfer buffer (150 g Tris base, 720 g Glycine) | | 200 ml |
| Methanol | Fisher Scientific | 100 ml |
| Nanopure H ₂ O | | 700 ml |

Table 2.8 TBST (10 L)

| Reagent | Supplier | Volume/Weight |
|---|-------------------|---------------|
| Sodium chloride | Fisher Scientific | 80 g |
| Potassium chloride | Fisher Scientific | 2 g |
| Tris base | Melford | 30 g |
| Make up to 9 L with Nanopure H ₂ O, then pH to 7.4 using HCl | | |
| Tween20 | Sigma-Aldrich | 5 ml |

2.7.2. Preparing and running gels

Glass plates were cleaned and secured into a casting apparatus. All western blot apparatus was supplied by Biorad. A 12% acrylamide resolving gel was prepared (Table 2.4) and poured between the glass plates. A layer of isopropanol was then added and the gel was left to polymerise for 15-30 minutes. The isopropanol layer was then removed and cleaned with filter paper. Next, a 10% acrylamide stacking gel (Table 2.5) was added and combs inserted to form the wells. This was left to polymerise for 15-30 minutes.

In the meantime, the protein samples and a dual colour molecular weight ladder (Biorad) were thawed on ice. The gels were then moved from the casting apparatus into a gel holder assembly and placed in a tank. The combs were removed and the tank was filled to 75% with SDS-PAGE buffer, ensuring that the section between the 2 gels was fully filled with buffer. Samples were loaded at 10 µg, as well as loading 5 µl of the ladder. The gel was then run at a constant 50 V for 30 minutes to pass samples through the stacking gel. The voltage was then changed to 120 V for at least 90 minutes to allow separation through the resolving gel.

2.7.3. Transfer

Next, the transfer buffer was prepared by combining 200 ml 5X transfer buffer, 100 ml methanol and 700 ml dH_2O . A polyvinylidene fluoride (PVDF) membrane was cut to the size of the resolving gel and soaked in methanol. Transfer cassettes, sponges and filter paper were also soaked in transfer buffer. The gel was then transferred from the SDS-PAGE buffer and the stacking gel removed to leave the resolving gel. The transfer assembly was then added together; sponge, filter paper, resolving gel, PVDF membrane, filter paper, sponge, and then placed in a tank. This was filled with transfer buffer and run at a constant amperage of 250 mA with an ice pack for 60 minutes so the gel would transfer onto the membrane.

2.7.4. Antibodies

The membranes were removed from the transfer buffer and washed in TBST. The membranes were then incubated for 60 minutes in 5% non-fat dry milk diluted in TBST. Primary antibodies diluted in TBST were then added for overnight incubation at 4°C (or 1 hour at room temperature for beta-actin) (Table 8). The membranes were then washed 3 x 10 minutes in TBST. Secondary antibodies diluted in TBST were then added for 1 hour (Table 2.8). The membranes were then washed again for 3 x 10 minutes. Membranes were

covered by ECL for 1 minute before removing excess ECL and imaging in chemiluminescent mode on the G-box (SynGene). Images were taken using the Intelli-mode of the G-box with markers included to check that the bands were of the correct molecular weight. Images were then taken in classic mode for densitometry analysis at sub-saturating levels.

2.7.5. Densitometry

Genetools software (Syngene) was used for densitometry analysis. Each lane was segmented and the background corrected. The total volume for each band was then calculated and exported to Microsoft Excel for analysis. Each antibody was normalised to beta-actin as a loading control, before being normalised to untreated control samples. Each membrane contained at least one control fibroblast line for normalisation.

Table 2.9 Antibodies used for western blotting

| Antibody | Supplier | Species | Dilution | Incubation |
|---|--------------------------|----------------|-----------------|---|
| Anti-BCS1L primary antibody | Santa Cruz Biotechnology | Mouse | 1:1000 | Overnight at 4°C |
| Anti-SCO2 primary antibody | Abcam | Rabbit | 1:1000 | Overnight at 4°C |
| Anti-OPA1 primary antibody | BD Biosciences | Mouse | 1:1000 | Overnight at 4°C |
| Anti-DRP1 primary antibody | Abcam | Mouse | 1:1000 | Overnight at 4°C |
| Anti-TSPO primary antibody | Abcam | Rabbit | 1:1000 | Overnight at 4°C |
| Total OXPHOS western blot antibody cocktail | Abcam | Mouse | 1:500-1:1000 | Overnight at 4°C |
| Anti-beta actin | Abcam | Mouse | 1:1000 | Overnight at 4°C/ 1 hr at room temperature |
| Anti-beta actin | St Johns Laboratory | Rabbit | 1:1000 | Overnight at 4°C/ 1 hr at room temperature |
| HRP conjugated anti-mouse secondary antibody | Abcam | Goat | 1:10,000 | 1 hr at room temperature |
| HRP conjugated anti-rabbit secondary antibody | Dako | Goat | 1:5000 | 1 hr at room temperature |

2.8. Brightfield imaging of iNPC-derived DA neuron-like cells

2 to 3 wells per cell line were imaged across each well throughout the differentiation protocol (days 15, 19, 22 and 27) using the InCell high content imager microscope. The same field of view is shown across multiple days for comparison.

2.9. Immunofluorescent staining

Cells were plated as per live cell imaging assays for all cell types. For fibroblasts, cells were fixed for 10 minutes using 4% paraformaldehyde diluted in PBS, before washing with PBS and storing at 4°C. For iNPC-derived DA neuron-like cells, cells were first fixed for 30 minutes in 1:1 ratio of cell media and 4% paraformaldehyde diluted in PBS. Following this, the cells were fixed for 10 minutes using 4% paraformaldehyde diluted in PBS, then washed with PBS and stored at 4°C. Sodium azide (0.4%) was added to the PBS for longer term storage of the cells.

Cells were permeabilised for 10 minutes using 0.1% Triton in PBS with Tween 20 1:1000 (PBST) and then washed twice in PBST. Cells were then incubated for 1 hour at room temperature in blocking solution, which composed of 5% horse serum diluted in PBST. Following this, cells were incubated in primary antibody diluted in blocking solution overnight at 4°C. Cells were then washed three times in PBST, before incubating in secondary antibodies (Alexa Fluor anti-rabbit 568, Alexa Fluor anti-mouse 488, and/or Alexa Fluor anti-chicken 488) diluted in PBST for 1 hour at room temperature, protected from light. Cells were washed three times in PBST, incubated with Hoechst (1 µM) for 2 minutes, washed a further three times in PBST, before adding PBS.

Cells were imaged using the Opera Phenix High Content Imaging System as described in section 2.9. Table 2.10 describes the primary antibodies used in immunofluorescent staining experiments.

Table 2.10. Primary antibodies used for immunofluorescent staining

| Antibody | Supplier | Species | Dilution | Incubation |
|---|-----------------|----------------|-----------------|-------------------|
| Anti-DRP1 primary antibody | BD Biosciences | Mouse | 1:1000 | Overnight at 4°C |
| Anti-TOM20 primary antibody | Santa Cruz | Rabbit | 1:1000 | Overnight at 4°C |
| Anti- β III tubulin (TuJ1) primary antibody | Millipore | Chicken | 1:1000 | Overnight at 4°C |
| Anti-tyrosine hydroxylase primary antibody | Abcam | Rabbit | 1:1000 | Overnight at 4°C |

2.10. siRNA knockdown experiments

At day 27 of differentiation control iNPC-derived DA neuron-like cells were treated with either 100 nM SCO2 siRNA SMART pool Accell probes (Horizon Discovery), 100 nM scramble siRNA-negative Accell probes in Accell delivery media, or Accell delivery media alone for different time points.

2.11. Opera Phenix image analysis

Images were analysed using Harmony analysis software (Perkin Elmer). Firstly, Z-stacks of images were combined into a maximum intensity projection image per field of view and basic flatfield correction applied. Nuclei were then segmented. Due to limitations of the analysis algorithm, it was not possible to always segment the whole cytoplasm of individual fibroblasts due to their length. Therefore, the mitochondria were segmented from the whole image region. This was completed by using the texture feature SER ridge to visualise the mitochondria, which were then segmented using the 'find spots' feature and filtered by staining intensity and size to remove any false positive segmentation. For cytoplasmic staining the image region was filtered by staining intensity to visualise the cell.

For iNPC-derived DA neuron-like cell assays, cells were instead segmented by cytoplasm region. This was in part because the staining was less homogenous in the neuron-like cells compared with the fibroblasts. Neuron-like cells were selected by their intensity and size to ensure that highly rounded small cells were removed. Individual mitochondria and lysosomes were segmented using the 'spot' parameter on the software and filtered by size to remove false positive segmentation. To determine basal mitophagy the number of lysosomes that overlapped directly with individual mitochondria were analysed. The same method was also used to assess DRP1 localisation in the fibroblast (**Figure 2.2**).

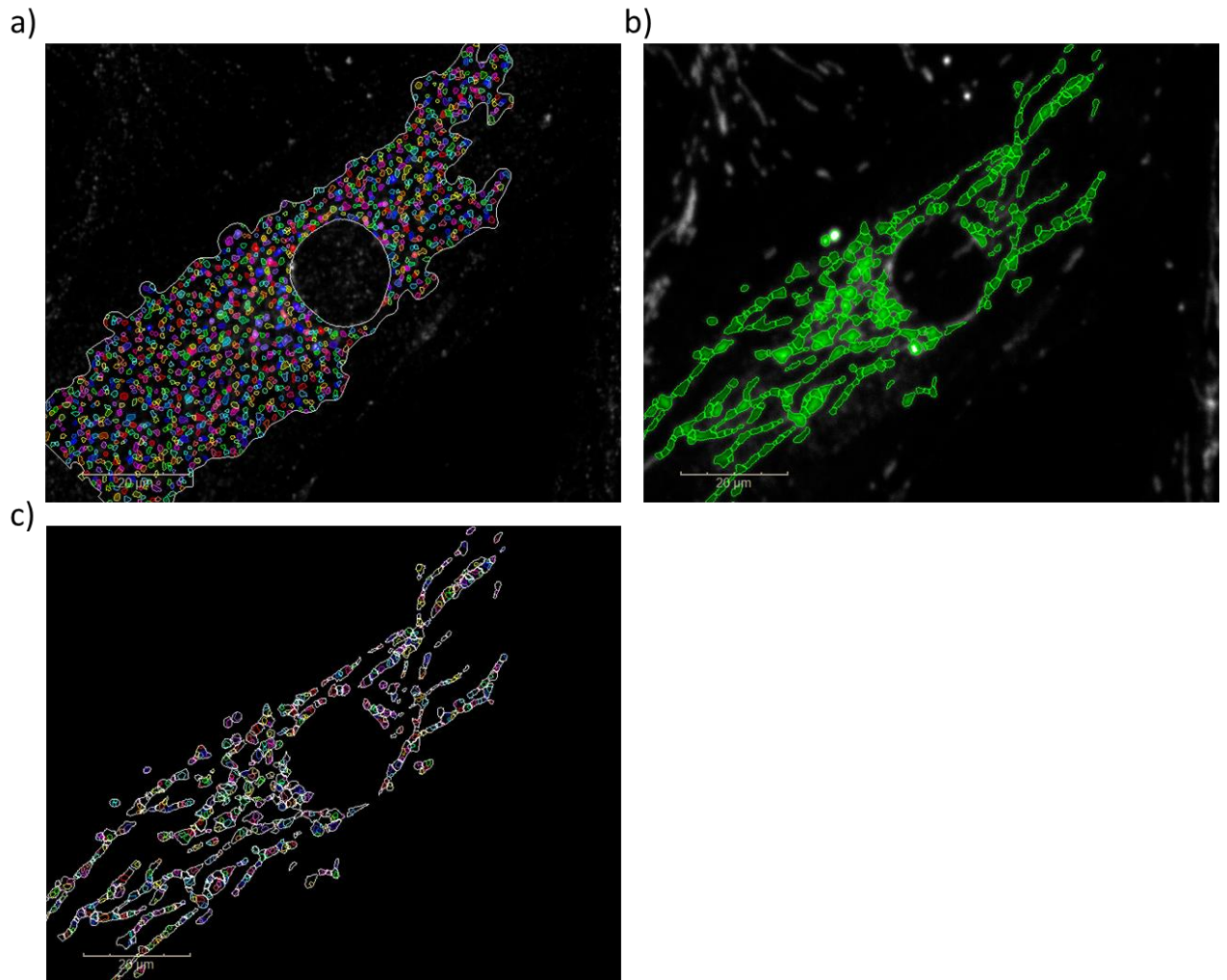


Figure 2.2. Example image of mitochondrial segmentation and DRP1 ‘spots’ found within the mitochondria.

a) Segmentation of DRP1 spots in the cytoplasm region. b) Segmentation of the mitochondria using TOM20. c) DRP1 spots found within the mitochondria. Image from control fibroblast.

2.12. Statistical analysis

Data analysis was completed in Microsoft Excel and then results transferred to GraphPad Prism for statistical analysis. $P < 0.05$ was deemed significant. Normality was tested using a Shapiro-Wilk test. For the comparison of two groups either a one sample t-test with a hypothetical mean of 100 (when comparing normalised datasets with no variance), an

unpaired t-test with Welch's correction, or a Mann-Whitney U test, was used. For comparison across multiple groups either a one-way ANOVA with Dunnett's multiple comparisons or a Kruskal Wallis with Dunn post-hoc test was used.

Chapter 3 **Analysis of mitochondrial dysfunction in LRRK2-G2019S fibroblasts**

3.1 Introduction

As described in the introductory chapter to this thesis, mitochondrial dysfunction is highly implicated in LRRK2-G2019S Parkinson's disease (PD). This chapter aims to characterise this mitochondrial dysfunction in more detail using primary human fibroblasts as a model.

Primary human fibroblasts are derived from 2 mm punch skin biopsies taken from the forearm. Skin biopsies are then cultured and both epithelial and fibroblast cells begin to grow around the surface of the skin. The fibroblasts are then separated from the epithelial cells using a short trypsinisation step which allows only the fibroblasts to detach. However, this cell culture still represents a fairly heterogenous cell population of both mitotic and post-mitotic fibroblasts (Bayreuther *et al.*, 1991; Auburger *et al.*, 2012).

Fibroblasts have commonly been used as a model to study neurodegenerative disease. They have an advantage of being generated from aged individuals via a relatively simple procedure and are much easier to obtain than post-mortem brain tissue. These patient-derived fibroblasts will already have the genetic mutations being studied, without the need to induce them. Hence, making them more physiologically relevant compared to immortalised cell lines.

The fibroblasts used in this study have been cultured from three different participant populations. Firstly, PD patients with the LRRK2-G2019S mutation, which will henceforth be referred to as 'manifesting'. Secondly, participants who have the LRRK2-G2019S mutation but have not been diagnosed with PD at the time of the skin biopsy, referred to as 'non-manifesting'. And thirdly, participants with neither the LRRK2-G2019S mutation, nor a

diagnosis of PD, referred to as 'healthy controls'. Currently, only a small minority of previous studies use patient-derived cells from a non-manifesting population. An advantage of using this population is that they give an opportunity to look at early changes that the LRRK2-G2019S mutation may induce, similar to a pre-clinical population. However, it can be difficult to detect changes in this population due to their heterogeneity.

Our group has previously looked at mitochondrial dysfunction in a small group of LRRK2-G2019S manifesting, LRRK2-G2019S non-manifesting and healthy control fibroblast lines (Mortiboys et al. 2010, 2015). Here, a decrease in ATP levels was observed in manifesting and non-manifesting lines compared with controls when cultured in galactose-containing media. This ATP deficit was ameliorated by treatment with either UDCA or UCA. In addition, there was a decrease in electron transport chain complex III and IV activity in manifesting and non-manifesting fibroblasts. The manifesting fibroblasts also displayed higher mitochondrial interconnectivity. We wanted to expand this work in further fibroblast lines we had obtained from these cohorts, as well as look more in depth at what may be causing these mitochondrial abnormalities.

3.1.1 *Aims and objectives*

The aim of this chapter was to investigate both functional and morphological mitochondrial differences in an expanded, not before investigated LRRK2-G2019S manifesting, non-manifesting and control fibroblasts. The specific objectives were to:

- Measure ATP levels
- Measure mitochondrial membrane potential
- Measure expression of mitochondrial complex subunits and proteins involved in mitochondrial complex III and IV assembly
- Evaluate changes in mitochondrial morphology and measure mitochondrial morphology protein expression

- Measure mitochondrial and cytosolic reactive oxygen species levels
- Assess the effect of UDCA and UCA on the above mitochondrial parameters

3.2 Results

3.2.1 *ATP levels in LRRK2-G2019S manifesting, non-manifesting, and control fibroblasts*

Production of ATP by the mitochondria is essential in fulfilling the cell's metabolic requirements. Fibroblasts have relatively low metabolic requirements in comparison to other cell types such as dopaminergic neurons, and mainly rely on glycolysis to generate ATP, particularly under glucose-rich cell culture conditions. As well as glycolysis, ATP can also be generated through oxidative phosphorylation in the mitochondria to produce higher net ATP levels. In order to direct fibroblasts to generate more of their ATP using oxidative phosphorylation, and thereby measure mitochondrial function, fibroblasts can be grown in galactose-containing media. As opposed to glycolysis with glucose as a substrate, when galactose is used there is no net generation of ATP. Indeed, fibroblasts with severe respiratory defects have reduced survival when cultured in galactose containing media (Hofhaus *et al.*, 1996). This is because the slow metabolism of galactose to glucose 1-phosphate is not sufficient for cells to synthesise the bulk of their ATP through glycolysis when OXPHOS is impaired. Therefore, dysfunctions in oxidative phosphorylation in fibroblasts can be unmasked using this method.

Total cellular ATP levels were measured in additional cell lines to the original cohort already published. LRRK2-G2019S manifesting (2 lines), LRRK2-G2019S non-manifesting (4 lines) and control fibroblast (3) lines cultured in either glucose or galactose-containing media (24-hour treatment). ATP levels were normalised to their DNA content, measured by a CyQuant assay. None of the G2019S lines (neither non-manifesting nor manifesting) showed alterations in ATP when grown in glucose media (**Figure 3.1 a**). However, non-manifesting-

4 had a significant reduction in ATP levels when cultured in galactose media (66% mean reduction compared with controls in galactose media; **Figure 3.1 a**). Manifesting-1 also showed a trend towards a decrease in ATP levels (36% mean reduction compared with controls in galactose media), though did not reach significance in this small cohort ($P=0.24$). **Figure 3.1 b** shows that the percentage change in ATP levels when cells are cultured in galactose media compared with glucose media. The controls showed an increase in ATP when switched to galactose media, as would be expected, as oxidative phosphorylation has a higher net production of ATP than glycolysis. The non-manifesting-3 and manifesting-1 cell lines showed no difference between media types, and ATP levels were significantly decreased in non-manifesting-4 when cultured in galactose media, suggesting a severe defect in oxidative phosphorylation.

One of the LRRK2-G2019S cell lines, manifesting-2, did not show any deficits in ATP when grown in galactose-containing media for 24 hours. Therefore, a further pilot experiment was run in which the cells were grown for a longer time point of 72 hours in galactose media (**Figure 3.1 c**). This showed no difference between cell lines, suggesting that there is no ATP defect in this manifesting line.

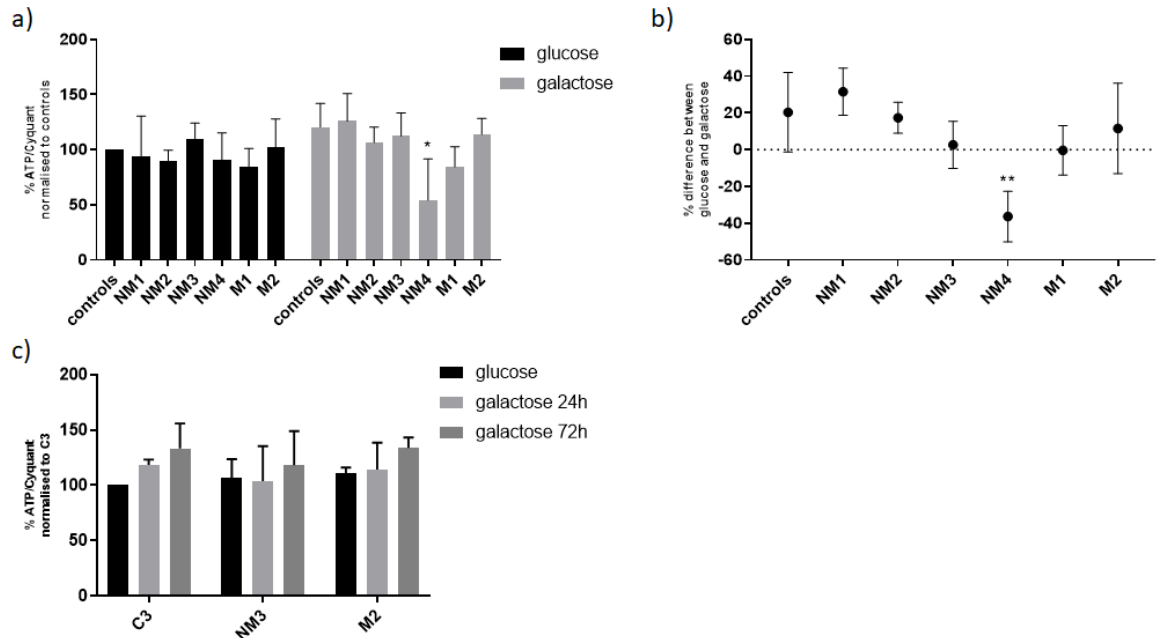


Figure 3.1. ATP levels in LRRK2-G2019S manifesting, non-manifesting and control fibroblasts.

Results are expressed as the mean \pm SD, LRRK2-G2019S manifesting (M), LRRK2-G2019S non-manifesting (NM), control (C) n=3 control lines pooled. (a) Percentage of total cellular ATP/Cyquant normalised to glucose media controls. *p<0.05 comparing galactose measurements using one-way ANOVA with Dunnett's multiple comparisons. (b) Percentage difference in normalised total cellular ATP levels between glucose and galactose media. **p<0.01 one-way ANOVA with Dunnett's multiple comparisons. Each line was repeated at least 3 times, with the exception of 1 control line due to poor growth. (c) Percentage of total cellular ATP/Cyquant normalised to glucose media control-3 at different galactose media timepoints (n= 2 experimental repeats).

3.2.2. Mitochondrial membrane potential in LRRK2-G2019S manifesting, non-manifesting, and control fibroblasts

As well as measuring total cellular ATP levels, mitochondrial function was also assessed by measuring mitochondrial membrane potential (MMP). MMP was measured using the cationic dye, Tetramethylrhodamine methyl ester (TMRM), which localises to mitochondria with an intact membrane potential. A lower TMRM signal suggests a disrupted membrane potential and decreased mitochondrial function. Carbonyl cyanide m-chlorophenylhydrazone CCCP, a mitochondrial uncoupler which disrupts the membrane potential, was used as a positive control of reduced TMRM staining (**Figure 3.2**). As shown in **Figure 3.2 c** there is no detectable difference in TMRM intensity between most of the cell lines. However, two lines, non-manifesting 2 and manifesting-1 show an increase in TMRM compared with controls. TMRM intensity shows the same pattern between media type and between short and long mitochondria, suggesting that neither media type nor the size of mitochondria is affecting the overall membrane potential.

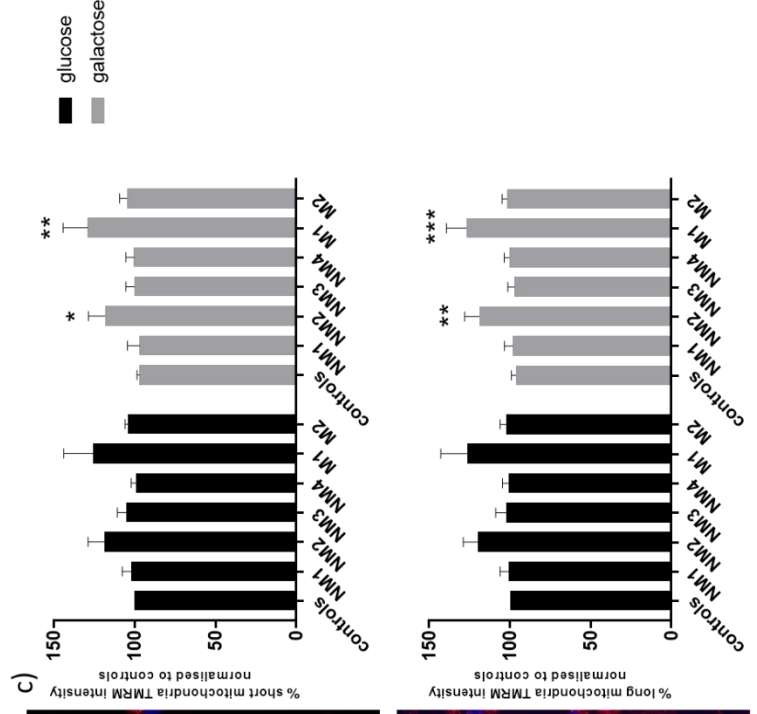
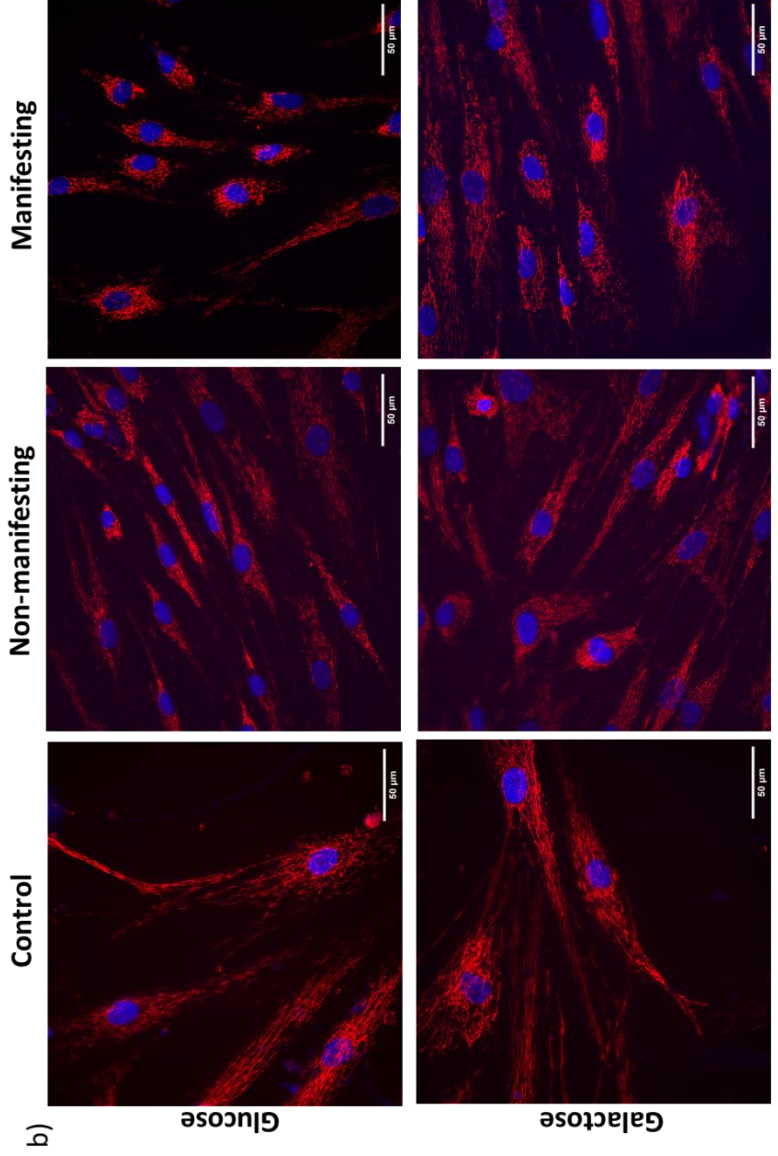
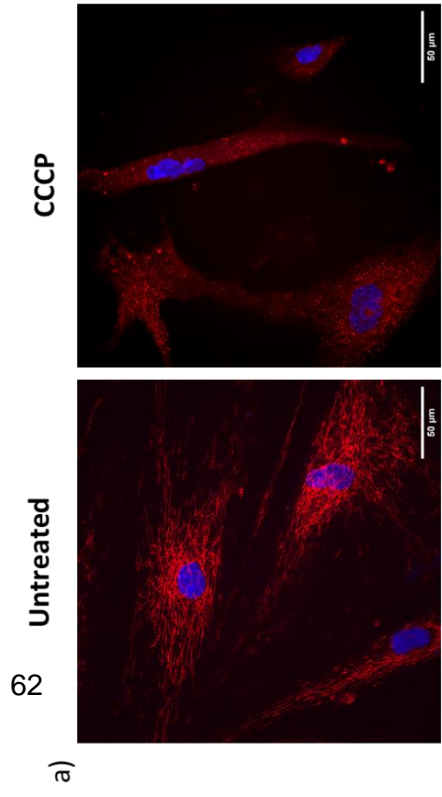


Figure 3.2. Mitochondrial membrane potential in LRRK2-G2019S manifesting, non-manifesting and control fibroblasts.

Results are expressed as the mean \pm SD, LRRK2-G2019S manifesting (M), LRRK2-G2019S non-manifesting (NM), control (C) n=3 control lines pooled. Each line was repeated at least 3 times, with 3 technical repeats, with the exception of 1 control line due to poor growth. (a) Representative images of TMRM staining for untreated and CCCP treated fibroblasts. (b) Representative images of TMRM staining for control, non-manifesting and manifesting fibroblasts in glucose and galactose media. Scale bar, 50 μ m. (c) % TMRM intensity normalised to glucose media controls in short (upper) and long (lower) mitochondria. *p<0.05, **p<0.01, ***p<0.001 one-way ANOVA with Dunnett's multiple comparisons.

3.2.3. Mitochondrial and cytosolic reactive oxygen species

Previous data has suggested an increase in reactive oxygen species (ROS) in LRRK2-G2019S PD cells (Heo *et al.*, 2010). However, there is very little literature exploring ROS in both LRRK2-G2019S manifesting and non-manifesting fibroblasts. In addition, the most commonly used probes to study ROS, such as the intracellular ROS probe dichlorodihydrofluorescein diacetate (DCFH-DA) and mitochondrial ROS probe MitoSox, have limitations. For example, there are several things that can react with DCFH and cause artefacts such as cytochrome c and redox active metals (Kalyanaraman *et al.*, 2012), and MitoSox is specific to superoxide so cannot reflect the overall redox status of its environment.

Our collaborator Professor Elizabeth New (University of Sydney) kindly provided us with two mitochondrial ROS probes, FRR2 and NpFR2, and one cytosolic ROS probe, NpFR1 (Yeow *et al.*, 2014b; Kaur *et al.*, 2015, 2016). These probes are not selective for specific ROS, but instead provide details of the overall redox status of their environments. In this

study, we looked at mitochondrial and cytosolic ROS levels in several LRRK2-G2019S manifesting, non-manifesting and control fibroblast cell lines, in both glucose media and after 24 hours in galactose containing media (**Figures 3.3 and 3.4**). Both mitochondrial ROS probes showed a similar pattern of results, thus further validating the results presented (**Figure 3.3 c and d**). There was no significant change in mitochondrial ROS between the different subgroups (glucose media manifesting, $101 \pm 19\%$; glucose media non-manifesting, $89 \pm 14\%$; galactose media manifesting, $109 \pm 21\%$; galactose media non-manifesting, $91 \pm 12\%$, galactose media control $100 \pm 11\%$; **Figure 3.3 c**). Interestingly, the LRRK2-G2019S manifesting line which did not have an ATP defect had the lowest mitochondrial ROS levels of the manifesting lines (**Figure 3.3 c**), thus further suggesting that this particular cell line does not have a mitochondrial phenotype. Some of the other LRRK2-G2019S manifesting lines showed a small increase in mitochondrial ROS compared to controls, while the non-manifesting lines had a trend towards a decrease, as can be seen from the shapes representing triplicate experimental repeats from a particular line in **Figure 3.3 c**. However, this data was variable between patient lines. No differences were observed between the different subgroups when looking at cytosolic ROS (**Figure 3.4 b**).

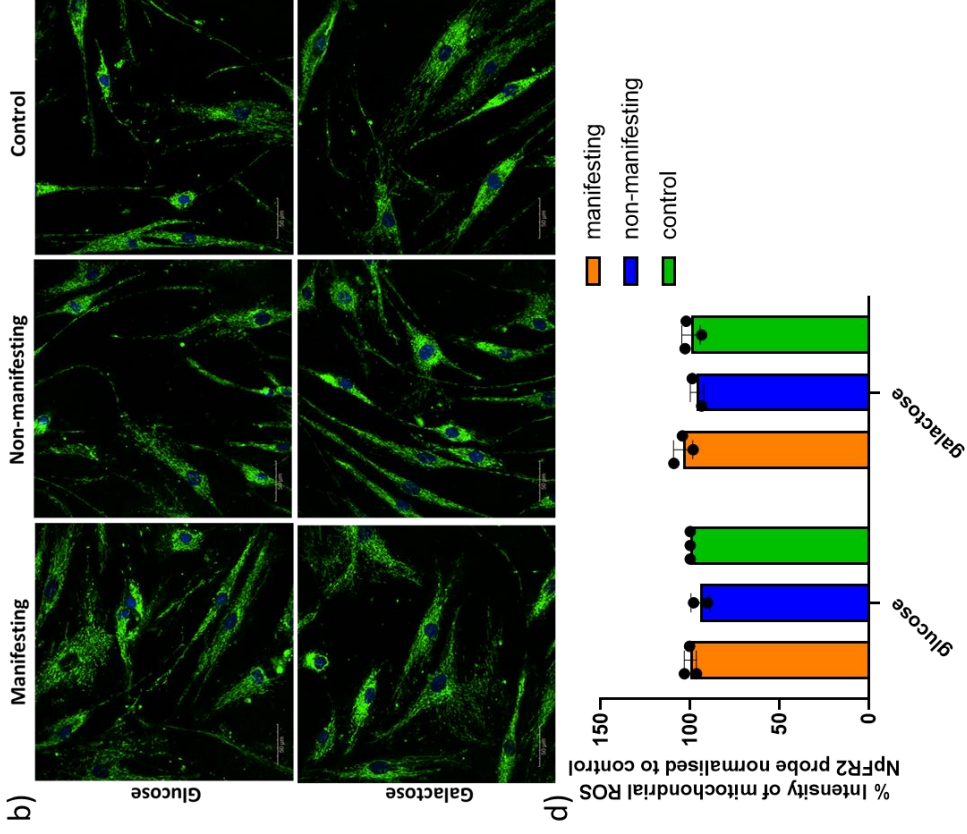
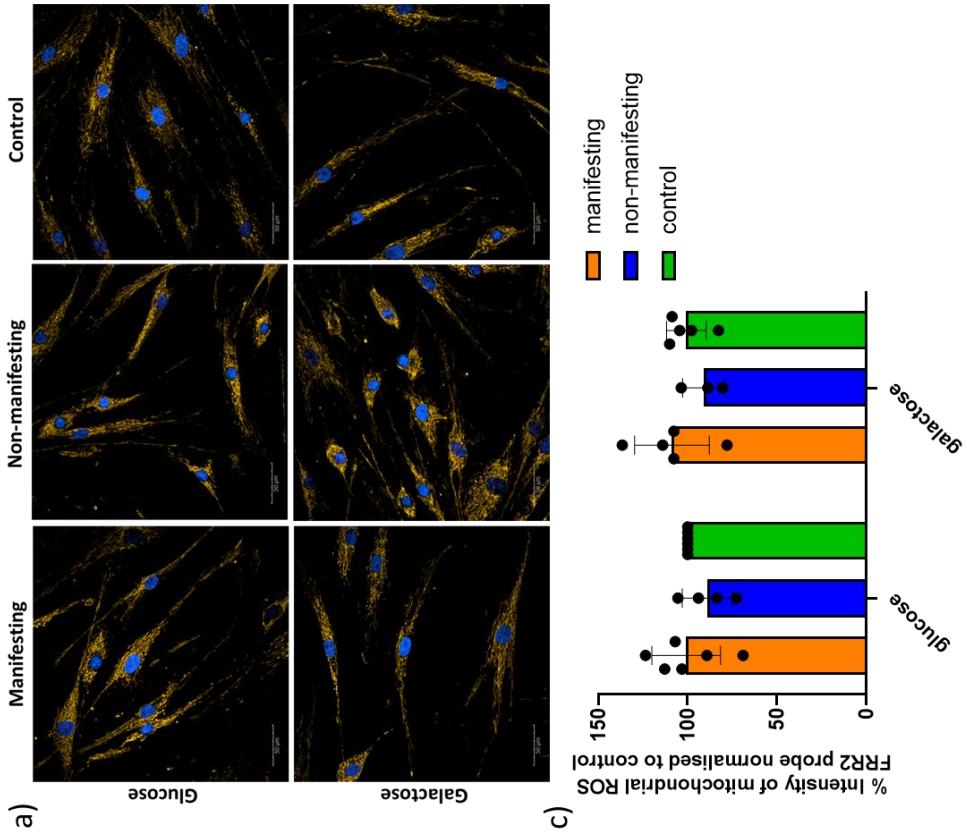


Figure 3.3. Mitochondrial reactive oxygen species levels in LRRK2-G2019S manifesting, non-manifesting and control fibroblasts.

a) Representative images of mitochondrial ROS probe FRR2 (orange) in LRRK2-G2019S manifesting, non-manifesting and control fibroblasts in glucose and galactose media. Scale bar, 50 μm . b) Representative images of mitochondrial ROS probe NpFR2 (green) in LRRK2-G2019S manifesting, non-manifesting and control fibroblasts in glucose and galactose media. Scale bar, 50 μm . c) Quantification of FRR2 intensity normalised to glucose media controls. $n = 6$ LRRK2-G2019S manifesting, 4 LRRK2-G2019S non-manifesting, 6 control fibroblast lines in glucose media and 5 LRRK2-G2019S manifesting, 3 LRRK2-G2019S non-manifesting, 5 control fibroblast lines in galactose media. Each line was repeated at least 3 times at different passages, with at least 2 technical repeats per biological repeat, with the exception of 1 manifesting and 1 control line in galactose media 1 control line in both media types, which had 2 experimental repeats, due to time constraints and poor growth. d) Quantification of NpFR2 intensity normalised to controls in glucose media. $n = 3$ LRRK2-G2019S manifesting, 2 LRRK2-G2019S non-manifesting, 3 control fibroblast lines in both media types. Each line was repeated 3 times at different passages, with 2 technical repeats per biological repeat, with the exception of 1 control line, which had 2 experimental repeats. Results are expressed as the mean \pm SD. Each dot represents the mean of the experimental repeats per line.

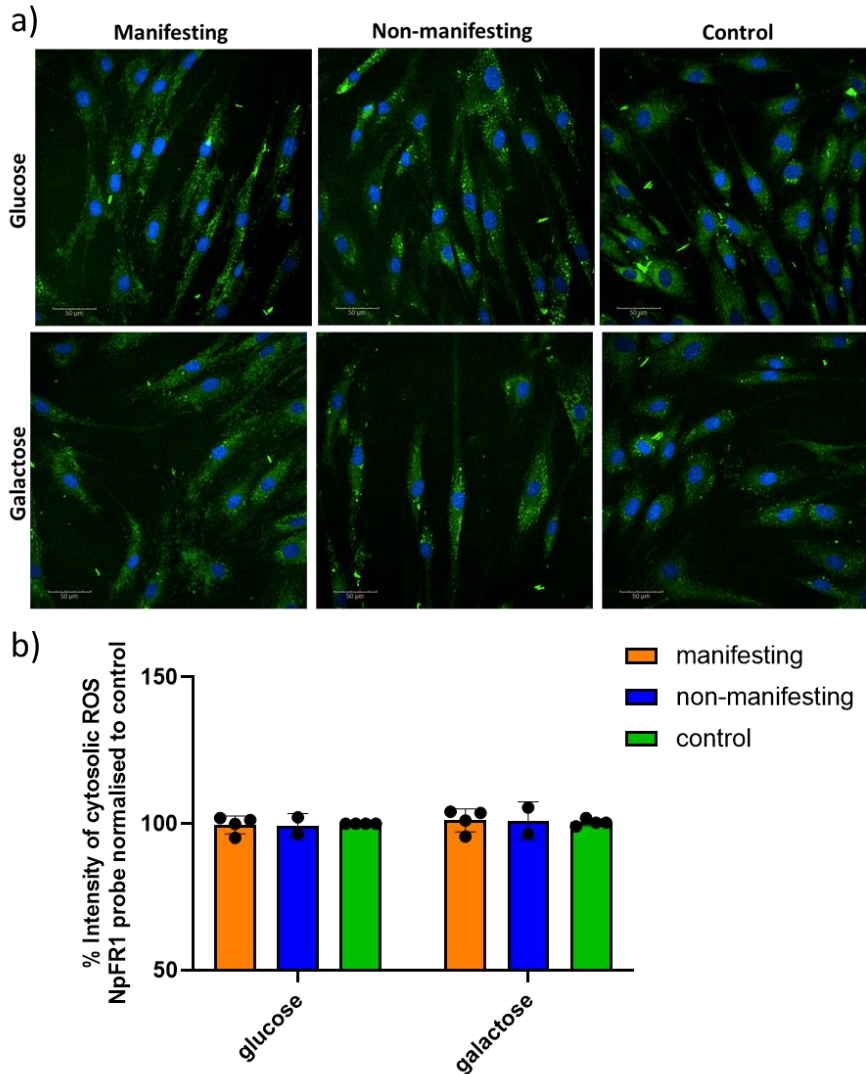


Figure 3.4. Cytosolic reactive oxygen species levels in LRRK2-G2019S manifesting, non-manifesting and control fibroblasts.

a) Representative images of cytosolic ROS probe NpFR1 (green) in LRRK2-G2019S manifesting, non-manifesting and control fibroblasts in glucose and galactose media. Scale bar, 50 μ m. b) Quantification of NpFR1 intensity normalised to controls in glucose media. $n = 3$ LRRK2-G2019S manifesting, 2 LRRK2-G2019S non-manifesting, 3 control fibroblast lines in both media types. Each line was repeated 3 times at different passages, with 2 technical repeats per biological repeat, with the exception of 1 control line, which had 2 experimental repeats. Results are expressed as the mean \pm SD. Each dot represents the mean of the experimental repeats per line.

3.2.4. Protein expression of mitochondrial complex subunits

Previous work by our group found that mitochondrial complexes III and IV activity are significantly decreased in both manifesting and non-manifesting LRRK2-G2019S fibroblasts (Mortiboys *et al.*, 2015). Therefore, we wanted to explore whether protein expression of the different mitochondrial oxidative phosphorylation (OXPHOS) complexes would be changed as well, potentially contributing to a decrease in activity. Western blots were performed using an antibody cocktail to look at specific subunits from the five mitochondrial complexes (**Figure 3.5**). These were then normalised to a beta-actin loading control, and then normalised to the control fibroblast complex subunit/beta-actin expression for each blot to allow comparison between experiments. As this is a novel area of investigation, the larger cohort of samples were investigated (which includes lines where the activity of the respiratory chain complexes has been published), in total 8 controls, 6 non-manifesting and 7 manifesting lines. The complex I subunit is particularly labile and could not be visualised on all blots, therefore has a lower sample size than the other complex subunits.

No significant difference was found between either LRRK2-G2019S manifesting or non-manifesting fibroblasts compared with controls in any of the mitochondrial complex subunits. There was a small, but non-significant decrease of 22% in the complex IV subunit in the LRRK2-G2019S fibroblasts compared with controls (**Figure 3.5 b**). As all of the LRRK2-G2019S manifesting fibroblasts in this study and previous work by the group showed an ATP deficit apart from manifesting-2 we decided to exclude this from the analysis on **Figure 3.5 c** to assess whether lines with an identified ATP deficit did show a decrease. We found that there was a decrease in the average protein expression levels for the LRRK2-G2019S manifesting fibroblasts when manifesting-2 was excluded of 26% but not enough to reach significance when compared with controls ($p=0.059$).

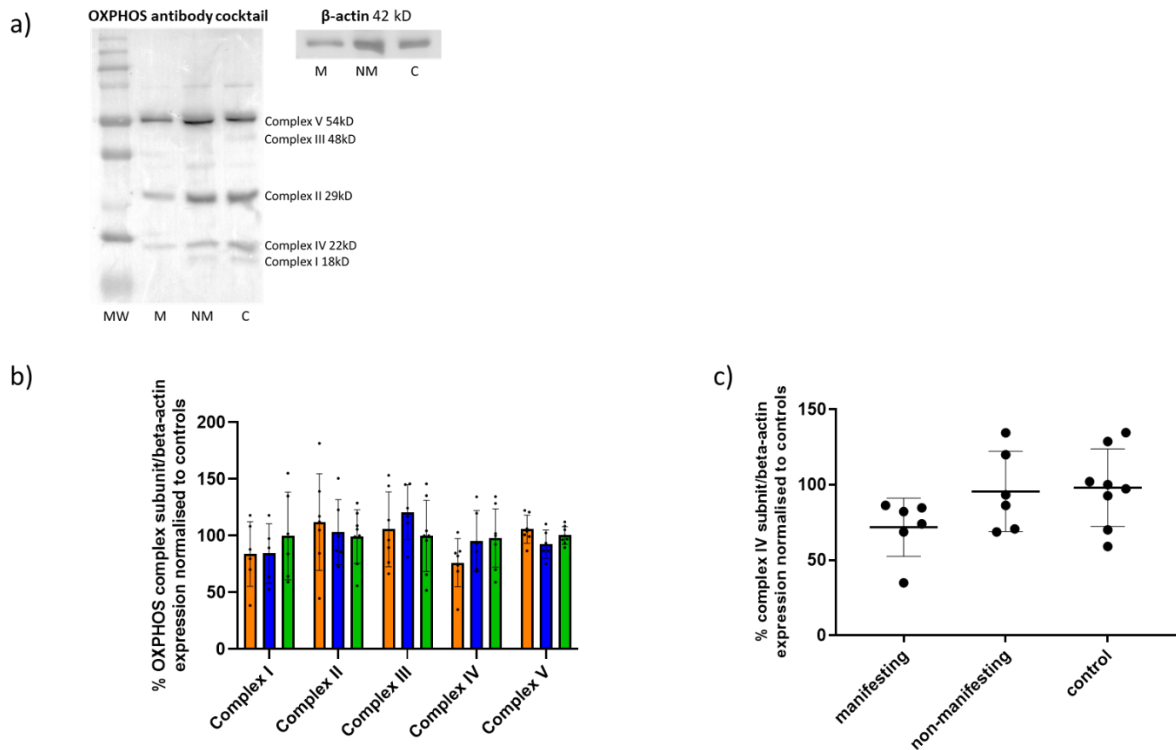


Figure 3.5. Protein expression of OXPHOS complex subunits in LRRK2-G2019S manifesting, non-manifesting and control fibroblasts.

(a) Representative western blot of the mitochondrial complex antibody cocktail and beta-actin. MW, molecular weight marker (b) Quantification of western blots showing the percentage of OXPHOS complex subunit/beta-actin expression normalised to controls. $n = 7$ LRRK2-G2019S manifesting (M), 6 LRRK2-G2019S non-manifesting (NM), 8 control (C) fibroblast lines. Complex I $n = 6$ LRRK2-G2019S manifesting, 5 LRRK2-G2019S non-manifesting, 6 control fibroblasts from at least 2 experimental repeats per line. Data for 3 manifesting and 3 control lines were generated by previous MSc student Harry Cooper, which was validated by repeats in some of these lines by Ruby Macdonald. (c) Quantification of complex IV subunit western blot excluding manifesting-2 which has no ATP deficit. $p = 0.059$ Mann-Whitney test. Results are expressed as the mean \pm SD. Each dot represents the mean of the experimental repeats per line.

3.2.5. Protein expression of complex III and IV assembly factors

As there was only a small amount of evidence to suggest a difference in expression levels of the mitochondrial complex subunits, we proposed the reduced activity of complex III and IV may be due to deficits in the assembly of these complexes. There are several known factors involved in the assembly of complexes III and IV. However, this study focused on BCS1L (complex III assembly factor) and SCO2 (complex IV assembly factor) due to them both being fundamental in the assembly of the catalytic core of their respective complexes, and the unreliability of other complex assembly factor antibodies for which optimisation was unsuccessful.

As can be seen in **Figure 3.6**, there was no change in BCS1L protein expression across either the manifesting ($108 \pm 35\%$) or non-manifesting groups ($80 \pm 12\%$). On the other hand, SCO2 expression levels were significantly reduced in the manifesting patient group by a mean of 38% (**Figure 3.7 b**). The non-manifesting lines were variable in SCO2 expression, with two lines showing much higher expression levels.

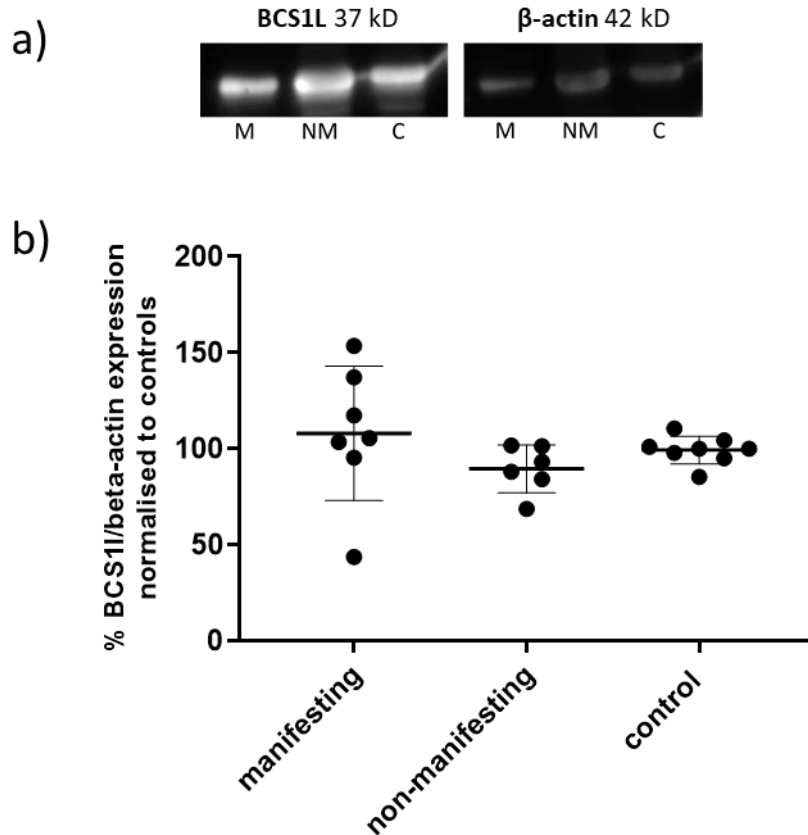


Figure 3.6. Protein expression of BCS1L in LRRK2-G2019S manifesting, non-manifesting and control fibroblasts.

(a) Representative western blot of BCS1L and beta-actin. (b) Quantification of western blots showing the percentage of Bcs1l/beta-actin expression normalised to controls. $n = 7$ LRRK2-G2019S manifesting (M), 6 LRRK2-G2019S non-manifesting (NM), 8 control (C) fibroblast lines from at least 2 experimental repeats per line. Data for 3 manifesting and 3 control lines were generated by previous MSc student Harry Cooper, which was validated by repeats in some of these lines by Ruby Macdonald. Results are expressed as the mean \pm SD. Each dot represents the mean of the experimental repeats per line.

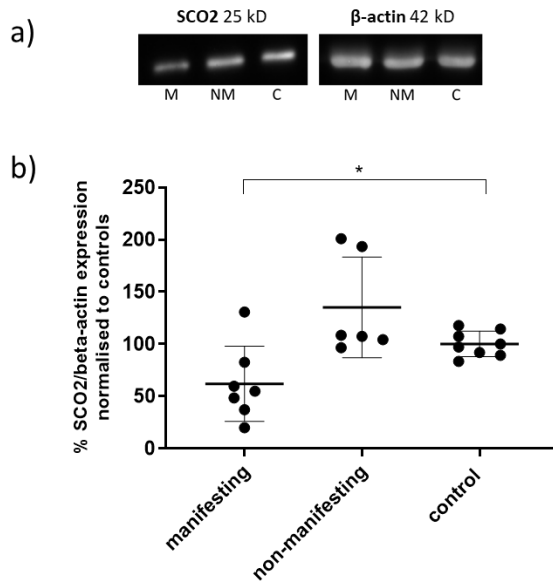


Figure 3.7. Protein expression of SCO2 in LRRK2-G2019S manifesting, non-manifesting and control fibroblasts.

(a) Representative western blot of SCO2 and beta-actin. (b) Quantification of western blots showing the percentage of SCO2/beta-actin expression normalised to controls. $n = 7$ LRRK2-G2019S manifesting (M), 6 LRRK2-G2019S non-manifesting (NM), 8 control (C) fibroblast lines from at least 2 experimental repeats per line. Data for 3 manifesting and 3 control lines were generated by previous MSc student Harry Cooper, which was validated by repeats in some of these lines by Ruby Macdonald. * $p < 0.05$ Mann-Whitney test.

3.2.6. Assessment of mitochondrial morphology

In addition to functional differences, changes in mitochondrial morphology have also been implicated in LRRK2-G2019S cells (Mortiboys *et al.*, 2010; Wang *et al.*, 2012). Therefore, we analysed mitochondrial morphology in cells stained with TMRM after culture in either glucose or galactose media (24-hour treatment). **Figure 3.8 a** shows a large amount of variation in mitochondrial count per cell area, but overall a trend towards an increased

number of mitochondria in both manifesting and non-manifesting lines compared with controls; this increase varies from a mean of 106% to 119% in the non-manifesting lines and 109% to 117% in the manifesting lines. There was also an increase in the percentage of perinuclear mitochondria, an indicator of cellular stress, by between a mean of 112% and 128% in non-manifesting and 105% and 125% in manifesting, compared with controls in fibroblasts cultured in galactose media (**Figure 3.8 b**).

Mitochondrial area showed variation between cell lines, with non-manifesting-2 and manifesting-1 showing a decrease (**Figure 3.8 c**). Therefore, we defined the mitochondria by two groups; short mitochondria and long mitochondria. There was a higher percentage of short mitochondria present in non-manifesting-2 with a mean of 115% and 115% and manifesting-1 with a mean of 125% and 121% compared with controls in glucose and galactose media, respectively (**Figure 3.8 d**). This difference was more pronounced when looking at the total mitochondrial area occupied by short mitochondria, where an increase in non-manifesting-4 of 118% and 124% in glucose and galactose media, respectively, was also present (**Figure 3.8 e**). Together, this suggests that certain LRRK2-G2019S manifesting and non-manifesting lines have more fragmented mitochondria compared to controls.

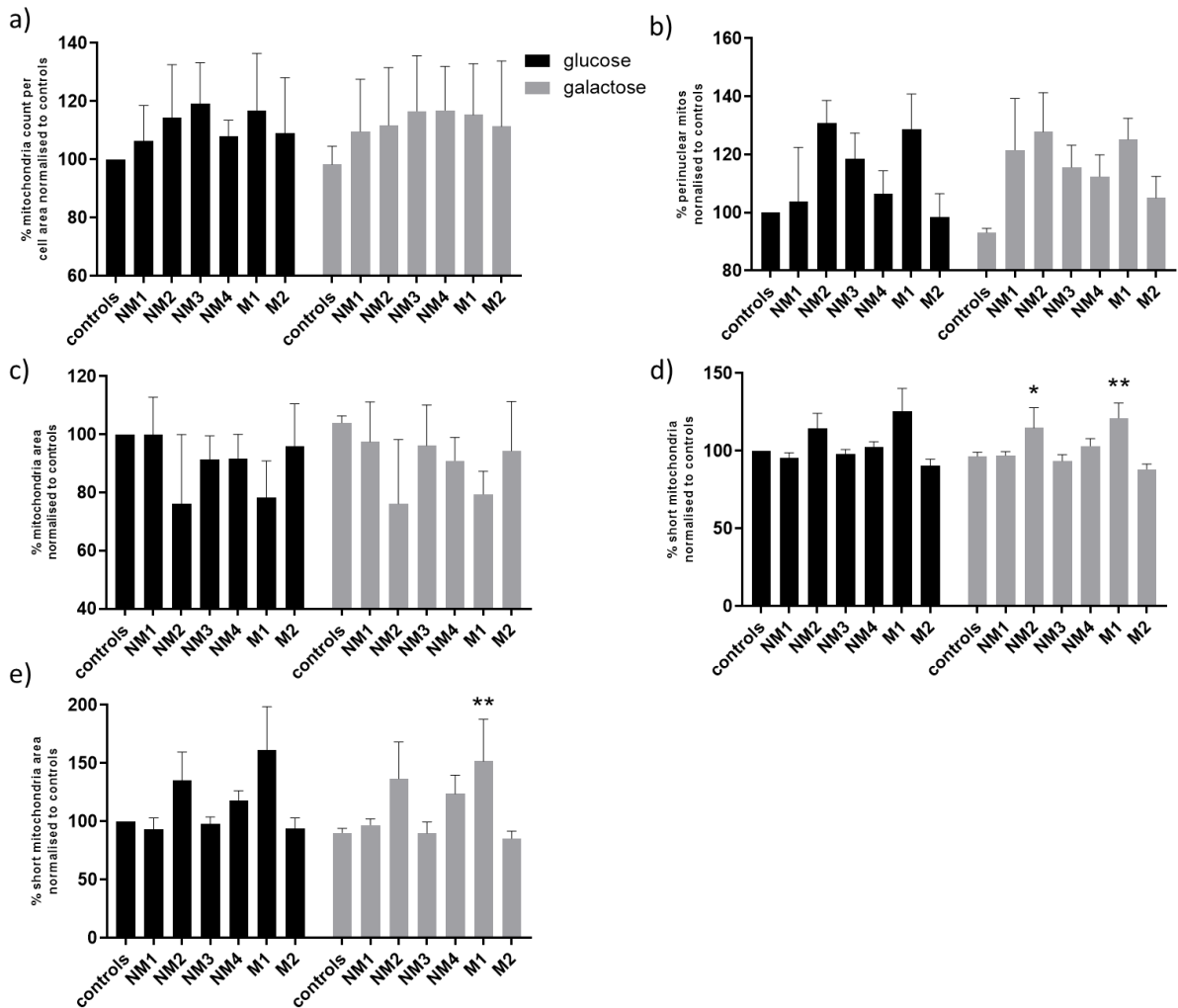


Figure 3.8. Mitochondrial morphology parameters from TMRM staining in LRRK2-G2019S manifesting, non-manifesting and control fibroblasts.

Results are expressed as the mean \pm SD, LRRK2-G2019S manifesting (M), LRRK2-G2019S non-manifesting (NM), control (C) n=3 control lines pooled. Each line was repeated at least 3 times at different passages, with 3 technical repeats per biological repeat, with the exception of 1 control line due to poor growth. (a) Number of mitochondria per cell area normalised to glucose media controls. (b) Percentage of perinuclear mitochondria normalised to glucose media controls. (c) Mean mitochondria area normalised to glucose media controls. (d) Percentage short mitochondria per total number of mitochondria normalised to glucose media controls. (e) Percentage of mitochondria area occupied by

short mitochondria normalised to glucose media controls. * $p < 0.05$, ** $p < 0.01$ one-way ANOVA with Dunnett's multiple comparisons.

3.2.7. Protein expression of mitochondrial morphology and fission/fusion factors

After investigating the mitochondrial morphology using microscopy we also wanted to investigate if these changes were due to alterations in the protein expression of the fission/fusion factors; in particular as changes in these have been implicated in LRRK2 mutant models by others (Wang *et al.*, 2012; Y.-C. Su and Qi, 2013).

In order to explore any changes in morphology, using western blotting we looked at expression levels of two proteins; Opa1 which is involved in mitochondria fusion, and Drp1 which is involved in mitochondrial fission. Two isoforms of each protein were seen in both Opa1 and Drp1 blots. For Opa1 we quantified relative expression for both isoforms separately as they produced very distinct bands and there is evidence that the long and short isoforms of Opa1 play different roles in mitochondrial fusion. For Drp1, we quantified both isoforms together as the bands were less distinct and currently the roles of the different isoforms are less well defined. No difference was observed in protein expression for either Opa1 isoforms (long isoform manifesting, $109 \pm 34\%$; long isoform non-manifesting, $117 \pm 33\%$; short isoform manifesting, $96 \pm 46\%$; short isoform non-manifesting, $106 \pm 26\%$), or Drp1 (manifesting $88 \pm 28\%$; non-manifesting, $61 \pm 40\%$), between manifesting, non-manifesting and control fibroblasts (**Figures 3.9 and 3.10**). There was however a decrease in DRP1 expression in the majority of the non-manifesting cell lines. Overall, however the expression of DRP1 is variable within the different groups, more so than that of other proteins probed in this thesis.

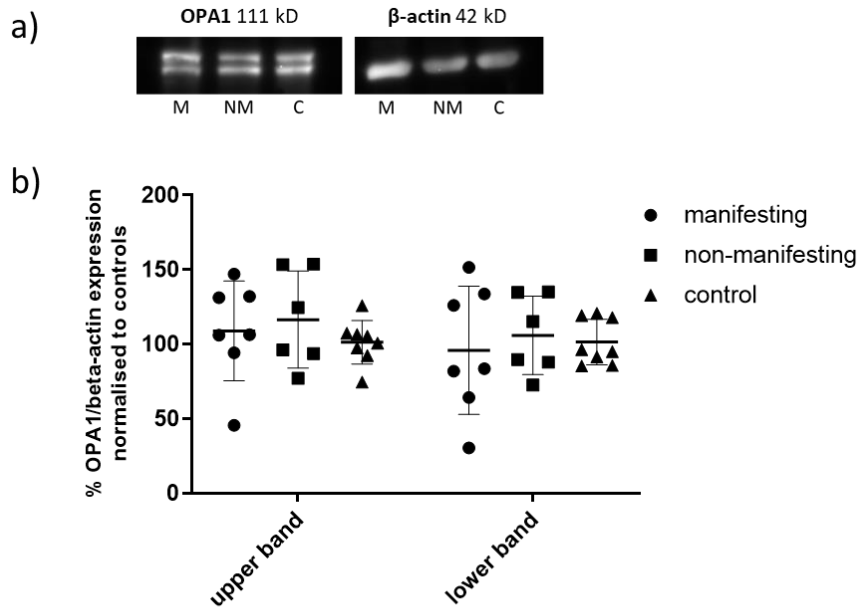


Figure 3.9. Protein expression of OPA1 in LRRK2-G2019S manifesting, non-manifesting and control fibroblasts.

(a) Representative western blot of OPA1 and beta-actin. (b) Quantification of western blots showing the percentage of Opa1/beta-actin expression normalised to controls for upper and lower bands. $n = 7$ LRRK2-G2019S manifesting (M), 6 LRRK2-G2019S non-manifesting (NM), 8 control (C) fibroblast lines from at least 2 experimental repeats per line. Results are expressed as the mean \pm SD. Each dot represents the mean of the experimental repeats per line.

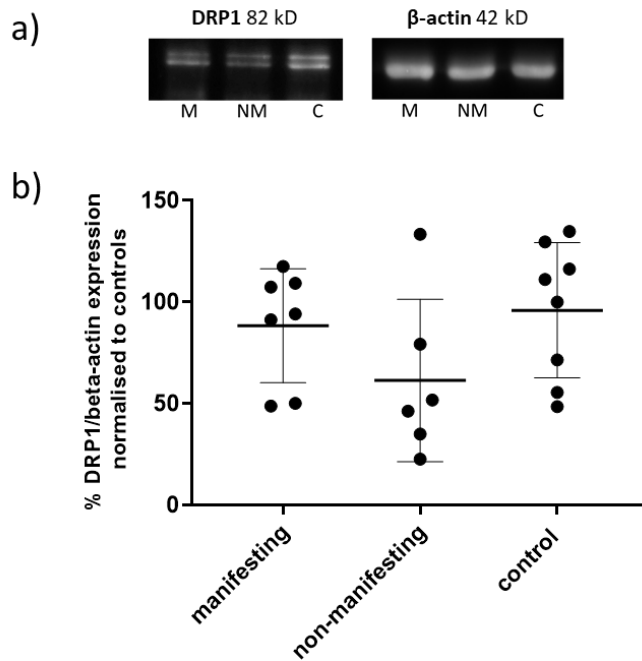


Figure 3.10. Protein expression of DRP1 in LRRK2-G2019S manifesting, non-manifesting and control fibroblasts.

(a) Representative western blot of DRP1 and beta-actin. SCO2 and DRP1 were probed on the same blot, therefore share the same beta-actin image (b) Quantification of western blots showing the percentage of DRP1/beta-actin expression normalised to controls. $n = 7$ LRRK2-G2019S manifesting (M), 6 LRRK2-G2019S non-manifesting (NM), 8 control (C) fibroblast lines from at least 2 experimental repeats per line. Results are expressed as the mean \pm SD. Each dot represents the mean of the experimental repeats per line.

3.2.8. *DRP1 localisation*

The data generated in this section was by Olivia Cracknell (OC), a TA SURE summer placement student primary supervised by Ruby Macdonald (RM). For this, RM designed and obtained funding for the summer placement project. RM plated and treated 2 sets of LRRK2-G2019S manifesting, non-manifesting and control fibroblasts and OC plated and treated 1 set. OC completed the staining for all fibroblasts and RM analysed the data.

As DRP1 is a cytosolic protein and is recruited to the mitochondrial outer membrane for mitochondrial fission, we also investigated the localisation of DRP1. To this end, LRRK2-G2019S manifesting, non-manifesting and control fibroblasts were cultured in either glucose or galactose-containing media for 24 hours. Cells were then stained with DRP1 and translocase of outer membrane (TOM20), a mitochondrial outer membrane marker. **Figure 3.11** shows representative staining of the different cell lines, where DRP1 can be seen in both the cytoplasm and localised with TOM20.

In order to determine DRP1 localisation we segmented different parts of the cell for data analysis using Harmony analysis software. The cytoplasm region of the cell was segmented to determine the DRP1 intensity within the cytoplasm, and the mitochondria were segmented using the TOM20 stain. We could not directly analyse colocalization of DRP1 and TOM20 using Harmony analysis software. Therefore, DRP1 'spots' were segmented and DRP1 spots within the mitochondria were determined. This is described in further detail in Chapter 2.

Firstly, the intensity of DRP1 in the cytoplasm was calculated (**Figure 3.12 a**), as well as the intensity of DRP1 spots in the mitochondria (**Figure 3.12 b**). For both of these parameters, we observed an increase in DRP1 intensity when cells were grown in galactose-containing media. There was also a small decrease in cytoplasmic DRP1

intensity in the LRRK2-G2019S lines compared to glucose media controls (test significance). Interestingly, a decrease in TOM20 intensity was also observed in the LRRK-2019S non-manifesting fibroblasts compared to controls.

The number of mitochondria per cell area were calculated to determine whether this would be less variable than the TMRM staining data presented in **Figure 3.8 a**. However, the number of mitochondria was also variable when cells were stained with TOM20 (glucose media manifesting, $101 \pm 11\%$; glucose media non-manifesting, $102 \pm 11\%$; galactose media manifesting, $103 \pm 11\%$; galactose media non-manifesting, $106 \pm 10\%$, galactose media control $107 \pm 6\%$; **Figure 3.12 d**).

To assess whether there was an increase in DRP1 localization to the mitochondria, we analysed two parameters; the number of DRP1 spots that were found with the mitochondria compared to the total number of DRP1 spots, and the number of DRP1 spots per mitochondrial area (**Figure 3.12 e and f**). In two of the three lines LRRK2-G2019S manifesting lines tested there was a small increase in the number of DRP1 spots in the mitochondria (glucose media manifesting, $104 \pm 6\%$; glucose media non-manifesting, $101 \pm 2\%$; galactose media manifesting, $103 \pm 7\%$; galactose media non-manifesting, $102 \pm 2\%$, galactose media control $101 \pm 2\%$; **Figure 3.12 e**). This suggests that it may be useful to test this parameter in additional cell lines to determine whether this is a common occurrence. There were no observable differences between subgroups in the number of DRP1 spots per mitochondrial area (**Figure 3.12 f**). This suggests that if there was an increased movement of DRP1 from the cytoplasm to the mitochondria, then this may not affect the overall amount of DRP1 in the mitochondria. Overall, these findings suggest minimal changes in DRP1 localization at basal conditions.

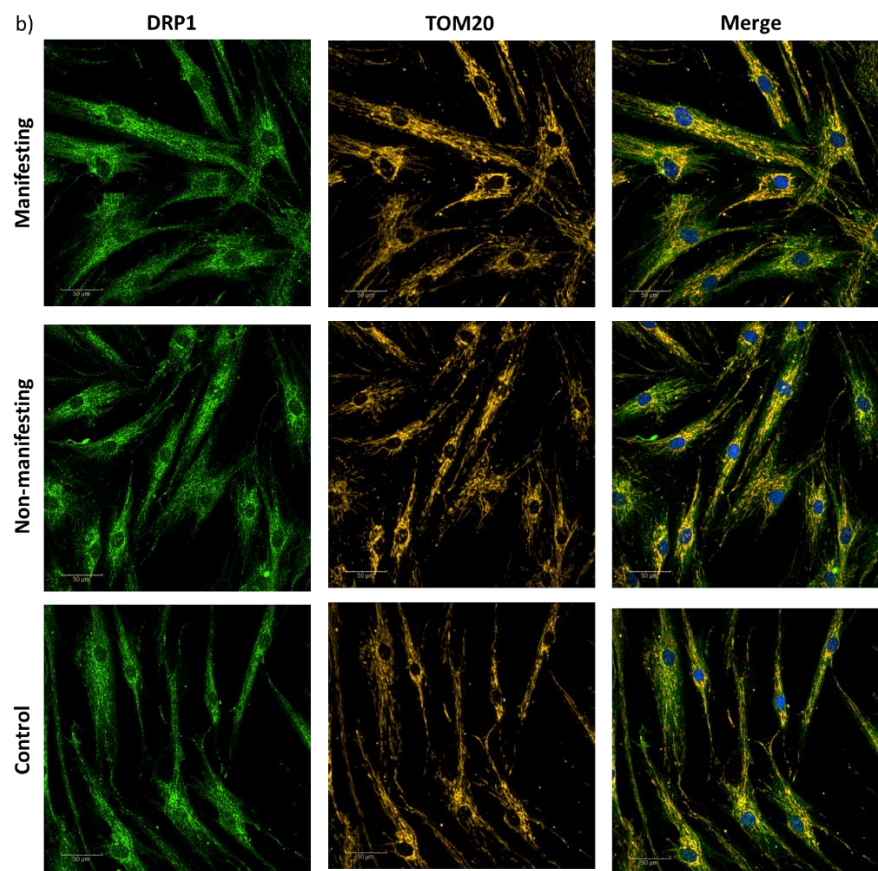
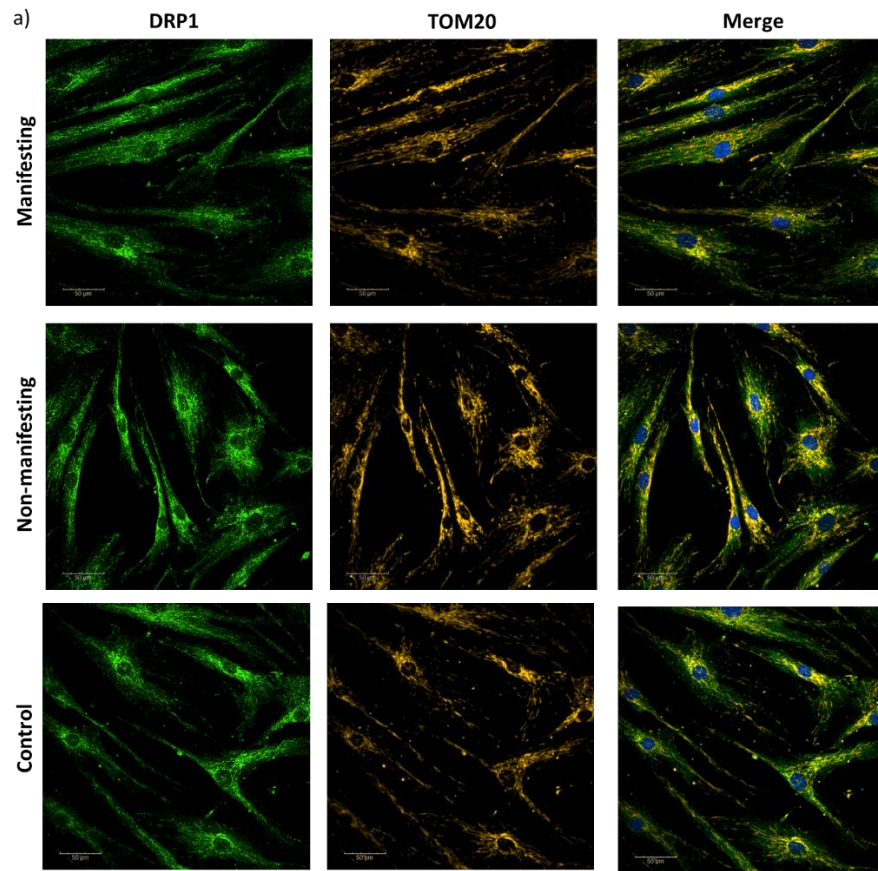


Figure 3.11. DRP1 localisation staining of LRRK2-G2019S manifesting, non-manifesting and control fibroblasts.

Representative staining images of DRP1 (green) and TOM20 (orange) in LRRK-2019S manifesting, non-manifesting and control fibroblasts. TOM20 was used as a mitochondrial marker and Hoechst (blue) was used to label nuclei. (a) cells in glucose media (b) cells in galactose-containing media for 24 hours. Scale bar, 50 μ m.

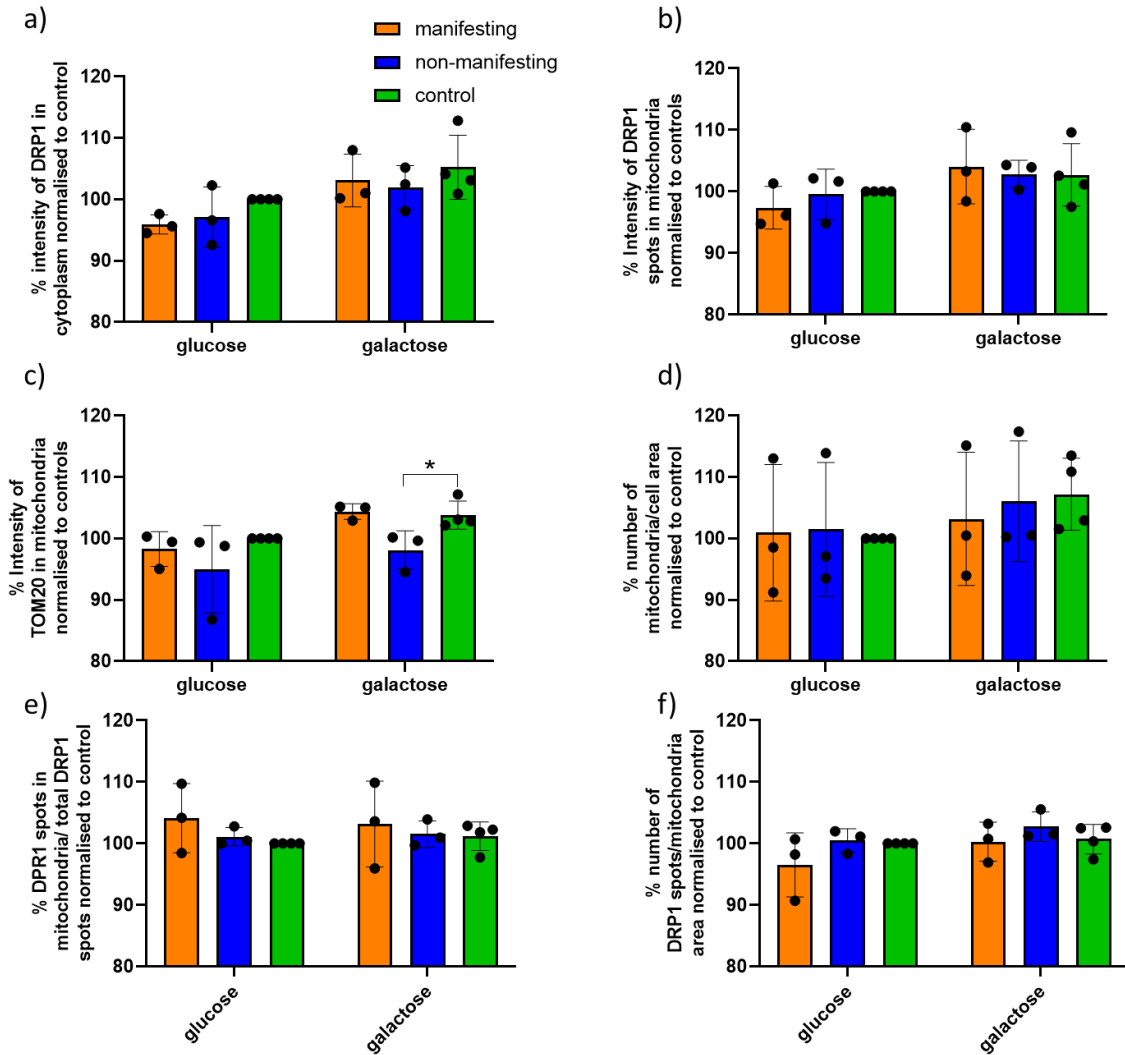


Figure 3.12. Quantification of DRP1 staining.

(a) Results are expressed as the mean \pm SD, $n = 3$ LRRK2-G2019S manifesting, 3 LRRK2-G2019S non-manifesting and, 4 control fibroblast cell lines. Due to the growth of the cells and the time of the summer project, variable number of experimental repeats were obtained for different control lines, 3 experimental repeats were obtained from 2 controls, 2 experimental repeats of 1 control, and 1 experimental repeat of 1 control. For LRRK2-G2019S manifesting and non-manifesting lines 3 experimental repeats were obtained. (a) Intensity of DRP1 staining in cytoplasm normalised to glucose media controls. (b) Intensity of DRP1 spot staining in mitochondria normalised to glucose media controls. (c) Intensity of TOM20 mitochondria staining normalised to glucose media controls. (d) Number of mitochondria per cell area normalised to glucose media controls. (e) Percentage DRP1

spots in mitochondria per total number of DRP1 spots normalised to glucose media controls
(f) Number of DRP1 spots per mitochondrial area normalised to glucose media controls.
* $p < 0.05$ one-way ANOVA with Dunnett's multiple comparisons. Each dot represents the mean of the experimental repeats per line.

3.2.9. Potential mechanisms of UDCA and UCA

Our group previously showed that UDCA and UCA improve ATP levels in LRRK2-G2019S fibroblasts (Mortiboys, Aasly and Bandmann, 2013; Mortiboys *et al.*, 2015), therefore it is important to determine the mechanism of action of these therapeutics.

Both UDCA and UCA are bile acids or bile acid like compounds. UDCA is produced naturally in the human body. Research has shown that UDCA and UCA can activate the same cellular systems as naturally occurring bile acids and also cholesterol. Translocator protein (TSPO) is localised to the outer mitochondrial membrane and binds to cholesterol, which UDCA and UCA help regulate (Tu *et al.*, 2016). TSPO is also thought to be involved in bile acid biosynthesis. Therefore, modulation of TSPO is an obvious potential mechanism by which UDCA and UCA could elicit a mitochondrial effect. We wanted to see whether there were any changes in TSPO expression in LRRK2-G2019S fibroblasts, in order to look at a potential mechanism of action for UDCA/UCA. We found no observable difference in TSPO expression between subgroups (manifesting, $100 \pm 23\%$; non-manifesting, $93 \pm 39\%$; **Figure 3.13**).

We also tested whether UDCA or UCA affected the protein expression of some of the other proteins studied. **Figure 3.14** shows a representative western blot. Results from these experiments were variable and did not point towards an effect of UDCA or UCA, therefore these experiments were not undertaken further.

Although ROS levels were not significantly altered in untreated LRRK2-G2019S, we wanted to determine whether ROS levels may have been altered in UDCA or UCA treated cells due to their effect on the mitochondria. As can be seen in **Figure 3.15**, there was no significant change in either mitochondrial or cytosolic ROS levels when cells were treated with UDCA. UCA, on the other hand, had a trend towards a small decrease in mitochondrial ROS levels in LRRK2-G2019S manifesting, non-manifesting and control fibroblasts. This was observed using both mitochondrial ROS probes.

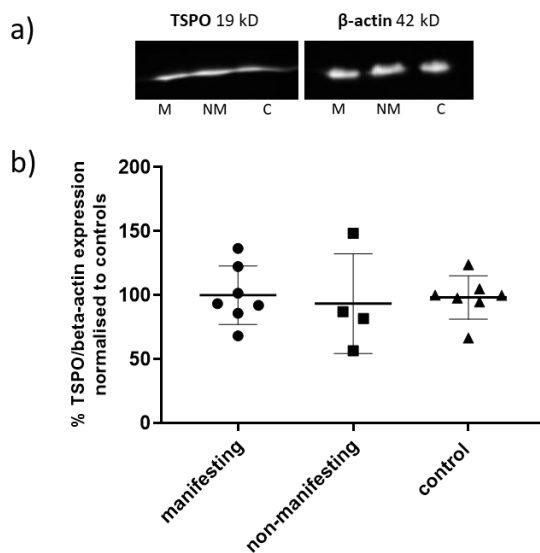


Figure 3.13. Protein expression of TSPO in LRRK2-G2019S manifesting, non-manifesting and control fibroblasts.

(a) Representative western blot of TSPO and beta-actin/ (b) Quantification of western blots showing the percentage of Tspo/beta-actin expression normalised to controls. n = 7 LRRK2-G2019S manifesting (M), 4 LRRK2-G2019S non-manifesting (NM), 7 control (C) fibroblast lines from at least 2 experimental repeats per line. Results are expressed as the mean \pm SD. Each dot represents the mean of the experimental repeats per line.

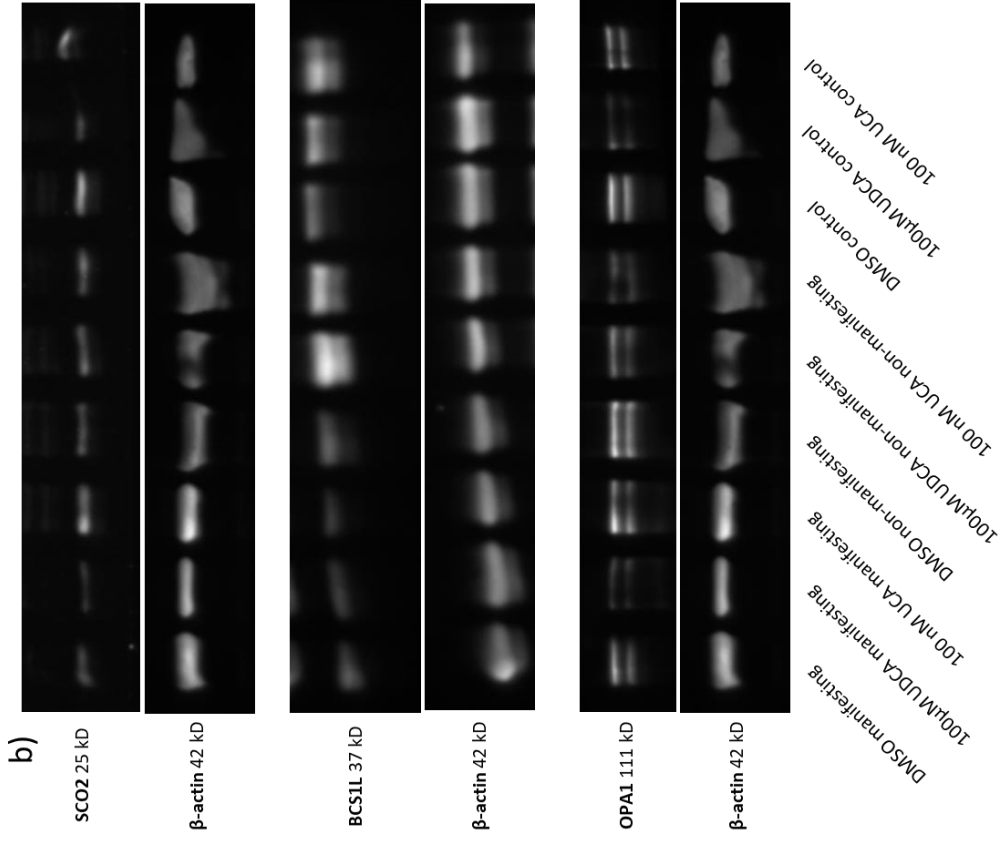
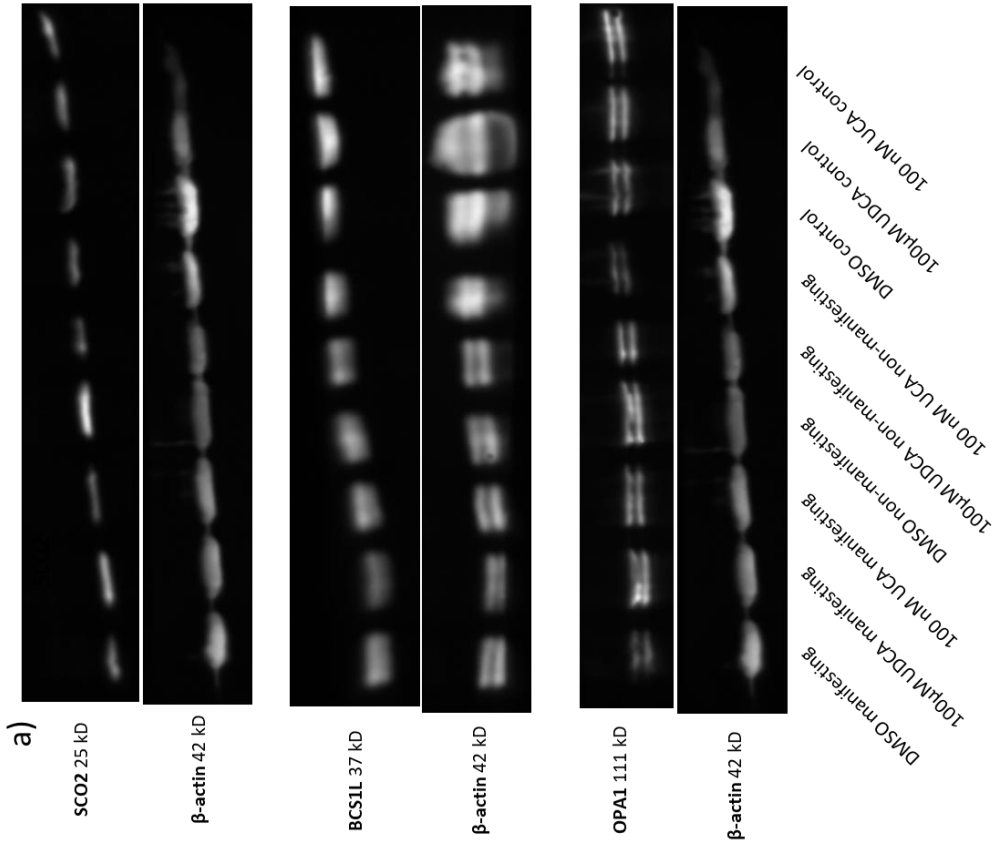


Figure 3.14. Protein expression of SCO2, BCS1L and OPA1 in UDCA and UCA treated fibroblasts.

Representative western blots of SCO2, BCS1L, OPA1 and beta-actin in cells treated with DMSO, UDCA 10 μ M or UCA 100 nM in either (a) glucose media or (b) galactose-containing media for 24 hours. SCO2 and OPA1 were probed on the same membrane so share the same loading control.

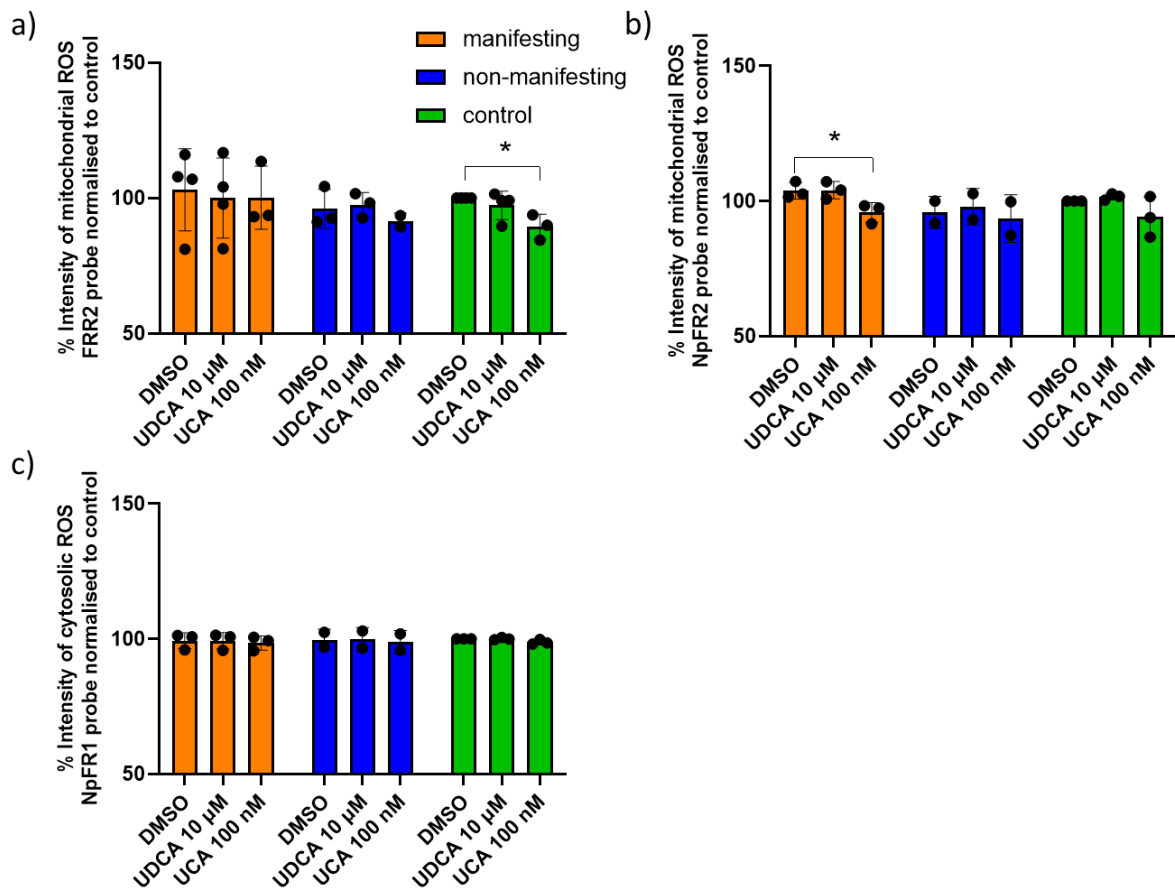


Figure 3.15. Effect of UDCA and UCA on mitochondrial and cytosolic reactive oxygen species in LRRK2-G2019S manifesting, non-manifesting and control fibroblasts.

LRRK2-2019S manifesting, non-manifesting and control fibroblasts were treated with either DMSO, UDCA 10 μ M, or UCA 100 nM for 24 hours and then staining with mitochondrial or cytosolic ROS probes. a) Quantification of FRR2 intensity normalised to DMSO controls. n

= 4 LRRK2-G2019S manifesting, 3 LRRK2-G2019S non-manifesting, 4 control fibroblasts lines for DMSO and UDCA treatment, and n = 3 LRRK2-G2019S manifesting, 2 LRRK2-G2019S non-manifesting, 3 control fibroblasts lines for UCA treatment. b) Quantification of NpFR2 intensity normalised to DMSO controls. n = 3 LRRK2-G2019S manifesting, 2 LRRK2-G2019S non-manifesting, 3 control fibroblasts lines. c) Quantification of NpFR1 intensity normalised to DMSO controls. n = 3 LRRK2-G2019S manifesting, 2 LRRK2-G2019S non-manifesting, 3 control fibroblasts lines. Results are expressed as the mean \pm SD. Each line was repeated 3 times, with at least 2 technical repeats per biological repeat, with the exception of 1 control line, which had 2 experimental repeats. * $p < 0.05$ Kruskal Wallis with Dunn's multiple comparisons for control data, or one-way ANOVA with Dunnett's multiple comparisons for manifesting data. Each dot represents the mean of the experimental repeats per line.

A summary table of the results of the assays in Chapters 3 and 5 from individual LRRK2-G2019S manifesting and non-manifesting fibroblast lines can be found in **Appendix B**.

3.3. Discussion

Fibroblasts are a commonly used model to assess mitochondrial dysfunction in PD as they are relatively easy to obtain and are more physiologically relevant than immortalised cell lines. In this chapter, data was presented from one of the largest cohorts studied thus far of both non-manifesting and manifesting LRRK2-G2019S PD fibroblasts. One of the main advantages of the present study was that cells were observed under physiological conditions rather than being exposed to mitochondrial toxins such as MPTP and rotenone, which may not fully represent the 'real-world' situation in PD.

3.3.2. ATP levels

Previous studies on mitochondrial activity have observed differences in mitochondrial function 24 hours of galactose treatment (Aguer *et al.*, 2011; González-Casacuberta *et al.*, 2019). This time point was also chosen to allow comparability to concurrent studies that

were being performed in drug screening studies on idiopathic PD fibroblast samples by other members of our research group. In this study, we found evidence of reduced ATP levels in LRRK2-G2019S fibroblasts in cells which were grown in media containing galactose, but no difference was observed when cells were grown in glucose media. ATP deficits have been observed in LRRK2-G2019S patient fibroblasts in other studies (Mortiboys *et al.*, 2010, 2015; Papkovskaia *et al.*, 2012). Mortiboys *et al.* 2015 observed a more marked decrease in ATP in both LRRK2-G2019S manifesting and non-manifesting fibroblasts than that observed in this study, using different cell lines from the same cohort. This may be due to the length of time cells were grown in galactose media, 24 h in this study vs. 72 h in the Mortiboys *et al.* 2015 study. On the other hand, a significant difference in ATP production was not observed in either glucose or galactose media in a large cohort of LRRK2-G2019S manifesting (n=6), non-manifesting (n=7) and control (n=8) fibroblasts, with high levels of variability in the different cell lines examined (Juárez-Flores *et al.*, 2018).

One of the manifesting lines studied in this thesis did not show any ATP deficit in galactose media. Interestingly, this cell line did not have the same mitochondrial phenotype as the other LRRK2-G2019S manifesting lines in other parameters such as SCO2 protein expression and mitochondrial ROS levels. This suggests that mitochondrial dysfunction may not be present in all cases of LRRK2-G2019S PD. A recent study by Carling *et al.* 2020 investigated mitochondrial and lysosomal function in fibroblasts of 100 sporadic PD patients and 50 controls (Carling *et al.*, 2020). They found that there were distinct subgroups of sporadic PD fibroblasts with mitochondrial or lysosomal dysfunction. This may be the same in LRRK2-G2019S PD and warrants further investigation in additional cell lines.

3.3.3. MMP

In our study, LRRK2-G2019S manifesting and non-manifesting fibroblasts showed either no change or an increase in MMP compared to controls, which is contrary to some of the previous literature on LRRK2-G2019S patient cells. There have been multiple studies showing a decrease in MMP in LRRK2-G2019S manifesting fibroblasts compared to controls (Papkovskaia *et al.*, 2012; Grünewald *et al.*, 2014; Mortiboys *et al.*, 2015). In glucose media, a significant increase has also been observed in the percentage of depolarised mitochondria in LRRK2-G2019S non-manifesting fibroblasts compared with controls (Juárez-Flores *et al.*, 2018). On the contrary, Ludtmann *et al.* 2019 observed no difference in MMP in LRRK2-G2019S, R1441G (ROC domain mutation) or Y1699C (COR domain mutation) fibroblasts compared with controls (Ludtmann *et al.*, 2019). However, only 1 fibroblast cell line per LRRK2 mutation was assessed in this study. The reasons for the discrepancy with the MMP results in our study and the literature is unclear. One potential reason could be the methodology used. To assess TMRM intensity levels in our study, the InCell microscope was used, which is unable to image z-stacks. Although fibroblasts are a relatively 'flat' cell type, there could be instances where the height of the image taken might not be optimal for all cell types. This may cause biases in the data obtained. The Opera Phenix microscope, which is able to image z-stacks was used for all other imaging assays in this thesis.

3.3.4. ROS

Evidence suggests that dysfunctional mitochondria may produce an increased amount of ROS (Park, Davis and Sue, 2018). In our study, we observed a small, but non-significant, increase in mitochondrial ROS in some of the LRRK2-G2019S manifesting cell lines, while no observable differences were found between the different subgroups in cytosolic ROS.

There is minimal literature exploring ROS levels specifically in LRRK2-G2019S fibroblasts. Yakhine-Diop et al. 2019 found an increase in ROS production and mitochondrial ROS in LRRK2 patient fibroblasts, while Papkovskaia et al. 2012 observed that intracellular ROS generation was decreased in LRRK2-G2019S patient fibroblasts (Papkovskaia *et al.*, 2012; Yakhine-Diop *et al.*, 2019). Su and Qi 2013 found a variable increase in mitochondrial ROS in three LRRK2-G2019S patient fibroblasts compared with one control line (Y.-C. Su and Qi, 2013). In SN4741 cells, overexpression of WT and G2019S LRRK2 led to an increase in intracellular ROS levels in both untreated and hydrogen peroxide treated conditions (Heo *et al.*, 2010). In the study, incubation of SN4741 cells with conditioned medium from cells expressing G2019S followed by hydrogen peroxide treatment had a 10-15% increase in cell death compared with cells that were incubated with conditioned media from WT or empty vector cells, suggesting that LRRK2-G2019S increases oxidative stress induced neurotoxicity (Heo *et al.*, 2010). To this end, it may be useful to explore the effect of hydrogen peroxide treatment on ROS and cell death in the cell lines used for this thesis.

3.3.5. Mitochondrial complexes

Interestingly, the strong trend towards a decrease in complex IV subunit expression in this thesis has also been observed in other studies looking at cells with the LRRK2-G2019S mutation. For example, Su and Qi 2013 also used the same OXPHOS cocktail antibody and found a decreased protein expression in both complex I, and particularly, in complex IV subunits in HeLa cells overexpressing LRRK2-G2019S (Y.-C. Su and Qi, 2013). Although less of a strong trend towards a decrease in complex I subunit was observed in our study, there was a clear decrease in complex I subunit observed in four of the six LRRK2-G2019S manifesting cell lines.

A particularly interesting finding in this thesis was the significant decrease in SCO2 expression in LRRK2-G2019S PD fibroblasts. A more in-depth discussion of SCO2 and the associated literature is provided in Chapter 6.

It must be noted that not all studies have shown a decrease in complex IV activity in LRRK2-G2019S fibroblasts. For example, a recent study by Delcambre et al. 2020 found that while there was a significant decrease in complex I activity in patient fibroblasts, only a small non-significant decrease was observed in complex IV activity (Delcambre *et al.*, 2020). There may be a number of reasons for this discrepancy in findings. For example, the media type used in the Mortiboys et al. 2015 study and the Delcambre study were different, EMEM and DMEM, respectively (Mortiboys *et al.*, 2015; Delcambre *et al.*, 2020). Unpublished data from our group has shown that media type can vary mitochondrial characteristics quite substantially. Another difference was the cohorts used and the differing methodology in measuring mitochondrial complex activity. In this thesis, some of the same cohort and the same media type as the Mortiboys et al. study were used (Mortiboys *et al.*, 2010, 2015). We observed no change in protein expression of the complex I subunit we studied (NDUFB8), but a decrease in complex IV subunit expression. It may be useful in future studies to also look at additional complex I subunits to see whether this is restricted to NDUFB8 or if globally there is no change. It will also be important that the same media type and methodology are used between different studies to aid in their comparability, as it is unclear which of these factors may be responsible for the difference between these two studies. Both of these studies utilise primary patient fibroblasts, it will be interesting to measure respiratory chain activity in reprogrammed neuron-like cells derived from manifesting and non-manifesting LRRK2-G2019S samples; as the reliance of neurons on OXPHOS is greatly increased compared to fibroblasts and may identify exacerbated differences

between groups. However, this will be technically challenging to generate enough material to be able to measure individual respiratory chain complexes.

3.3.6. Mitochondrial morphology

In this thesis, the findings regarding mitochondrial morphology were quite variable. However, this variability in different cell lines is comparable with the current state of the current literature. For example, in our study, there was no difference in OPA1 expression in fibroblasts between the different subgroups in either long or short OPA1 isoforms. This is consistent with data in SH-SY5Y cells overexpressing LRRK2-G2019S, where no difference in OPA1 was observed (Wang *et al.*, 2012). However, in LRRK2-G2019S post-mortem brain tissue, the short isoform of OPA1 was found to be decreased (Stafa *et al.*, 2014). These data demonstrate that OPA1 expression is variable across different LRRK2-G2019S cell types. Similarly DRP1 expression in fibroblasts is variable in the literature, with no significant differences between LRRK2-G2019S manifesting and control fibroblasts in both our study and data from Bonello *et al.* 2019, while Yakhine-Diop *et al.* 2019 found an increase in DRP1 expression in LRRK2-G2019S manifesting fibroblasts (Bonello *et al.*, 2019; Yakhine-Diop *et al.*, 2019). Interestingly in our study, DRP1 expression was decreased in the majority of LRRK2-G2019S non-manifesting cells compared with controls. To the best of our knowledge, this is the first time DRP1 expression has been explored in non-manifesting cells.

It has been suggested that LRRK2 directly interacts with DRP1 to affect mitochondrial morphology (Wang *et al.*, 2012). An increase in mitochondrial fragmentation and DRP1 colocalization has been previously observed in LRRK2-G2019S manifesting fibroblasts compared to controls (Y.-C. Su and Qi, 2013; Yakhine-Diop *et al.*, 2019). However, Mortiboys *et al.* 2010 observed an increase in mitochondrial elongation and interconnectivity

in LRRK2-G2019S patient fibroblasts, and LRRK2-G2019S knock in mice were found to exhibit a bead-on-a-string-like mitochondrial morphology suggestive of abnormalities in mitochondrial fission or fusion (Mortiboys *et al.*, 2010; Yue *et al.*, 2015). In our study, the percentage of short mitochondria was increased in some of the LRRK2-G2019S manifesting and non-manifesting fibroblasts, suggesting an increase in mitochondrial fragmentation. However, there were minimal changes in DRP1 localisation to the mitochondria. This may be in part due to the data analysis method which could not directly measure colocalization of DRP1 and mitochondria, but rather the number of DRP1 spots in the mitochondria. Overall, this data suggests that there may be some changes in mitochondrial morphology, but it is unclear whether this is mediated by an interaction between LRRK2 and DRP1.

DRP1 phosphorylation is involved in the regulation of DRP1 activity, such as DRP1's translocation to the mitochondrial outer membrane which is promoted by phosphorylation at Ser616 (Zhu *et al.* 2004; Xie *et al.* 2020). In this thesis, we looked at total DRP1, rather than phosphorylated DRP1. Interestingly, there evidence shows that the PD associated gene, PINK1 can directly regulate DRP1 by phosphorylation at Ser616, regulating mitochondrial fission (Han *et al.* 2020). LRRK2 has also been shown to indirectly phosphorylate DRP1, as LRRK2 knockdown has shown an increased protein expression of phosphorylated DRP1 but no change in total DRP1. It would be interesting to see whether there are any changes in phosphorylated-DRP1 in our LRRK2-G2019S fibroblast cell lines.

3.3.7. Future studies

As previously mentioned, there is a benefit in studying a cohort of non-manifesting LRRK-2019S patients due to the pre-clinical nature of this cohort. At the time of thesis submission, the follow-up information regarding whether the LRRK2-2019S non-manifesting cohort had

developed PD symptoms was not available. The non-manifesting cohort were heterogeneous in both mitochondrial function and morphology. For example, one non-manifesting line showed a particularly severe ATP deficit when exposed to galactose media. In addition, a subset of the non-manifesting lines showed an increase in SCO2 expression and a decrease in DRP1 expression. This may suggest a compensatory effect in some of the non-manifesting cohort, potentially suggesting why PD symptoms had not manifested at the time of skin biopsy collection. It would be interesting in future studies to determine whether age of LRRK2-G2019S PD onset is correlated with mitochondrial dysfunction.

There were no clear changes observed with UDCA treatment in our cell lines. One of the proposed mechanisms of action is that the AKT pathway mediates the action of UDCA (Hanafi *et al.*, 2016). It would be useful to explore the AKT pathway further in LRRK2-G2019S patient cells. UCA treatment led to a small decrease in mitochondrial ROS in the different cell lines. However, there was no significant difference in mitochondrial ROS in either glucose or galactose media in untreated cells between the different subgroups. Therefore, these cells may need to be stressed in order to observe any effect of treatment.

Both an advantage and a limitation of this thesis was that patient samples were not always compared to the same control sample in each repeat of assays. The reason for this was due to availability of samples, and the differing growth rates between different cell lines. This increases the reliability of the study to certain extent. For example, if SCO2 was found to be decreased even when compared against different controls, this suggests it to be a more robust finding as it is not dependent on the control that it was compared to. However, as control samples will not all show the same phenotype, it does add to the heterogeneity of the findings and may mean that more subtle differences in the mitochondrial phenotype were not observed. For future studies it may be useful to use an immortalised cell line, such as WS1, for each experiment, to help normalise across different experiments.

The complex IV deficit in LRRK-G2019S PD that has been demonstrated both in this thesis and in the literature is particularly interesting regarding the development of personalised medicine. Although PD describes one disorder, there is a growing trend in both clinical and academic medicine as describing PD as an 'umbrella' disorder, containing many different subtypes. It is not typical in the general population to screen for LRRK2 mutations unless there is a clear genetic predisposition within the family. As the clinical symptoms are similar between idiopathic and LRRK2 PS, this means that many patients with a LRRK2 mutation may be recruited to clinical trials alongside patients with idiopathic PD. This may not be conducive to testing new treatments targeting the mechanisms underlying idiopathic PD may not be as effective for LRRK2 mutation-induced PD, and vice-versa. Therefore, it will be important in future large-scale clinical trials to screen for LRRK2 mutations.

Chapter 4 **Assessing mitochondrial function in LRRK2-G2019S induced neural progenitor cell derived dopaminergic neuron-like cells**

4.1. Background

In the previous chapter, using fibroblasts allowed us to gain insight into the mitochondrial phenotype present in LRRK2-G2019S manifesting cells. However, while fibroblasts are a well-utilised model to investigate mitochondrial deficiencies, they are not the cells which degenerate in Parkinson's disease (PD). Therefore, the same mitochondrial phenotype found in the fibroblasts may not be present in the dopaminergic neurons, thereby reducing their utility in studying PD pathogenesis. Newer models, which better represent these dopaminergic neurons, could allow a greater understanding of how the mitochondria are affected in PD. Induced pluripotent stem cells (iPSCs), first developed in 2006 by Takahashi and Yamanaka, are able to be differentiated into any cell type, including dopaminergic neurons (Takahashi and Yamanaka, 2006). Since then, they have been used substantially in studying human disease. The model which is used in this study are induced neuronal progenitor cells (iNPCs). These are similar to iPSCs but instead of being reprogrammed to a pluripotent stem cell, the cells are reprogrammed to neuronal progenitor cells which are further down the ectoderm lineage. These neuronal progenitor cells can be differentiated into any cell type of the brain, apart from microglia as these derive from the mesenchymal lineage.

iNPCs have several benefits over iPSCs. For example, the cell population is not taken from one clone but from a population of cells, which reduces potential bias if the clone that is used is not representative of most of the cell population. In addition, the differentiation process into different cell types from iNPCs can be quicker and more efficient. Our group

has previously found that the differentiation process into dopaminergic neuron-like cells from iNPCs has a high efficiency in producing tyrosine hydroxylase (TH) positive neurons (89.9% TH positive) compared to previously published studies using iPSC-derived DA neurons (Schwartzentruber *et al.*, 2020). There is also evidence to suggest that cells differentiated from iNPCs also have a more aged phenotype than those from iPSCs, which is very beneficial when investigating an age-related condition such as PD (Gatto *et al.*, 2020). Our group has shown that iNPC-derived DA neuron-like cells switch from glycolysis to OXPHOS as they undergo differentiation, which is indicative of an adult neuron (Hall *et al.*, 2012; Zheng *et al.*, 2016; Schwartzentruber *et al.*, 2020). This has not been fully investigated in iPSC-derived DA neuron models. There is literature which suggests a change in metabolism needed by cells as they differentiate from iPSC to neural crest cells, but the metabolism in the final stage of differentiation has not yet been published (Lees, Gardner and Harvey, 2018).

Comparing the mitochondrial phenotype between fibroblasts and iNPC-derived DA neuron-like cells can provide some very useful information. For instance, drug screening of induced-dopaminergic neuron models is more time-consuming, technically challenging and costly than using patient fibroblasts. Therefore, if there are mitochondrial abnormalities that are present in both fibroblasts and our neuron-like cell model, this will tell us which parameters in the fibroblasts may be useful in screening for different drugs that improve mitochondrial function. Conversely, if there are changes in the neurons and not the fibroblasts, these may be particularly crucial mitochondrial abnormalities that may lead to the specific degeneration of DA neurons in PD.

In this chapter, we show pilot data from 1 LRRK2-G2019S PD patient and 1 control iNPC-derived DA neuron-like cell line in several mitochondrial parameters which have been previously explored in fibroblasts in Chapter 3. In addition to mitochondrial parameters, we

have also begun to investigate lysosomal changes due to LRRK2's suggested effect on lysosomes and mitophagy. Data has been collected from these neuron-like cells at several points across the differentiation process to assess at which point any mitochondrial and lysosomal deficiencies may develop.

4.1.1. Aims and objectives

The aims of this chapter were to characterise both mitochondrial and lysosomal differences between LRRK2-G2019S manifesting and control iNPC-derived DA neuron-like cells throughout the differentiation process by:

- Measuring ATP levels
- Measuring mitochondrial membrane potential (MMP)
- Evaluating changes in mitochondrial and lysosomal numbers and morphology
- Measuring mitochondrial and cytosolic reactive oxygen species levels

4.2. Results

4.2.1. iNPC-derived DA neuron-like cell characterisation

LRRK2-G2019S manifesting and control neuron-like cells were imaged throughout the course of the third stage of differentiation in order to assess changes in cell morphology.

Figure 4.1 presents brightfield images from the same field of view at different days of the differentiation process. A clear change in cell morphology was observed in both LRRK2-G2019S manifesting and control neuron-like cells. Towards the end of the differentiation cells began to elongate and the neuronal bodies began to cluster. Although iNPC-derived neuron-like cells show a difference in morphology compared with the more typical model of iPSC-derived neuron, the clustering of neuronal bodies is clear in both DA neuron-like

models. Interestingly, there was a visual difference between the LRRK2-G2019S manifesting and control cells. The LRRK2-G2019S manifesting DA neuron-like cells had thicker projections compared with the control. From our groups previous experience differentiating the DA neuron-like cell model, different cell lines can have different morphologies such as projections and cell body size. It would be interesting to determine whether this difference in morphology is present in cells derived from additional LRRK2-G2019S manifesting PD patients.

We further characterised the neuron-like cells by staining the cells with TuJ1, a neuronal marker, and tyrosine hydroxylase (TH), a marker of dopaminergic neurons. As can be seen in **Figure 4.2**, at the end of differentiation neuron-like cells are both TuJ1 and TH positive, suggesting that they are a suitable dopaminergic neuron-like model. Due to time constraints and low yield of cells, we focussed on assessing mitochondrial and lysosomal assessment for the rest of this thesis, rather than additional characterisation. The same differentiation protocol used has been to generate both Parkin and sporadic PD iNPC-derived DA neuron-like cells, which were characterised by Schwartzenruber et al. 2020 and Carling et al. 2020. The Schwartzenruber et al. 2020 study included the same control line used for this thesis, and showed increased mRNA expression of TH at day 27 differentiation compared with iNPCs, as well as high percentages of positive microtubule-associated protein (MAP)2, dopamine transporter (DAT), NeuN and Neurosensor 521 staining.

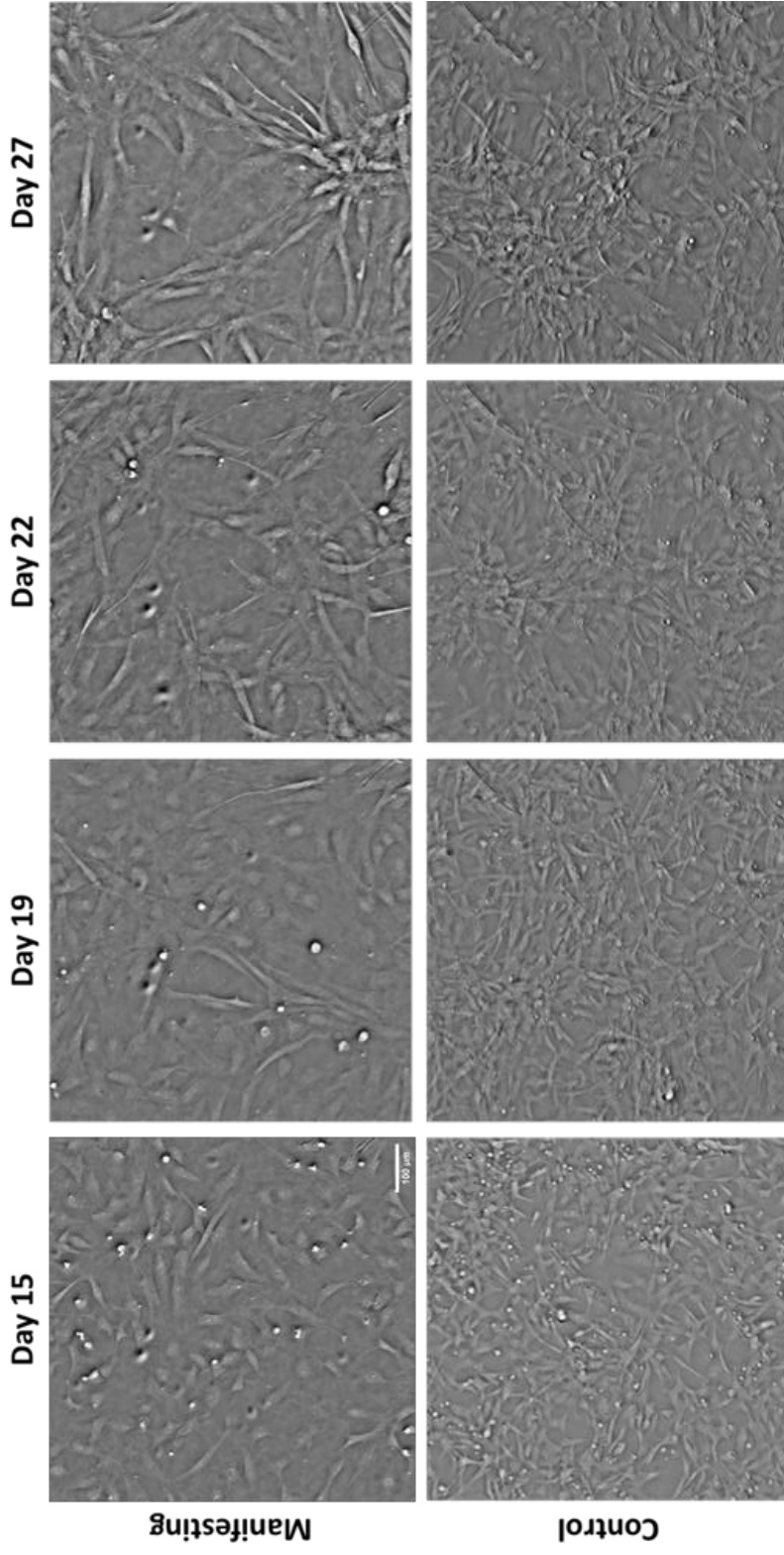


Figure 4.1. Brightfield imaging of LRRK2-G2019S manifesting and control iNPC-derived DA neurons during the third stage of differentiation.

Days represent the total number of days cells were differentiated for.

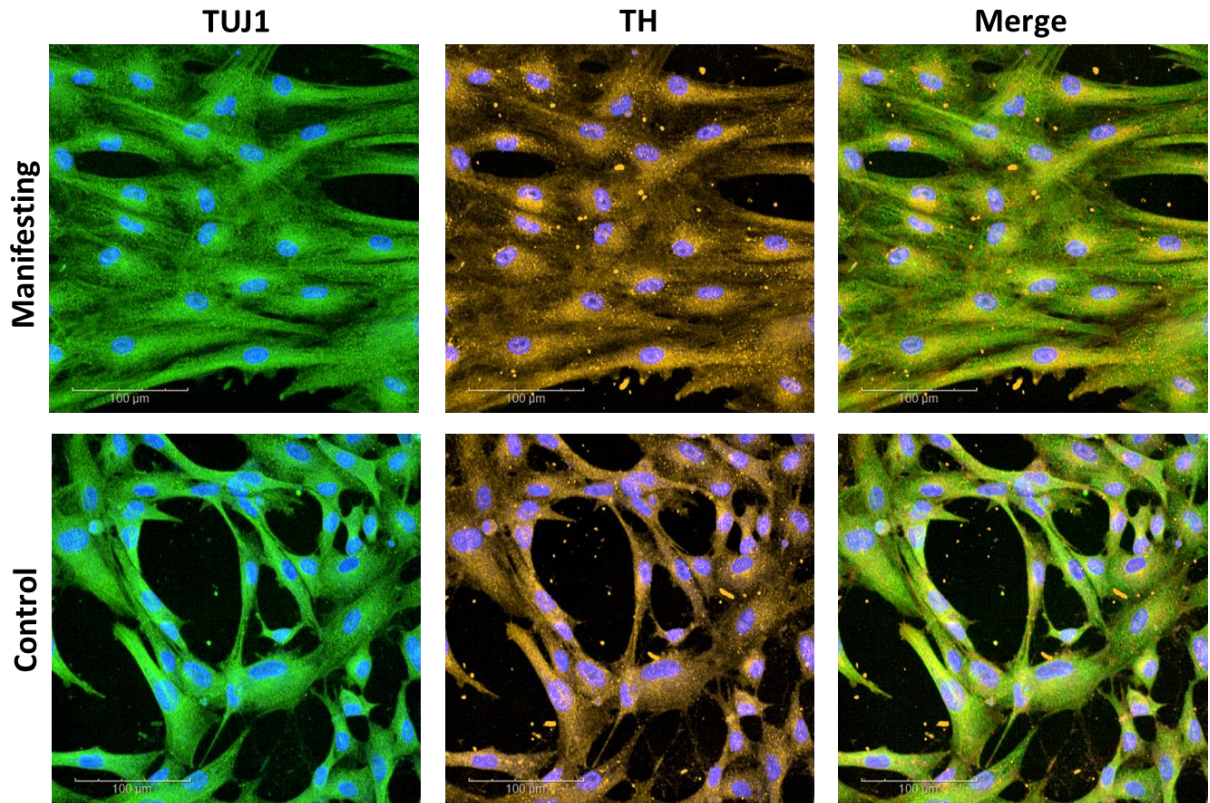


Figure 4.2. Tuj1 and TH staining of LRRK2-G2019S manifesting and control iNPC-derived DA neuron-like cells at day 27 of neuronal differentiation.

Representative images of neuronal marker Tuj1 (green) and dopaminergic marker tyrosine hydroxylase (TH; orange). Hoechst was used to label nuclei (blue). Images were gamma adjusted to improve the clarity of neuronal projections. Scale bar, 100 μm

4.2.2. ATP levels throughout differentiation

ATP levels were measured during the third stage of differentiation for both LRRK2-G2019S and control neuron-like cells (**Figure 4.3**). Contrary to what was originally hypothesised, the LRRK2-G2019S patient neuron-like cells showed an increase compared to control cells. Although, both patient and control cells had very similar ATP levels at day 12 (last day of FGF/SAG treatment), when cells were exposed to the third stage differentiation factors,

there was a sharp increase in the ATP levels compared with the controls, reaching a mean of 25% increase compared with control neuron-like cells. Interestingly, this difference between the patient and control started to decrease throughout the third stage of differentiation. Therefore, instead of stopping cell differentiation at day 27, we extended the differentiation for 7 additional days. By day 34, there was a less marked difference in ATP levels between the two groups, with a mean of a 7% increase in the manifesting line. Unfortunately, the cells did not survive in culture after this time point to test whether this trend continued. These results suggest that either the ATP levels of the controls was increasing throughout the third stage of differentiation, that the patient ATP levels were decreasing, or a mixture of both. However, as the ATP levels were relative arbitrary values, rather than exact measurements of ATP levels, then direct comparisons between the different timepoints is not possible to ascertain, and further investigation is required to test this.

We hypothesised that similar to the fibroblasts in Chapter 3, any ATP deficits would perhaps be more pronounced in galactose-containing media. Schwartzenruber et al. 2020 has shown that the control line used in this thesis has a switch to from glycolysis to OXPHOS dependency at the end of differentiation. However, it was unclear whether directing the neuron-like cells towards utilising OXPHOS to generate ATP would unmask any deficits in the LRRK2-G2019S manifesting line. Therefore, at the end of the neuronal differentiation, we cultured cells in galactose-containing media for 24 h. We also cultured cells with neither galactose nor glucose in the media (**Figure 4.4**). There was a large amount of variation in ATP levels between the different neuronal differentiations when the cells were cultured in galactose-containing media. Therefore, no significant differences were observed between the patient and control neuron-like cells. In addition, when cells were cultured in media containing neither glucose nor galactose, there was a reduction in ATP levels seen

compared with the other media types. This is not as pronounced as one might expect, potentially due to the large amount of cell death after treatment in this media type, which may have potentially biased the values. There was, however, no difference between manifesting or control neuron-like cells in this media type.

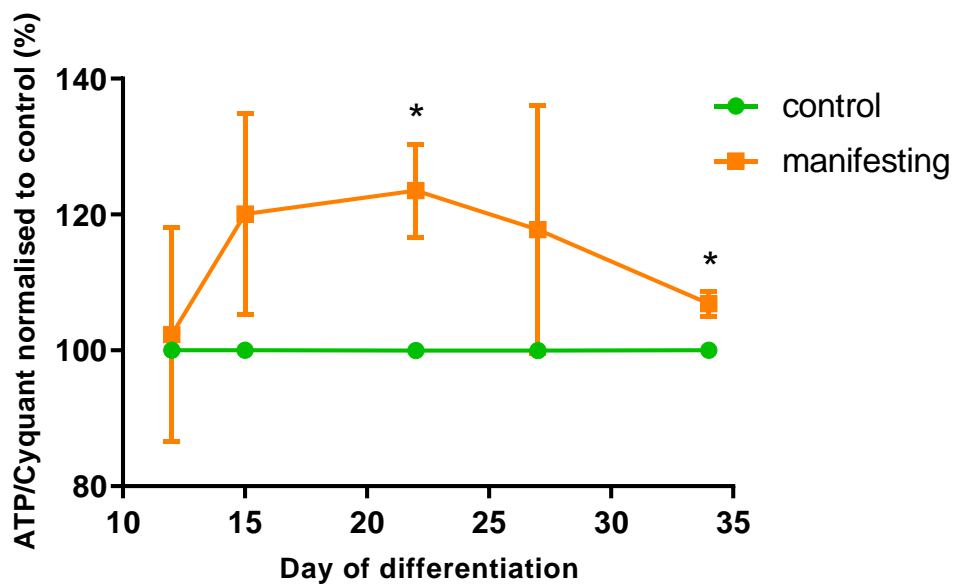


Figure 4.3. ATP levels of LRRK2-G2019S manifesting and control iNPC-derived DA neuron-like cells throughout differentiation.

Percentage of total cellular ATP/Cyquant at day 12, day 15, day 22, day 27 and day 34 of differentiation normalised to control iNPC-derived DA neuron-like cells. * $p < 0.05$ unpaired t-test with Welch's correction. $n = 3$ independent differentiations, with 3 technical repeats. Data represent mean \pm SD.

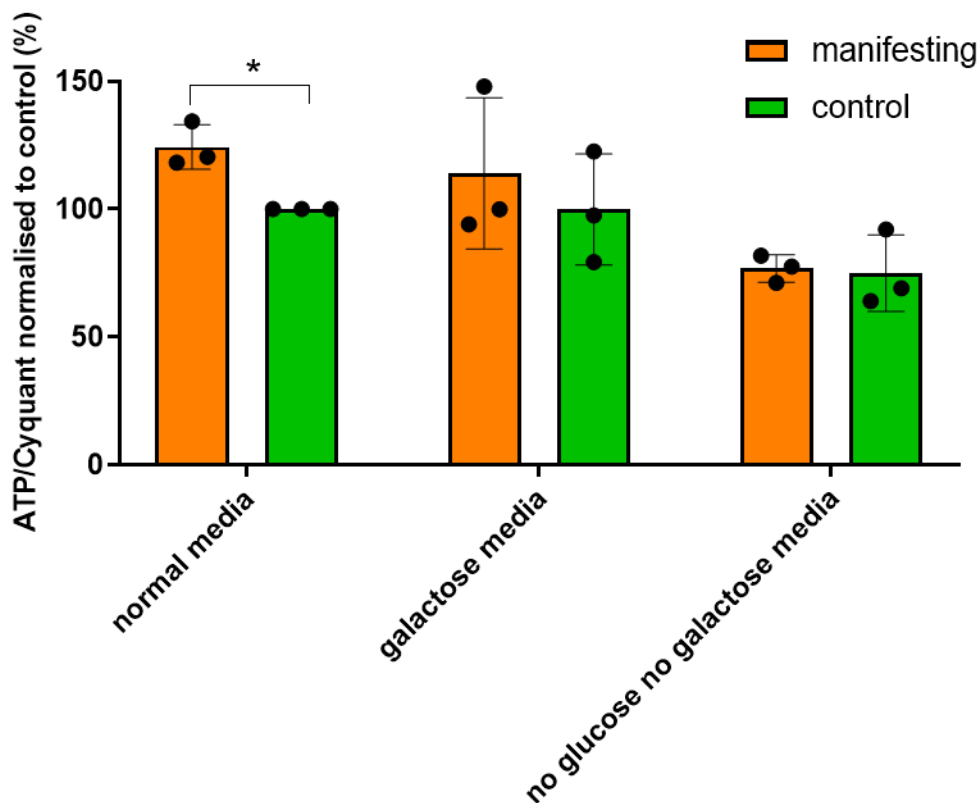


Figure 4.4. ATP levels of LRRK2-G2019S manifesting and control iNPC-derived DA neuron-like cells in different media types.

Percentage of total cellular ATP/Cyquant of cells cultured in normal neuronal media, galactose-containing media, and media without glucose or galactose for 24 h normalised to control iNPC-derived cells cultured in normal neuronal media. $n = 3$ independent differentiations, with 3 technical repeats. Data represent mean \pm SD. Each dot represents the mean of the experimental repeats per differentiation. $*p < 0.05$ one sample t-test with a hypothetical mean of 100.

4.2.3. Mitochondrial membrane potential and mitochondrial number

MMP was assessed in LRRK2-G2019S and control iNPC-derived DA neuron-like cells throughout the differentiation using the cationic dye TMRM (**Figure 4.5**). CCCP was tested as a positive control of reduced TMRM staining. A clear reduction in TMRM intensity when cells were treated with CCCP was demonstrated (data not shown). Mitochondria were segmented at all time points and the MMP measured, excluding day 12 where the cytosolic TMRM intensity was measured due to the size of the cells meaning that accurate mitochondrial segmentation was not possible. No difference was observed between the genotypes at day 12 of differentiation, but by day 15 there was a trend towards a decrease ($68 \pm 15\%$ of control values) and a significant reduction in MMP (mean 28%) was observed in the LRRK2-G2019S iNPC-derived DA neuron-like cells by day 27 (**Figure 4.6 a**).

TMRM staining was also used to quantify the number of mitochondria. Similar to our findings in the fibroblasts, there was no clear difference in the number of the mitochondria per cell area between the LRRK2-G2019S manifesting and control iNPC-derived DA neuron-like cells (**Figure 4.6 b**). However, unlike the fibroblasts, there was a small trend towards a decrease in the percentage of perinuclear mitochondria. This finding was more variable throughout the differentiation (**Figure 4.6 c**).

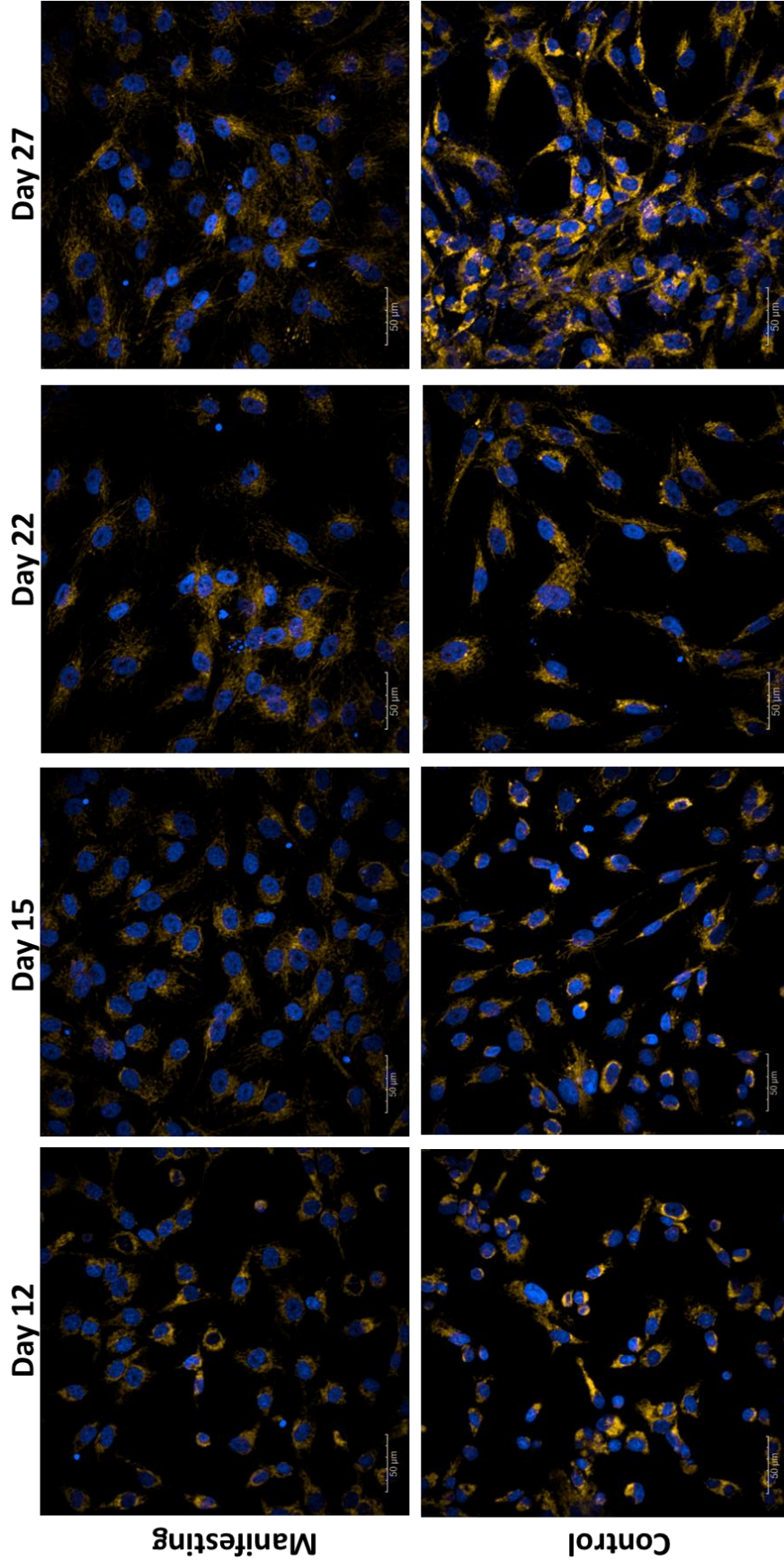


Figure 4.5. TMRM staining of LRRK2-G2019S manifesting and control INPC-derived DA neuron-like cells throughout neuronal differentiation.

Representative images of TMRM staining (orange) LRRK2-G2019S manifesting and control INPC-derived DA neuron-like cells throughout differentiation. Hoechst was used to label nuclei (blue).

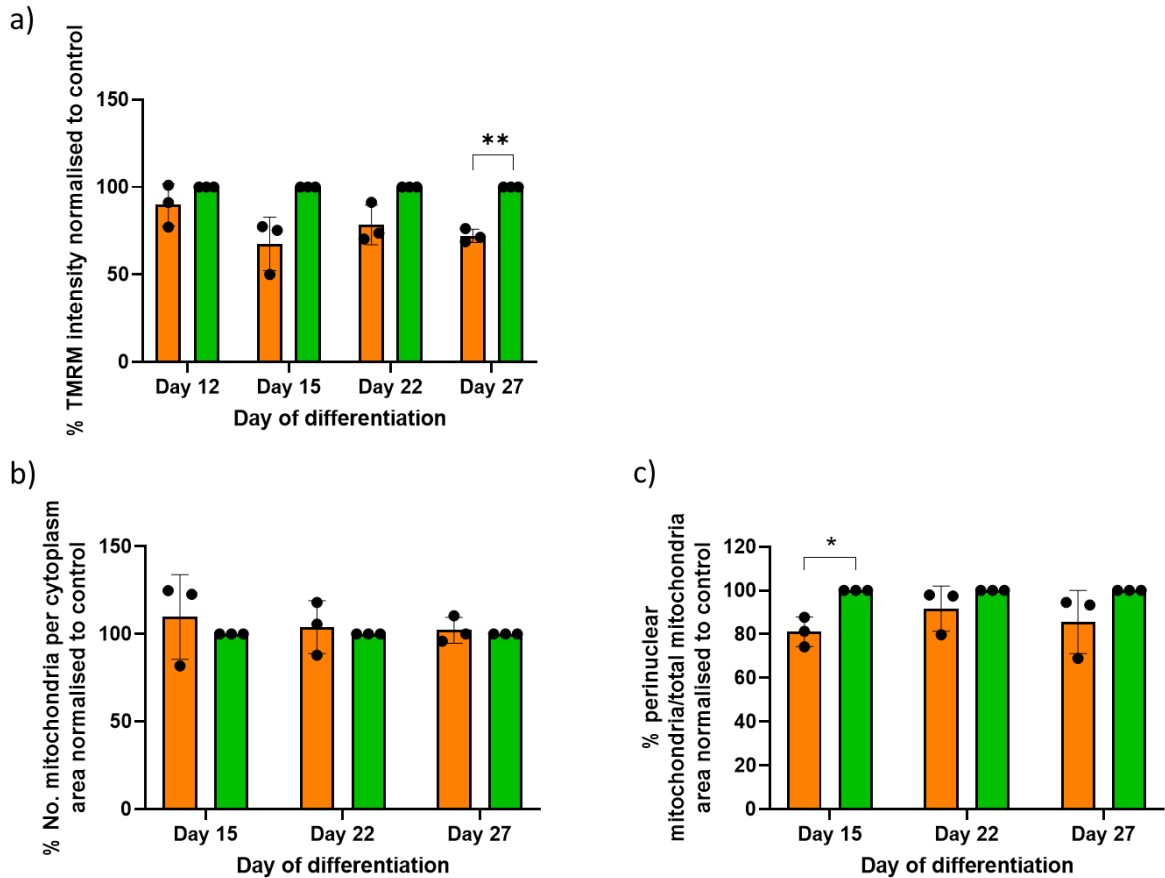


Figure 4.6. Quantification of mitochondrial characteristics of LRRK2-G2019S manifesting and control iNPC-derived DA neuron-like cells throughout neuronal differentiation.

a) Percentage TMRM intensity of mitochondria normalised to control iNPC-derived DA neuron-like cells. For day 12 of differentiation, cells were too small to segment mitochondria, therefore, the data represents the TMRM intensity of the cytoplasm region at this timepoint. b) Number of mitochondria per cell area normalised to control iNPC-derived DA neuron-like cells c) Percentage of perinuclear mitochondria normalised to control iNPC-derived DA neuron-like cells. n= 3 independent differentiations, with 2 technical repeats. Data represent mean \pm SD. Each dot represents the mean of the experimental repeats per differentiation. * $p < 0.05$; ** $p < 0.01$ one sample t-test with a hypothetical mean of 100.

4.2.4. Lysosomal phenotype and mitophagy

There is evidence that LRRK2 has a role in autophagy and lysosome activity in neurons (Madureira, Connor-Robson and Wade-Martins, 2020), therefore we explored whether a lysosomal phenotype was present in LRRK2-G2019S manifesting iNPC-derived DA neuron-like cells using LysoTracker as a marker (**Figures 4.7 and 4.8**). We observed that the number of lysosomes between different differentiations was highly variable (**Fig. 4.8 a**). The mean area of individual lysosomes showed a trend towards a decrease in LRRK2-G2019S manifesting iNPC-derived DA neuron-like cells. at day 15 of differentiation compared with the control ($82 \pm 10\%$ of control lysosome area). This reduction was less pronounced by day 27 of differentiation ($96 \pm 1\%$; **Figure 4.8 b**).

Evidence suggests that there is dysfunctional mitophagy in LRRK2-G2019S iPSC-derived neurons. Therefore, we wanted to assess whether this was the case in our DA neuron-like cell model. In order to determine basal mitophagy in our cells, we segmented both the mitochondria from the TMRM staining and the lysosomes from the LysoTracker staining using Harmony analysis software. Next, we segmented the lysosomes found within the mitochondria. We then calculated the number of lysosomes in the mitochondria / the total number of lysosomes and normalised this to the control cells (**Figure 4.8 c**). Although our data was not significant, we noticed an interesting trend in basal mitophagy throughout neuronal differentiation. At day 15 basal mitophagy was increased in LRRK2-G2019S iNPC-derived DA neuron-like cells compared with the control ($113 \pm 8\%$), but by day 27 basal mitophagy was decreased in LRRK2-G2019S iNPC-derived DA neuron-like cells compared with the control ($95 \pm 5\%$). According to the raw data for these experiments, this is more due a decrease in basal mitophagy over the differentiation in the manifesting cells, rather than a substantial change in mitophagy in the control cells.

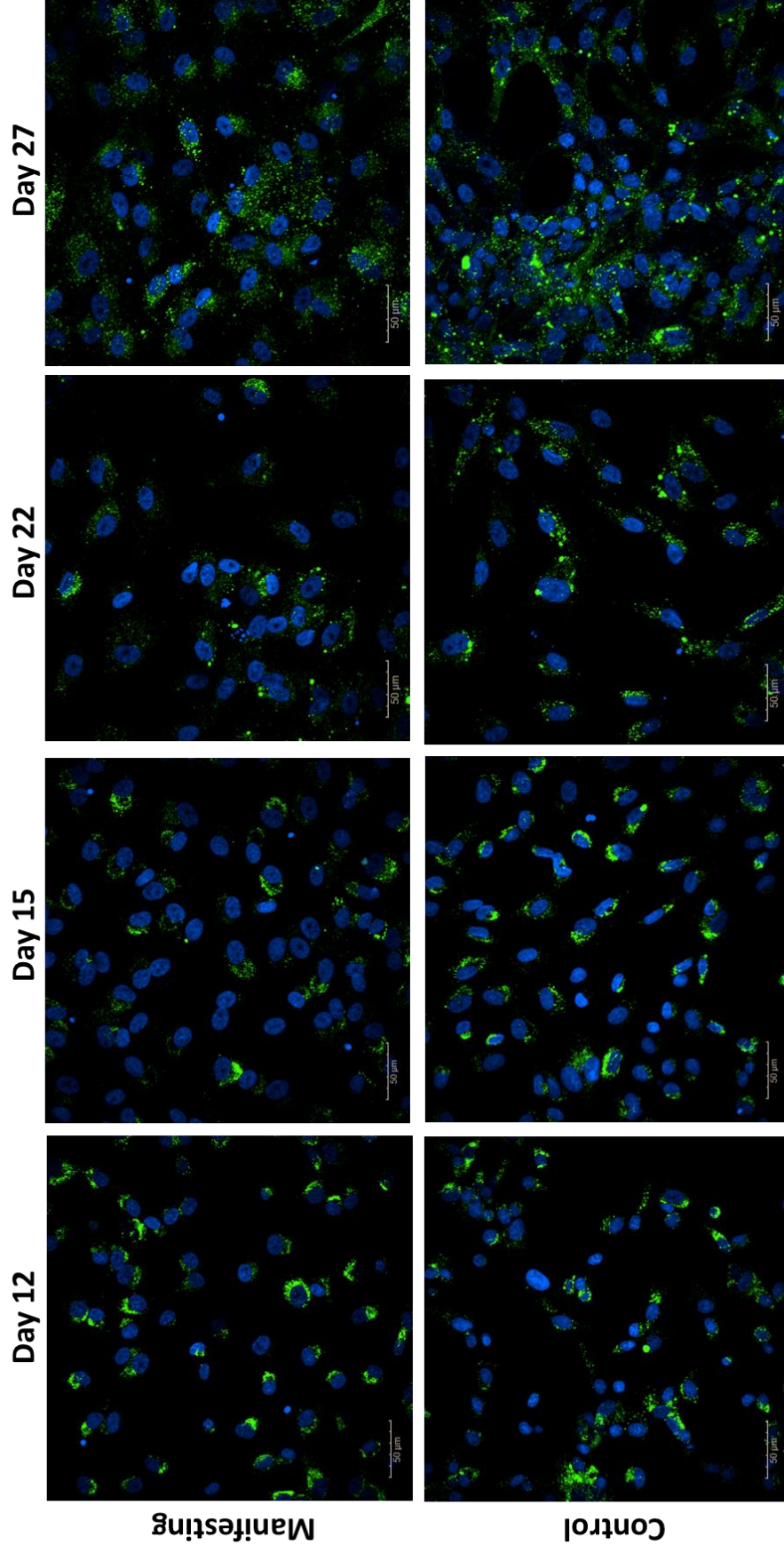


Figure 4.7. LysoTracker staining of LRRK2-G2019S manifesting and control iNPC-derived DA neuron-like cells throughout neuronal differentiation.

Representative images of LysoTracker staining (green) LRRK2-G2019S manifesting and control iNPC-derived DA neuron-like cells throughout differentiation. Hoechst was used to label nuclei (blue).

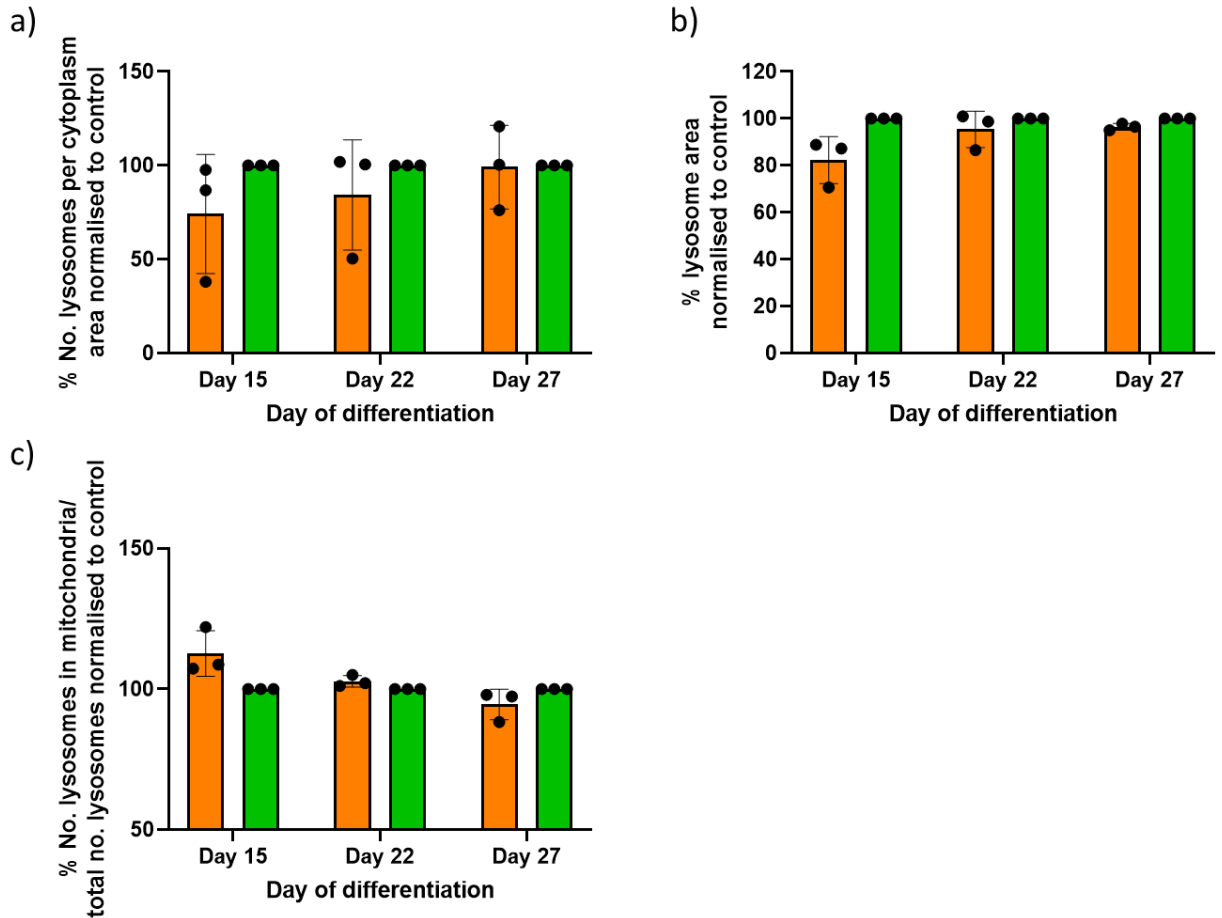


Figure 4.8. Quantification of lysosome characteristics of LRRK2-G2019S manifesting and control iNPC-derived DA neuron-like cells throughout neuronal differentiation.

a) Number of lysosomes per cell area normalised to control iNPC-derived DA neuron-like cells b) Mean area per lysosome normalised to control iNPC-derived DA neuron-like cells c) Percentage of lysosomes in mitochondria normalised to control iNPC-derived DA neuron-like cells n= 3 independent differentiations, with 2 technical repeats. Data represent mean \pm SD. Each dot represents the mean of the experimental repeats per differentiation.

4.2.5. Mitochondrial and cytosolic reactive oxygen species

We assessed mitochondrial ROS throughout the differentiation using the NpFR2 probe (Figures 4.9 and 4.10) Mitochondria were segmented at all time points and the NpFR2 probe measured, excluding day 12 where the cytosolic NpFR2 intensity was measured due

to the size of the cells meaning that accurate mitochondrial segmentation was not possible. We found a decrease in mitochondrial ROS throughout the differentiation, with a significant decrease being observed at day 15, 22 and 27.

We decided to validate this finding using the FRR2 mitochondrial ROS probe at day 27 of differentiation (**Figure 4.11**). We found that for two of the differentiations there was a marked decrease in FRR2 intensity compared with control. However, for one differentiation there was a slight increase compared. Further repeats will be necessary to draw conclusions from this data.

We observed no significant difference in cytosolic ROS between manifesting and control cells, suggesting that only mitochondrial ROS is affected in LRRK2-G2019S iNPC-derived DA neuron-like cells (**Figure 4.12**).

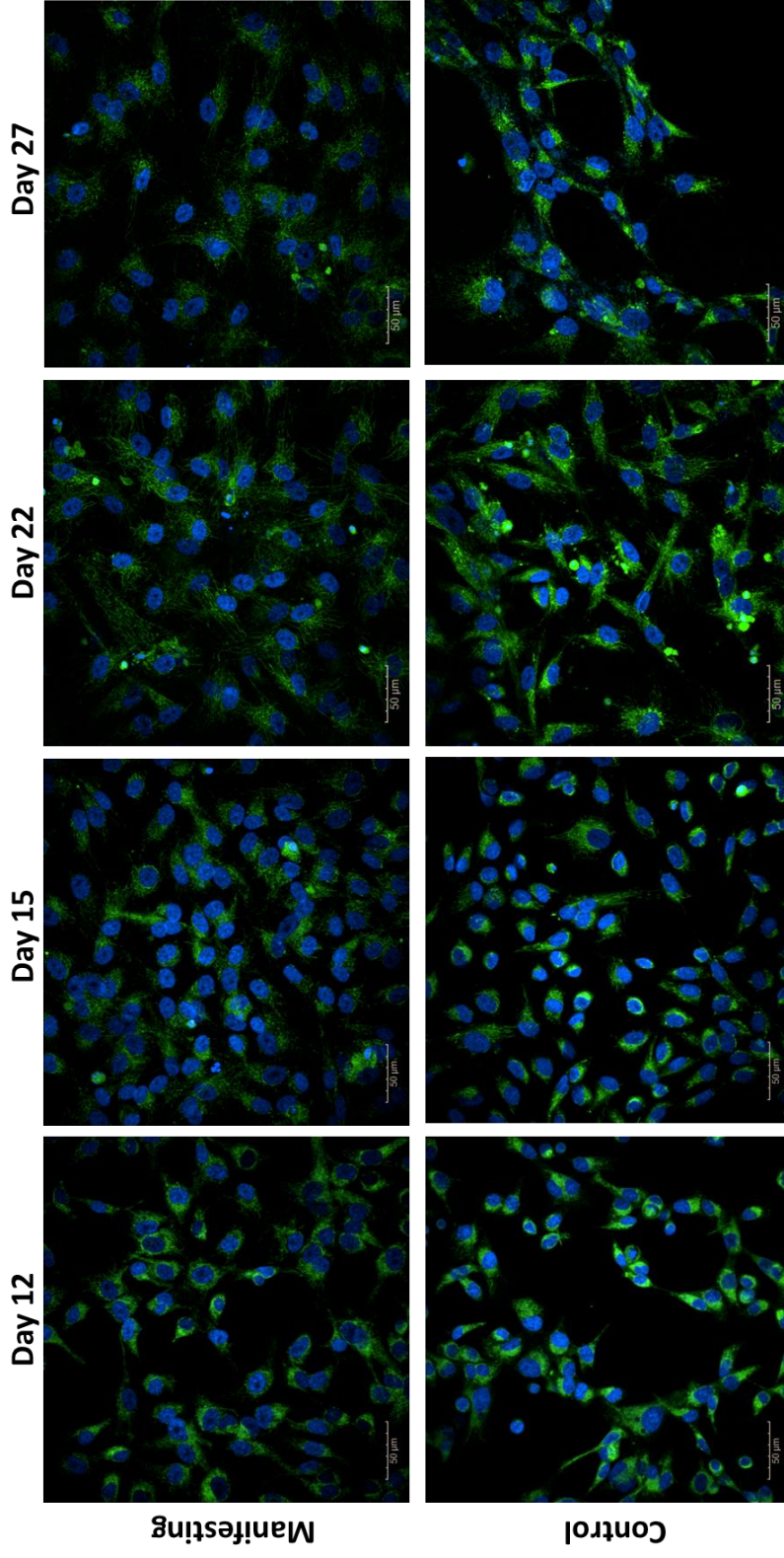


Figure 4.9. Mitochondrial reactive oxygen species probe NpFR2 staining of LRRK2-G2019S manifesting and control iNPC-derived DA neuron-like cells throughout neuronal differentiation.

Representative images of mitochondrial ROS probe NpFR2 staining (green) LRRK2-G2019S manifesting and control iNPC-derived DA neuron-like cells throughout differentiation. Hoechst was used to label nuclei (blue).

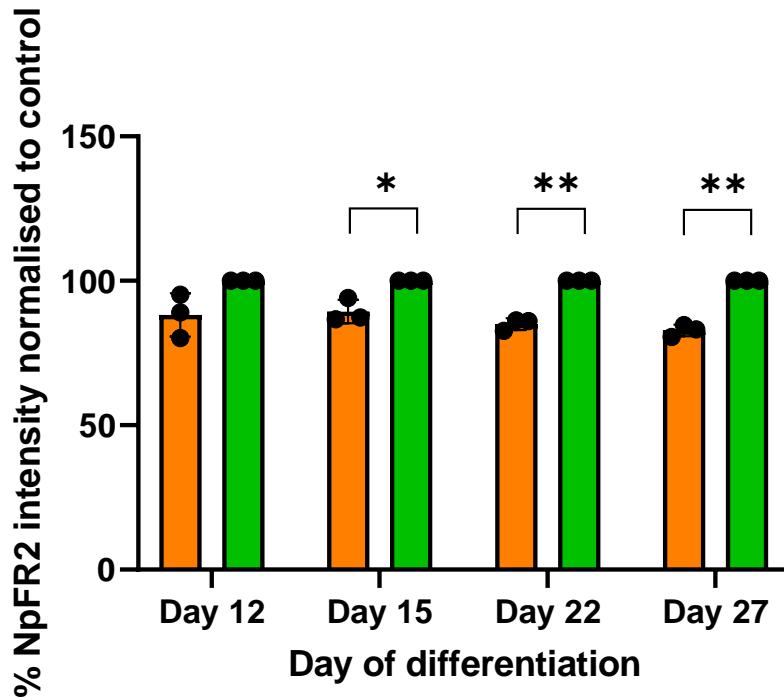


Figure 4.10. Quantification of mitochondrial reactive oxygen species probe NpFR2 staining of LRRK2-G2019S manifesting and control iNPC-derived DA neuron-like cells throughout neuronal differentiation.

n= 3 independent differentiations, with 3 technical repeats. Data represent mean \pm SD. Each dot represents the mean of the experimental repeats per differentiation. *p<0.05; **p<0.01 one sample t-test with a hypothetical mean of 100.

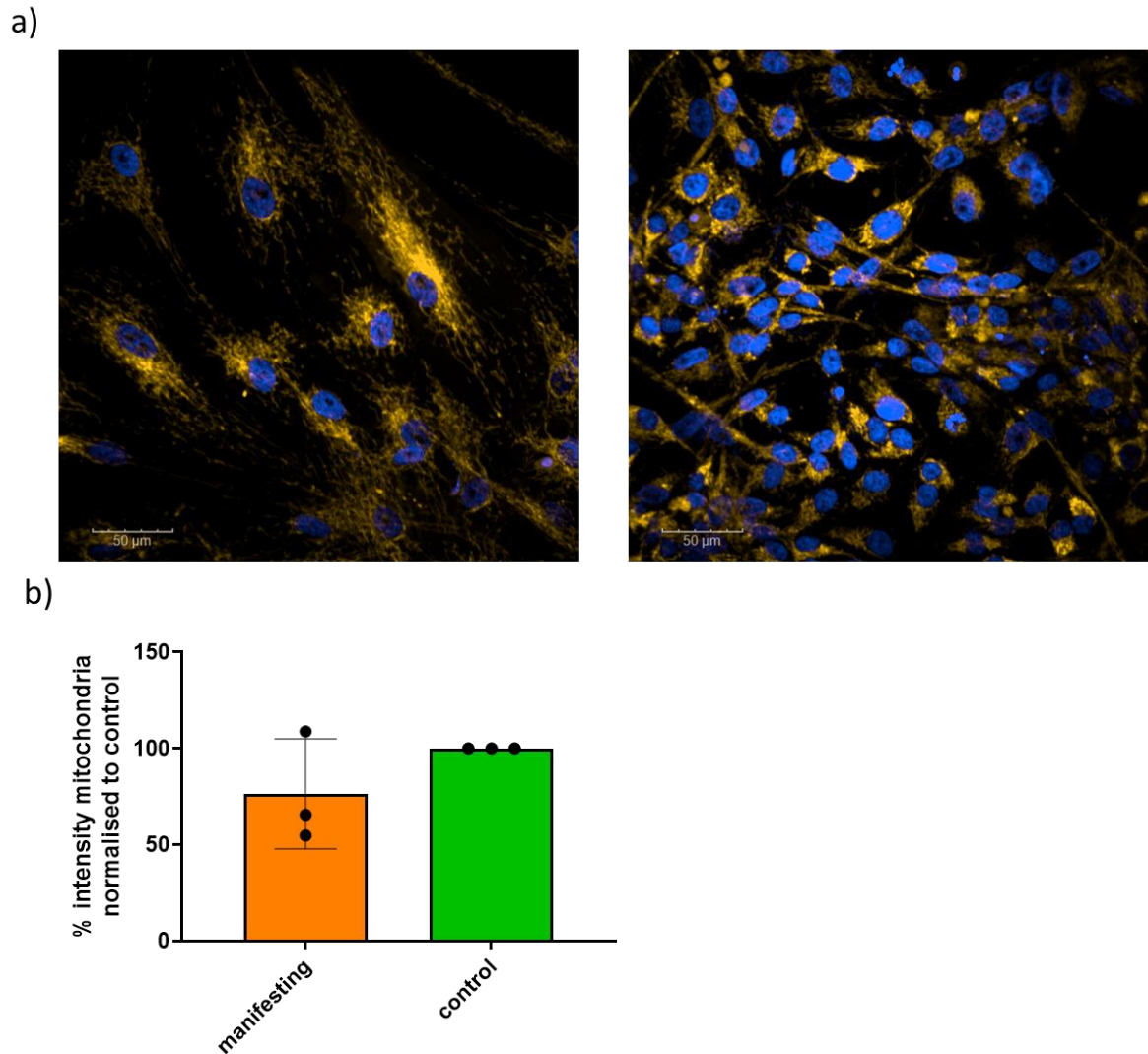
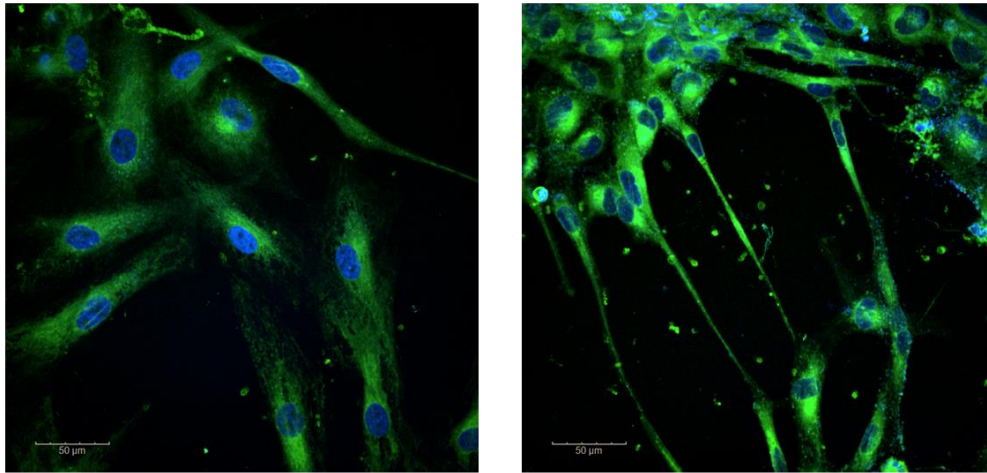


Figure 4.11. Mitochondrial reactive oxygen species probe FRR2 staining of LRRK2-G2019S manifesting and control iNPC-derived DA neuron-like cells at day 27 of neuronal differentiation.

a) Representative images of mitochondrial ROS probe FRR2 (orange). Hoechst was used to label nuclei (blue). Left: manifesting, Right: control. Scale bar, 50 μ M. b) Quantification of FRR2 intensity normalised to control iNPC-derived DA neuron-like cells. $n=3$ independent differentiations, with 3 technical repeats. Data represent mean \pm SD. Each dot represents the mean of the experimental repeats per differentiation.

a)



b)

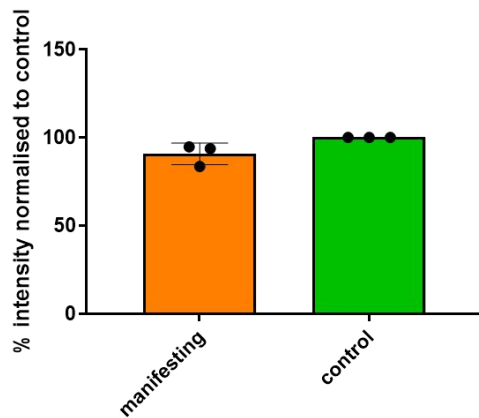


Figure 4.12. Cytosolic reactive oxygen species probe NpFR1 staining of LRRK2-G2019S manifesting and control iNPC-derived DA neuron-like cells at day 27 of neuronal differentiation.

a) Representative images of cytosolic ROS probe NpFR1 (green). Hoechst was used to label nuclei (blue). Left: manifesting, Right: control. Scale bar, 50 μm . b) Quantification of NpFR1 intensity normalised to control iNPC-derived DA neuron-like cells. $n=3$ independent differentiations, with 3 technical repeats. Data represent mean \pm SD. Each dot represents the mean of the experimental repeats per differentiation.

4.3. Discussion

There is a small amount of literature looking at mitochondrial dysfunction in LRRK2-G2019S iPSC-derived DA neuron models, reviewed extensively by (Weykopf *et al.*, 2019). However, to the best of our knowledge, this is the first study to use iNPC-derived DA neuron-like cells to model LRRK2-G2019S PD. As mentioned in the introduction to this chapter, iNPC-derived DA neuron-like cells have several advantages over iPSC-derived models. One of the main advantages is that the cell population is not taken from one clone but from a population of cells, thus being more physiologically relevant. However, one of the major disadvantages this presents is the heterogeneity between the differentiations. This could clearly be seen in some of the parameters assessed in this chapter. In addition, some of the changes observed were small, thus would require additional repeats in order to reach statistical significance.

In our study, we found that ATP levels varied across the differentiation, with LRRK2-G2019S manifesting iNPC-derived DA neuron-like cells demonstrating increased ATP levels compared with the control line. This is contrary to what has been observed in LRRK2-G2019S iPSC-derived DA neurons, where a decrease in ATP levels have been demonstrated (Y.-C. Su and Qi, 2013; Schwab *et al.*, 2017). However, this is not a new phenomenon as increased ATP levels have previously been observed in PD patient cells (Annesley *et al.*, 2016). We hypothesise that the cells could be in an overactive state and may be overcompensating for other dysfunctions. The difference between the LRRK2-G2019S and control iNPC-derived neuron-like cells then begins to decrease as the LRRK2-G2019S neuron-like cells are unable to sustain this increased production of ATP. Another suggestion is that the control line becomes more OXPHOS dependent throughout the differentiation, as observed by Schwartzentruber *et al.* 2020, whilst this may not occur in the LRRK2-G2019S cells. This area will need to be explored further in future studies.

Another finding of this chapter was that in LRRK2-G2019S manifesting iNPC-derived DA neuron-like cells, MMP decreased throughout the differentiation, with a significant decrease compared with the control at day 27. This supports other findings in the literature that show a decrease in MMP in LRRK2-G2019S iPSC-derived neurons (Y.-C. Su and Qi, 2013). This also supports other findings from sporadic and Parkin mutant iNPC-derived DA neuron-like cells (Carling *et al.*, 2020; Schwartzenuber *et al.*, 2020). Interestingly, MMP in fibroblasts from the same patient as the LRRK2-G2019S iNPC-derived DA neuron-like cells were assessed in Chapter 3. In these fibroblasts an increase in MMP was observed, thus showing cell type specific differences within the same patient. Cell type specific differences such as these have been observed in other studies. For example, Cooper *et al.* 2012 found that when LRRK2-G2019S iPSC-derived neural cells were treated with valinomycin they released more lactate dehydrogenase than healthy controls (Cooper *et al.*, 2012). However, LRRK2-G2019S fibroblasts undergoing the same treatment showed no significant difference in lactate dehydrogenase release. Findings such as these are important to note as they may provide us clues to what leads to a selective neuronal vulnerability in LRRK2 PD.

There is evidence to suggest that LRRK2-G2019S affects lysosomes in neurons. For example, in neurons cultured from LRRK2-G2019S knock in mice, a decreased average lysosomal area and increase number of lysosomes per cell were observed (Schapansky *et al.*, 2018). In our study, we found that the number of lysosomes per cell area was very variable. This is not surprising as lysosomes are very dynamic organelle. The mean area per lysosomes also had a trend towards a decrease in LRRK2-G2019S iNPC-derived DA neuron-like cells. However, this trend was not seen later in the differentiation.

Recently, there has been growing interest in mitophagy in LRRK2-G2019S PD (Bonello *et al.*, 2019; Korecka *et al.*, 2019; Singh *et al.*, 2020; Wauters *et al.*, 2020). Studies have

suggested that LRRK2 may be involved in PINK1 and Parkin-mediated mitophagy via either Rab10 or LRRK2's kinase activity (Bonello *et al.*, 2019; Wauters *et al.*, 2020). Increased mitophagy has been observed in PD patient fibroblasts (Su, Guo and Qi, 2015; Smith *et al.*, 2016). However, Hsieh *et al.* 2016 previously showed in a LRRK2-G2019S iPSC-derived neuron model that the G2019S delayed mitophagy by disrupting the interaction of LRRK2 with Miro and delaying its removal from damaged mitochondria (Hsieh *et al.*, 2016). In this study, we found that at day 15 basal mitophagy was increased in LRRK2-G2019S iNPC-derived DA neuron-like cells but by day 27 basal mitophagy was trending towards a decrease in LRRK2-G2019S iNPC-derived DA neuron-like cells compared with the control. Schwartzenuber *et al.* 2020 found that in Parkin mutant iNPC-derived DA neurons basal mitophagy increased at day 17 and became decreased at day 27. Although the changes in the Schwartzenuber *et al.* 2020 study were more substantial, it does suggest that there may be a similar mitophagy phenotype in different genetic forms of PD.

We found a significant reduction in mitochondrial ROS in the later stages of the differentiation, which is contrary to findings by Su and Qi *et al.* 2013 in iPSC-derived LRRK2-G2019S neurons (Y.-C. Su and Qi, 2013). A similar decrease in mitochondrial ROS was observed in the same patient fibroblast in Chapter 3 (mean 89% of control). This was the only manifesting fibroblast line, along with another line which showed no ATP defect, that had a reduction in mitochondrial ROS. Interestingly, overall, this fibroblast line had less severe mitochondrial dysfunction than other manifesting lines in Chapter 3, for example in SCO2 expression. Our group had some difficulties getting other LRRK2-G2019S manifesting fibroblasts lines to survive the conversion into iNPCs and the differentiation into DA neuron-like cells. This may be because their mitochondrial dysfunction was too severe to allow this.

Overall, the results from this chapter suggest that the iNPC-derived DA neuron-like cell model is useful for studying LRRK2-G2019S PD and can provide us with additional information to using other cell types as a model. We must consider however, that the data in this chapter is produced from only 1 line per group, therefore further studies are required to validate these findings.

Chapter 5 **Assessing mechanisms underlying mitochondrial complex IV deficiency in LRRK2-G2019S manifesting cells**

5.1. Introduction

The results of Chapter 1 demonstrated a trend towards a decrease in mitochondrial complex IV subunit expression and a significant decrease in mitochondrial complex IV assembly factor SCO2 expression in LRRK2-G2019S manifesting fibroblasts compared with controls. A previous study, which included some of the same cell lines, also found that complex IV activity was significantly reduced (Mortiboys *et al.*, 2015). Together, these results suggest a deficit in mitochondrial complex IV that warrants further investigation. Therefore, the aim of this chapter was to explore in greater detail the potential mechanisms underlying complex IV deficiency.

5.1.1. Complex IV assembly and the role of SCO2

Complex IV assembly was described in Chapter 1 of this thesis. There are more than 30 assembly factors involved in complex IV assembly. A proposed model of complex IV assembly is shown in **Figure 5.1**. As can be seen from the diagram, SCO2 is an essential assembly factor for complex IV and mutations in SCO2 can lead to disease. SCO2 is important for the insertion of copper into mitochondrial complex IV. **Figure 5.2** describes this process in more detail.

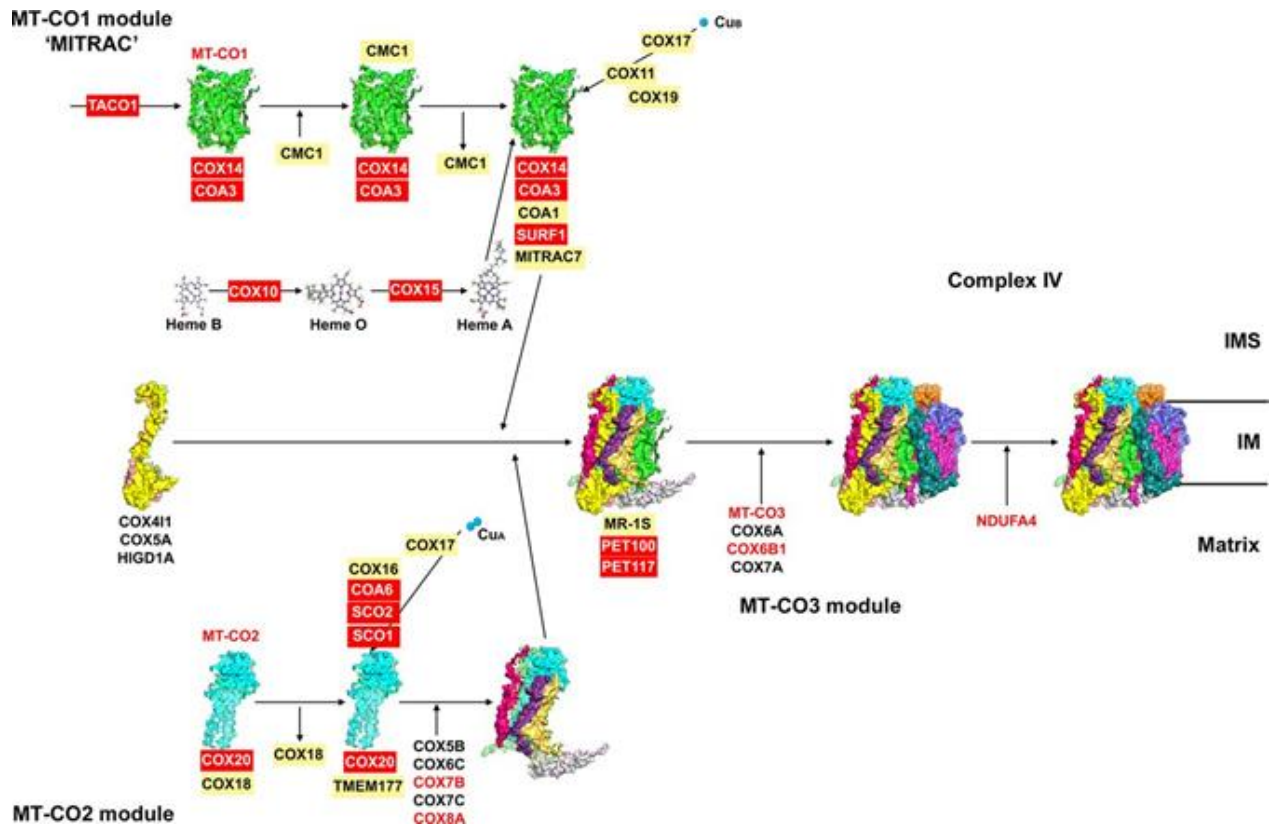


Figure 5.1. Complex IV assembly model.

Boxes show assembly factors and red represents proteins with described pathological mutations. IM, inner membrane; IMS, intermembrane space. Image taken from (Signes and Fernandez-Vizarra, 2018). Creative Commons Attribution License 4.0 (CC BY).

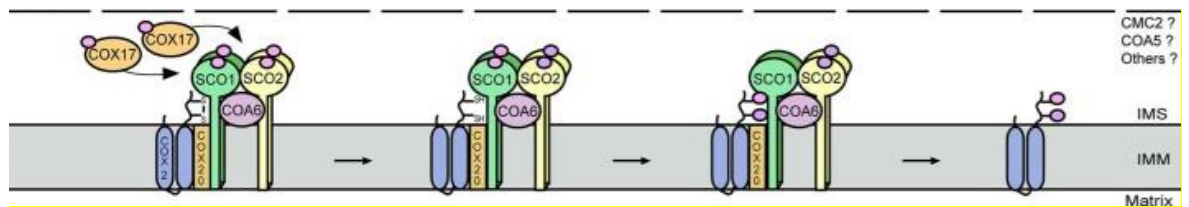


Figure 5.2. The role of SCO2 in CuA incorporation.

Image from (Jett and Leary, 2018), with copyright permission. Cu (I), pink circle; Cu(II) purple circle. COX17 delivers Cu(I) to SCO1 and SCO2. SCO2 reduces the cysteinyl sulfurs of COX2, thereby converting Cu(I) to Cu(II). This requires COA6.

Approximately 100 mg copper is stored in the human body, with 20 mg of this being in the brain (Umair and Alfadhel, 2019). The locus coeruleus and substantia nigra have the highest levels of copper in the brain (Warren, Earl and Thompson, 1960; Davies *et al.*, 2013). As well as cytochrome c oxidase (mitochondrial complex IV), there are several other key enzymes within the body that contain copper. These include superoxide dismutase, which is involved in free radical detoxification, and dopamine-beta-hydroxylase, which is essential for dopamine production in neurons (Umair and Alfadhel, 2019). As well as incorporation in the catalytic core of mitochondrial complex IV, copper plays an important role in other cellular processes, such as brain development and growth of new blood cells (Tapiero, Townsend and Tew, 2003).

5.1.2. Aims

The aim of this chapter was to explore the potential mechanisms underlying mitochondrial complex IV deficiency in LRRK2-G2019S patient tissue. To this end, we explored whether expression levels of complex IV assembly factor SCO2 were altered in LRRK2-G2019S iNPC-derived DA neuron-like cells and attempted to optimise SCO2 knockdown in control iNPC-derived DA neuron-like cells. We also explored whether either mitochondrial or cytosolic copper was affected in LRRK2-G2019S fibroblasts and iNPC-derived DA neuron-like cells.

5.2. Results

5.2.1. SCO2 expression in LRRK2-G2019S iNPC-derived DA neuron-like cells

Firstly, SCO2 expression was assessed via western blotting in the LRRK2-G2019S manifesting iNPC-derived DA neuron-like cell line to see whether the same decrease was present in neuron-like cells that was observed in the fibroblasts in Chapter 3 (**Figure 5.3**).

Interestingly, SCO2 expression was markedly decreased in the LRRK2-G2019S manifesting cell line compared to the control. The mean SCO2 expression of the neuron-like cell line was comparable to mean expression of the combined fibroblast data shown in Chapter 3. However, when comparing the same patient fibroblast line to its equivalent iNPC-derived DA neuron-like cell line (cell line NPFC-071), a more marked reduction in SCO2 expression was observed in the neuron-like cells. This is particularly interesting as the DA neurons are the cell type affected in PD.

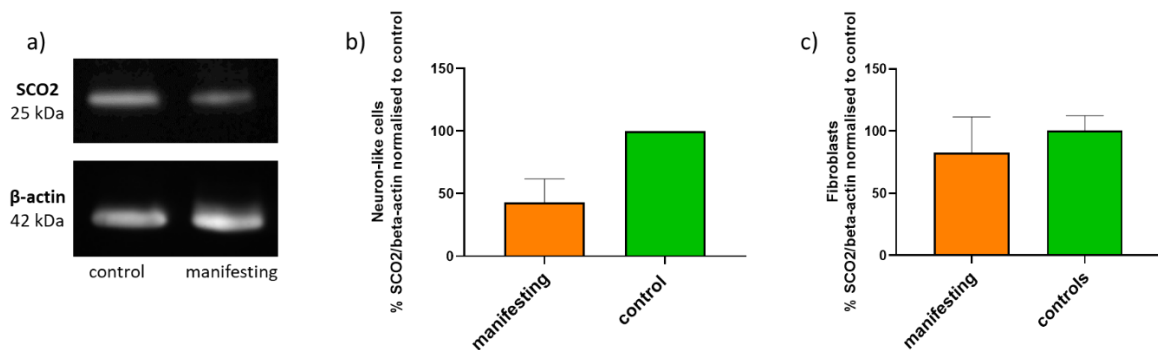


Figure 5.3. SCO2 protein expression in LRRK2-G2019S and control iNPC-derived DA neuron-like cells.

a) Representative western blot of SCO2 for LRRK2-G2019S and control iNPC-derived DA neuron-like cells at end of differentiation. Beta-actin was used as a loading control. b) Semi-quantification of SCO2/beta-actin protein expression in LRRK2-G2019S iNPC-derived DA neuron-like cells normalised to control neuron-like cells (n=2 experimental repeats). Statistical analysis was chosen not to be performed due to the low number of repeats c) Semi-quantification of SCO2/beta-actin protein expression in LRRK2-G2019S fibroblast lines from same patient as the DA neuron-like cells, normalised to combined control fibroblast data (n=3 experimental repeats of manifesting line, n=8 control lines with at least two experimental repeats per line). This data was presented in the combined SCO2 expression graph in Chapter 3. Data represent mean \pm SD.

5.2.2. *SCO2* knockdown optimisation

In order to determine whether *SCO2* expression directly affects mitochondrial function, knockdown of *SCO2* was tested in control iNPC-derived DA neuron-like cells. This was performed using *SCO2*-siRNA in Accell siRNA delivery media. Several different conditions were tested (**Figure 5.4**), however the siRNA optimisation was not successful. Contrary to what might be expected, *SCO2* expression was in fact increased when treated with *SCO2* siRNA, particularly when treated for 24 h with 24 h recovery. These findings were also seen in an additional iNPC-derived DA neuron-like cell line tested, and Accell media without siRNA) was shown to decrease *SCO2* expression compared to cells that were grown in standard neuronal media (data not shown). Further work is required to optimise *SCO2* knockdown in these cells, which time did not allow to be included in this thesis.

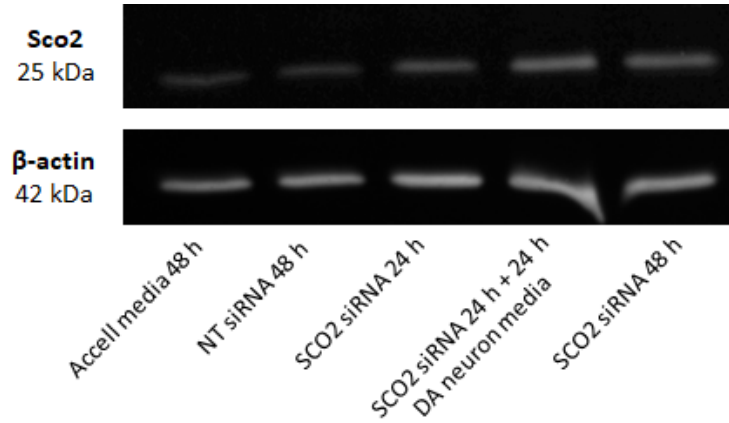


Figure 5.4. *SCO2* knockdown optimisation in control iNPC-derived DA neuron-like cells.

Control iNPC-derived DA neuron-like cells were treated at day 27 of differentiation with Accell siRNA delivery media containing NT siRNA or *SCO2* siRNA for different lengths of time. Figure shows a representative western blot of *SCO2* expression in different treatment

conditions. Beta-actin was used as a loading control. NT, non-targeting; siRNA, short interfering RNA.

5.2.3. Mitochondrial copper in fibroblasts and iNPC-derived DA neuron-like cells

As SCO2 is fundamental in incorporating Cu_A into mitochondrial complex IV, we hypothesised that there may be a change in mitochondrial copper in LRRK2-G2019S fibroblasts and iNPC-derived DA neuron-like cells. To determine this, a novel mitochondrial copper probe InCCu1, kindly donated by our collaborator Professor Elizabeth New (University of Sydney), was used to assess unbound mitochondrial copper in different cell lines (Shen *et al.*, 2016). When copper is labile in the mitochondria, i.e. not incorporated into complex IV, it binds to the copper probe and causes a decrease in fluorescent intensity. Therefore, a higher fluorescent intensity would suggest a decrease in unbound mitochondrial copper (thus a suggested increase in incorporated copper), and a lower fluorescent intensity would suggest an increase in unbound mitochondrial copper (thus a suggested decrease in incorporated copper).

We first assessed mitochondrial copper in LRRK2-G2019S manifesting, non-manifesting and control fibroblasts. As can be seen in **Figure 5.5**, there was no observable difference in mitochondrial copper between the different cell lines.

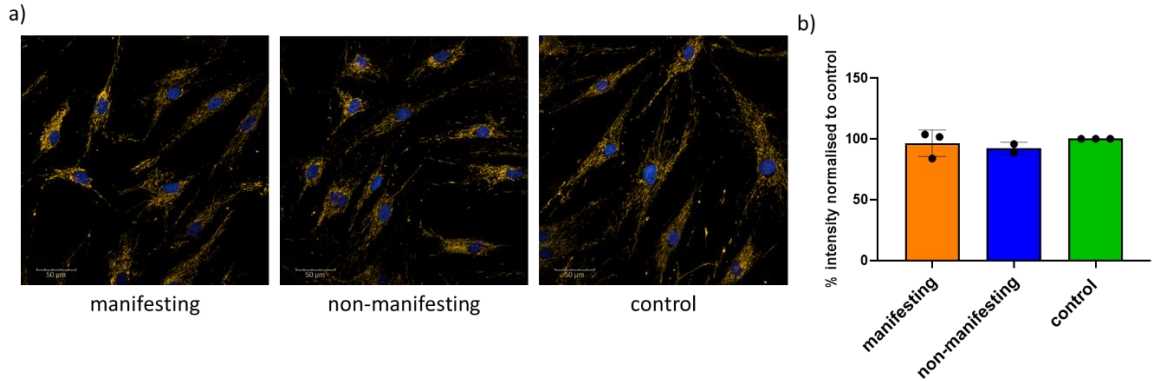


Figure 5.5. Mitochondrial copper in LRRK2-G2019S manifesting, non-manifesting and control fibroblasts.

a) Representative images of mitochondrial copper InCuu1 probe in LRRK2-G2019S manifesting, non-manifesting and control fibroblasts. Scale bar, 50 µm. b) Mitochondria were segmented using Harmony analysis software and the intensity of the mitochondrial probe was determined. Graph represents percentage of mitochondrial copper probe intensity normalised to control fibroblasts. n=3 LRRK2-G2019S manifesting, 2 LRRK-G2019S non-manifesting, 3 control cell lines. Results represent 3 experimental repeats containing at least 2 technical repeats. Data represent mean ± SD. Each dot represents the mean of the experimental repeats per differentiation.

Next, we assessed mitochondrial copper in LRRK2-G2019S and control iNPC-derived DA neuron-like cells throughout the differentiation (**Figures 5.6 and 5.7**). Unfortunately, a non-specific stain was observed in many of the fields of view at the day 27 differentiation time point, possibly due to debris accumulation, therefore this time point was excluded from quantitative analysis.

A clear difference in unbound mitochondrial copper was observed between the LRRK2-G2019S and control DA neuron-like cells. This difference was more marked throughout the differentiation, though did not reach significance ($P=0.053$ at day 22 compared with control,

Figure 5.7) .Overall, this data suggests that there is an increase in unbound mitochondrial copper in LRRK2-G2019S iNPC-derived neuron-like cells compared with the control.

SCO2 is involved in the incorporation of copper in the mitochondrial complexes, i.e. bound copper. Together with the results showing that SCO2 expression is decreased in LRRK2-G2019S iNPC-derived DA neuron-like cells, this could be suggestive of a defect in incorporation of copper into complex IV.

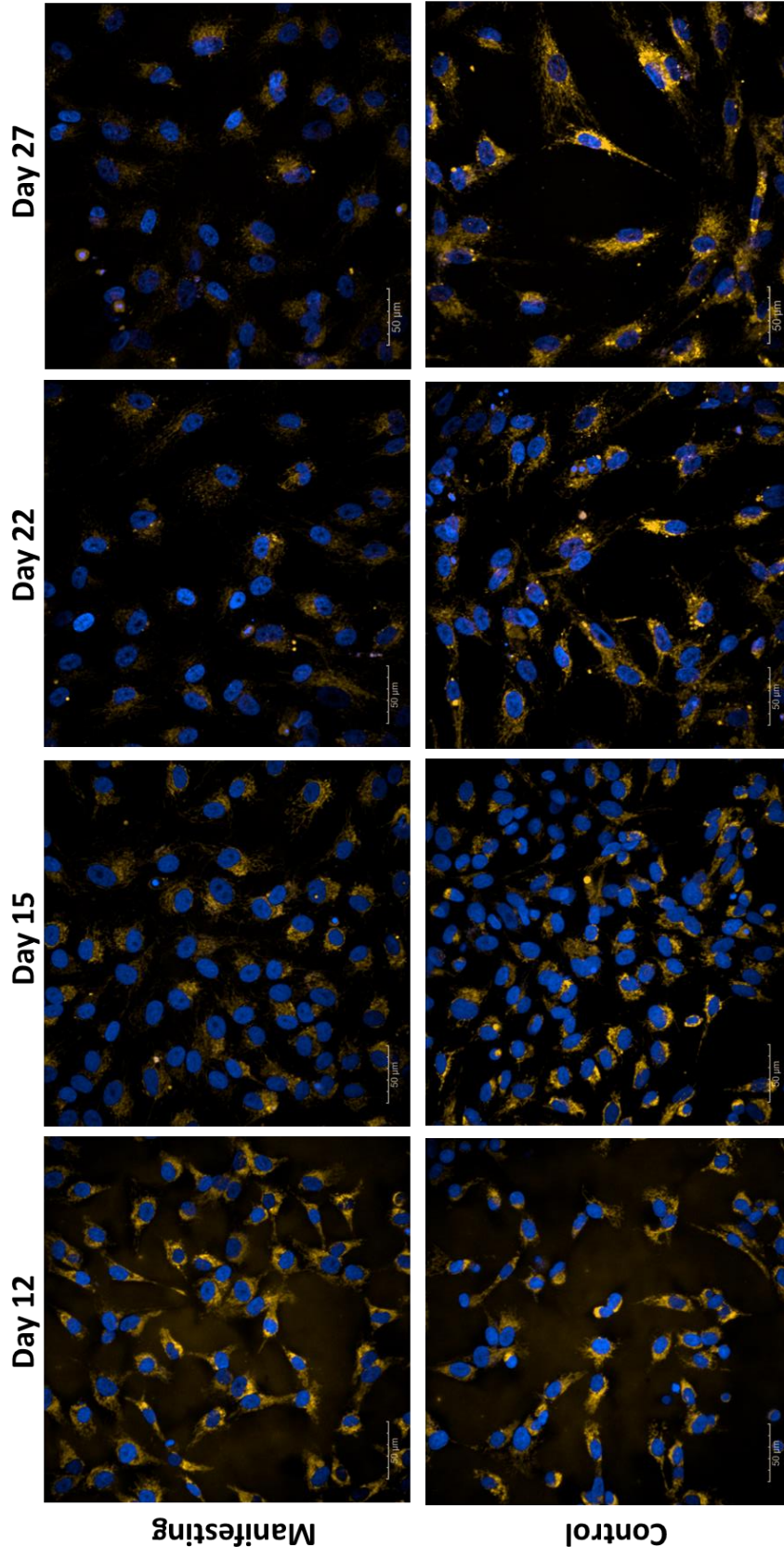


Figure 5.6. Mitochondrial copper in LRRK2-G2019S manifesting and control iNPC-derived DA neuron-like cells. Representative images of mitochondrial copper probe InCu1 in LRRK2-G2019S manifesting and control iNPC-derived DA neuron-like cells at different time points of neuron differentiation. Scale bar, 50 µm.

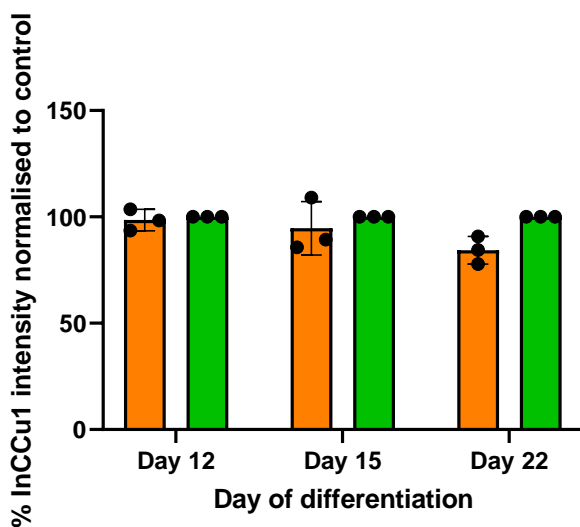


Figure 5.7. Quantification of mitochondrial copper in LRRK2-G2019S manifesting and control iNPC-derived DA neuron-like cells.

Mitochondria were segmented using Harmony analysis software and the intensity of the mitochondrial probe was determined. Graph represents percentage of mitochondrial copper probe intensity normalised to control cells. Results represent 3 experimental repeats containing 3 technical repeats. Data represent mean \pm SD. Each dot represents the mean of the experimental repeats per differentiation.

5.2.4. Cytosolic copper in fibroblasts and iNPC-derived DA neuron-like cells

It must be considered that the mitochondria are not the only compartment that copper is important in the cell. Therefore, cytosolic copper was assessed using a novel cytosolic copper probe NS2-AI-SiR, kindly donated by our collaborator Professor Christopher Chang (University of California, Berkeley).

Firstly, cytosolic copper was assessed in LRRK2-G2019S manifesting, non-manifesting and control fibroblasts, and no observable difference was found (**Figure 5.8**).

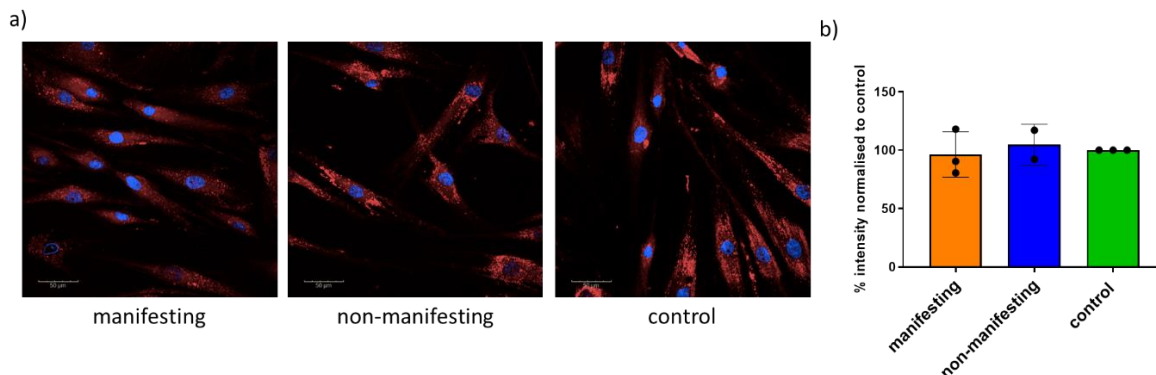


Figure 5.8. Cytosolic copper in LRRK2-G2019S manifesting, non-manifesting and control fibroblasts.

a) Representative images of cytosolic copper NS2-AI-SiR probe in LRRK2-G2019S manifesting, non-manifesting and control fibroblasts. Scale bar, 50 μ m. b) Graph represents percentage of cytosolic copper probe intensity normalised to control fibroblasts. n=3 LRRK2-G2019S manifesting, 2 LRRK-G2019S non-manifesting, 3 control cell lines. Results represent 2 experimental repeats containing 2 technical repeats. Data represent mean \pm SD. Each dot represents the mean of the experimental repeats per differentiation.

Cytosolic copper was then assessed in LRRK2-G2019S and control iNPC-derived neuron-like cells at the end of differentiation (day 27). Contrary to the changes that were observed in unbound mitochondrial copper levels, there were no significant changes in cytosolic copper probe intensity between patient and control cells (**Figure 5.9**). This is suggestive that the changes in mitochondrial copper are not due to global changes in cytosolic copper.

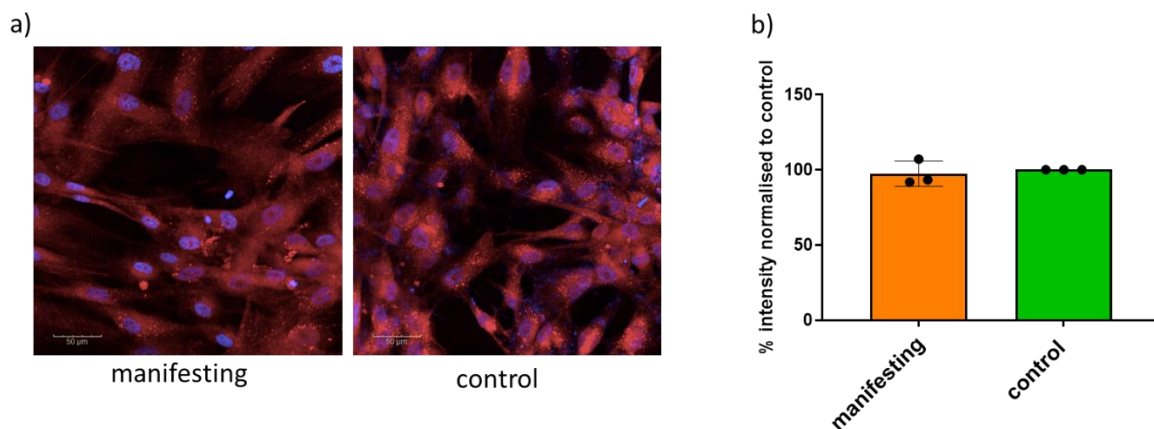


Figure 5.9. Cytosolic copper in LRRK2-G2019S manifesting and control iNPC-derived DA neuron-like cells.

a) Representative image of cytosolic copper in LRRK2-G2019S manifesting and control iNPC-derived DA neuron-like cells at the end of differentiation. Scale bar, 50 µm. b) Graph represents percentage of cytosolic copper probe intensity normalised to control iNPC-derived DA neuron-like cells at the end of differentiation. Results represent 3 experimental repeats containing 3 technical repeats. Data represent mean ± SD. Each dot represents the mean of the experimental repeats per differentiation.

5.2.5. Other mitochondrial complex IV assembly factors

The data for this section was generated by a previous MSc student in our lab, Andre Djalalvandi, who was co-supervised by Ruby Macdonald.

The focus of this chapter has been on SCO2 and the incorporation of copper into mitochondrial complex IV; however, there are many other assembly factors involved in mitochondrial complex IV biogenesis. Therefore, we wanted to test whether there were any additional complex IV assembly factors with a change in protein expression. We attempted to optimise several complex IV subunit and assembly factor antibodies for use in western blotting such as SCO1, SURF1, COX2, COX4 and COX6b1. However, we were unable to

successfully optimise these. COX15, a mitochondrial complex IV assembly factor involved in Heme A biosynthesis was successfully optimised. COX15 protein expression was shown to be significantly decreased in LRRK2-2019S manifesting fibroblasts compared with controls (**Figure 5.10**). This is suggestive that assembly factors other than SCO2 may be affected in LRRK2-G2019S PD.

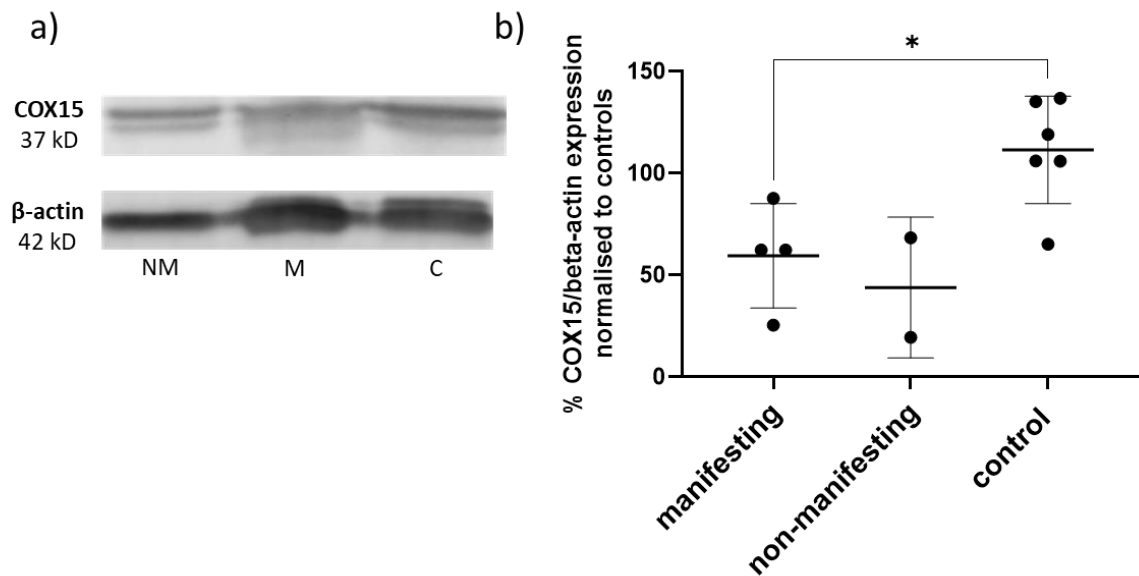


Figure 5.10. COX15 protein expression in LRRK2-G2019S manifesting, non-manifesting and control fibroblasts.

a) Representative western blot of COX15 protein expression of LRRK2-G2019S manifesting, non-manifesting and control fibroblasts. Beta-actin was used as a loading control. b) Semi-quantification of western blotting relative to controls $n= 4$ LRRK2-G2019 manifesting, 2 non-manifesting and 5 controls performed in two repeats. Data represent mean \pm SD. Each dot represents the mean of the experimental repeats per cell line. * $p<0.05$ unpaired t-test with Welch's correction.

5.3. Discussion

5.3.1. *LRRK2-G2019S SCO2 protein expression*

The aim of the first part of this chapter was to assess SCO2 expression in LRRK2-G2019S iNPC-derived DA neuron-like cells. We observed a marked decrease in SCO2 expression in patient neuron-like cells. This was a more substantial decrease than that observed in the fibroblasts from the same patient. Interestingly, the LRRK2-G2019S cell line used for neuronal differentiation was the one with the smallest change in SCO2 expression in the LRRK2-G2019S fibroblast cohort studied in Chapter 3, Figure 3.7 c. It would be interesting to see how the fibroblasts with a more substantial decrease in SCO2 expression compared when differentiated into DA neuron-like cells. As described in Chapter 4, severe mitochondrial deficits may have hindered the differentiation process and this is something that we might need to be cautious of in the future when using the iNPC-derived DA neuron-like cell model to assess PD and other conditions with a mitochondrial dysfunction.

Unfortunately attempts to knockdown SCO2 in control iNPC-derived DA neuron-like cells were unsuccessful. It may be that a longer treatment with siRNA is required in this cell type. However, other lab members have found that iNPC-derived DA neuron-like cells cultured in Accell siRNA delivery media for longer than 48 h caused substantial cell death. An unexpected finding was that SCO2 siRNA 24h + neuronal media recovery for 24 h increased SCO2 expression. One potential explanation for this is that SCO2 knockdown may have led to cell death. Therefore, the remaining cells were those with higher SCO2 levels, or cells where the knockdown was not successful. An alternative method of SCO2 knockdown that could be tested is viral transduction of short hairpin RNA. If this was unsuccessful another cell type such as SHSY5Y cells could be used.

5.3.2. LRRK2-SCO2 interaction

It is important to consider the mechanisms by which mutations in LRRK2 could affect protein expression of SCO2. LRRK2 interactions were searched on BioGRID (<https://thebiogrid.org/>), a database of protein, genetic and chemical interactions (Oughtred *et al.*, 2019). No direct interactions were found between LRRK2 and SCO2. However, HERC2, an E3 ubiquitin protein ligase was found to interact with both LRRK2 and SCO2, which could provide a potential mechanism by which LRRK2 mutations affect SCO2 expression (Galligan *et al.*, 2015; Imai *et al.*, 2015). HERC2 is involved in many functions, such as DNA damage repair, centrosome assembly, eye colour, iron metabolism and p53 regulation (García-Cano *et al.*, 2019). Deletions in the 15q11-q13 locus of HERC2 are associated with Angelman syndrome (Harlalka *et al.*, 2013). In order to assess whether HERC2 protein expression was altered in LRRK2-G2019S patient fibroblasts, we attempted to optimise western blotting for HERC2. However, due to the large size of HERC2 (528 kDa), this was technically challenging, and we were unable to visualise the protein.

5.3.3. SCO2 deficient patients and conditions associated with copper dyshomeostasis

SCO2 deficiency has thus far not been reported in PD. However, there are several cases where SCO2 mutations have led to disease. Thus far, mutations in SCO2 have been associated with fatal infantile cardioencephalomyopathy, myopia, Leigh syndrome, cerebellar ataxia and progressive peripheral axonal neuropathy, and early-onset axonal Charcot-Marie-Tooth disease (Papadopoulou *et al.*, 1999; Jaksch *et al.*, 2000; Tran-Viet *et al.*, 2013; Ruhoy and Saneto, 2014; Rebelo *et al.*, 2018; Barcia *et al.*, 2019). Interestingly, SCO2 knock-in/ knock-out mice are insulin resistant (Hill *et al.*, 2017). A large retrospective cohort linkage study found that Type II diabetes increased the risk of PD by nearly a third

(De Pablo-Fernandez *et al.*, 2018). It is too preliminary to say whether SCO2 deficiency could play a role in this increased risk of PD, but it is an interesting proposition, nonetheless.

There is evidence to suggest that SCO2 mutations lead to a decrease in COXII expression, mitochondrial complex IV activity and cellular copper levels (Jaksch *et al.*, 2001; Leary *et al.*, 2007; Yang *et al.*, 2010). Dodani *et al.* 2011 explored both cellular and mitochondrial copper in SCO2 patient fibroblasts using a targetable fluorescent sensor Mito-CS1 (Dodani *et al.*, 2011). They found that though there was a global decrease in cellular copper, labile mitochondrial Cu⁺ in SCO2 patient fibroblasts was largely unaltered. In this thesis, we found that in LRRK2-G2019S patient fibroblasts there were no significant alterations in labile mitochondrial copper, but did not observe any changes in global cellular copper.

As well as patients with SCO2 mutations, there are several other conditions associated with copper dyshomeostasis, including MEDNIK syndrome and Menkes disease (Bhattacharjee, Chakraborty and Shukla, 2017). Of particular note is Wilson's disease, which is caused by a genetic mutation in the ATP7B gene and is autosomal recessive (Bhattacharjee, Chakraborty and Shukla, 2017). Wilson's disease results in an accumulation of copper in the liver in the brain and causes Parkinsonian-like symptoms (Bandmann, Weiss and Kaler, 2015).

5.3.4. Copper in PD

Epidemiological studies have shown that long-term heavy metal exposure, including copper, increases the risk of developing PD (Montgomery, 1995). It has been proposed that copper could increase oxidative stress by converting superoxide anion and hydrogen peroxide into the hydroxyl radical, which is considered the most reactive oxygen species (Bisaglia and Bubacco, 2020). Copper has also been demonstrated to increase the

oxidation process of dopamine and has a role in the promotion of alpha-synuclein aggregation (Wang *et al.*, 2010; Pham and Waite, 2014).

However, other evidence has pointed towards a reduction in copper being associated with an increased risk of PD. For example, patients with PD have been found to have lower blood concentrations of copper compared to healthy controls (Ilyechova *et al.*, 2018). Multiple studies have shown that there is a substantial decrease in copper levels specifically in the substantia nigra of patients with PD (Dexter *et al.*, 1989; Riederer *et al.*, 1989; Genoud *et al.*, 2017). Overall, it seems likely that a balance of copper is required for normal physiological function, and dysfunction of this balance is associated with PD.

In this thesis, there were no significant changes observed in cellular copper levels, however there was an increase in the levels of unbound copper in the mitochondria of LRRK-G2019S manifesting iNPC-derived DA neuron-like cells. Together, with a decrease in SCO2 protein expression, this is suggestive of dysfunctional incorporation of copper into mitochondrial complex IV. Copper supplementation increases complex IV activity in myoblasts of patients with a SCO2 mutation (Jaksch *et al.*, 2001), suggesting copper supplementation as a potential treatment to test in LRRK2-G2019S PD. However, in the clinic, while subcutaneous injections of copper histidine improved hypertrophic cardiomyopathy in a patient with a SCO2 mutation, it did not improve CNS, muscular or respiratory functions, nor survival (Freisinger *et al.*, 2004). This may have been due to inefficient delivery of copper to the mitochondria (Soma *et al.*, 2018). Recently, elesclomol, an investigational anticancer drug, was found to increase mitochondrial copper content and rescue respiratory defects in COA6-deficient yeast cells, as well as increase mitochondrial subunit COX2 protein expression levels in SCO2 patient fibroblasts (Soma *et al.*, 2018). In future studies, it could be useful to test these compounds to see if they rescue the mitochondrial phenotype in LRRK2-G2019S patient cells. However, for clinical use, we must be cautious of the

dosage of any therapies which increase copper, due to the literature on the copper toxicity in PD.

5.3.5. *Methods for assessing copper in cells*

In this chapter, two fluorescent probes were used to measure mitochondrial and cytosolic copper respectively. The mitochondrial probe tended to not only be a mitochondrial marker, but also to show cellular debris. Therefore, data from the last time point in the neuronal differentiation protocol was deemed to not be accurate enough to assess and could not be included in the analysis. Therefore, it would be beneficial to validate these findings using other methods to detect copper. The 'gold standard' method for assessing cellular copper is to use inductively coupled mass spectrometry (ICP-MS), which can detect and quantify low copper concentrations (Williams *et al.*, 2019). This would provide us with a more accurate measure of copper levels. This would be particularly interesting in the fibroblasts, as the probes may not have been sensitive enough to detect minor changes in copper concentration.

It would be beneficial to generate mitochondrial fractions and compare these with cellular fractions using ICP-MS to validate our findings. Previously, laser ablation ICP-MS imaging has been used to detect the distribution of copper in Wilson's disease (Weiskirchen, Kim and Weiskirchen, 2019), and multi-collector ICP-MS has been used by Costas-Rodríguez *et al.* 2019 to assess cellular and mitochondrial copper in both non-differentiated and differentiated SH-SY5Y cells (Costas-Rodríguez *et al.*, 2019). Of course, the main finding of this thesis that requires further exploration is the suggested dysfunction of copper incorporation into complex IV. Our probe measures unbound copper but does not directly assess the copper that is incorporated into complex IV. To assess this, mitochondrial fractions could be generated, and the different mitochondrial complexes isolated using blue

native gel electrophoresis, or liquid chromatography. ICP-MS could then be used to quantify copper content in mitochondrial complex IV. The technical challenge however with this is the large amounts of material required to perform these experiments.

There have also been significant advancements in using synchrotron-based X-ray fluorescence microscopy to visualise copper in mammalian systems (Leary and Ralle, 2020). It would be interesting to explore this in LRRK2-G2019S mouse models. It could also be interesting to explore copper efflux and retention using ^{64}Cu .

Another aspect to mention is that the mitochondrial copper probe used in this thesis detects Cu(I) specifically. Cu(I) binds to SCO2, which functions as a thiol-disulfide oxidoreductase to reduce the cysteinyl sulfurs of COX2 (Morgada *et al.*, 2015). In this reaction, Cu(I) is converted to Cu(II). Li *et al.* 2017 have developed a mitochondrial specific Cu(II) sensor, which would be beneficial to also test in our cell lines (Li *et al.*, 2017). COA6 is required for the conversion of Cu(I) to Cu(II) and would be a particularly fundamental protein to look at in future studies (Jett and Leary, 2018).

5.3.6. Future directions

The results from this chapter suggest that the SCO2 phenotype in LRRK2-G2019S manifesting iNPC-derived DA neuron-like cells is more severe than in LRRK2-G2019S manifesting fibroblasts. It also provides evidence that mitochondrial copper might be dysregulated in LRRK2-G2019S DA neuron-like cells, but not in fibroblasts.

The majority of this chapter focussed specifically on SCO2 and copper dysregulation. However, another mitochondrial complex IV assembly factor, COX15, was also found to be decreased in manifesting LRRK2-G2019S fibroblasts. COX15 is important for the biosynthesis of heme A, a prosthetic group for complex IV. COX15 mutations have also been associated with disease (Antonicka *et al.*, 2003; Halperin *et al.*, 2020). While, COX15

is important for the assembly of the MTCO1 module of complex IV, SCO2 is important for the assembly of the MTCO2 module. This is suggestive that the two distinct modules of complex IV could both be affected in LRRK2-G2019S PD. The MTCO2 subunit, also known as COX2, was found to have a trend towards a decrease in protein expression in manifesting LRRK2-G2019S fibroblasts in Chapter 3. It would be interesting to explore COX2 protein expression in the LRRK2-G2019S iNPC-derived DA neuron-like cells to explore whether this decrease is more severe than that of the fibroblasts. Complex IV activity should also be measured in the neuron-like cells to determine whether the changes in SCO2 protein expression and mitochondrial copper lead to a decrease in mitochondrial complex IV activity.

It will be fundamental for future studies to explore in further detail the different complex IV assembly factors and subunits. This will enable us to detect whether there is a global complex IV deficiency, or whether there are certain components of the assembly pathway that are affected. The use of LRRK2-G2019S non-manifesting cells will be particularly useful here, as they may help determine which components of complex IV assembly could be affected in pre-clinical PD. As there were technical difficulties in the optimisation of many of the complex IV assembly factor and subunit antibodies tested, an alternative method would be to use reverse transcription quantitative-PCR to look at mRNA expression. Overall, these novel findings in LRRK2-G2019S PD have a lot of avenues for future exploration.

6. General Discussion

Parkinson's disease (PD) is a progressive, neurodegenerative, motor disorder affecting around 1% of the over 60 population. Leucine-Rich Repeat Kinase 2 (LRRK2) mutations are the most common cause of familial PD, with the G2019S mutation being the most common. Mitochondrial dysfunction has been previously associated with LRRK2-G2019S PD (Mortiboys *et al.*, 2017; Macdonald *et al.*, 2018), however the mechanisms underlying this dysfunction require further exploration and study. In this thesis, we explored mitochondrial dysfunction in one of the largest cohorts studied thus far of LRRK2-G2019S manifesting, non-manifesting and control fibroblasts. We also utilised a recently developed methodology to differentiate iNPCs into DA neuron-like cells (Carling *et al.*, 2020; Schwartzentruber *et al.*, 2020), in order to study LRRK2-G2019S manifesting and control cells.

We observed mitochondrial deficiencies in both LRRK2 manifesting fibroblasts and iNPC-derived DA neuron-like cells. Of note, we observed a reduction in SCO2 protein expression. SCO2 is a mitochondrial complex IV assembly factor which is involved in the incorporation of copper (Horng *et al.*, 2005). This reduction in SCO2 expression was more marked in the LRRK2-G2019S manifesting iNPC-derived DA neuron-like cells compared to the fibroblasts of the same patient. We also observed a trend towards an increase in the amount of unbound mitochondrial copper in the LRRK2-G2019S manifesting iNPC-derived DA neuron-like cells at the end of differentiation, while no difference in mitochondrial copper was observed in the LRRK2-G2019S fibroblasts. In Chapter 4 we observed a significant decrease in MMP throughout the differentiation in the LRRK2-G2019S manifesting iNPC-derived DA neuron-like cells, while an ATP deficiency was observed in some of the LRRK2-G2019S fibroblast lines. Complex IV is essential for the generating both ATP and MMP in

cells, and therefore dysfunction in complex IV assembly could be responsible for the reduction in MMP observed in the LRRK2-G2019S manifesting iNPC-derived DA neuron-like cells and the reduction in ATP observed in the LRRK2-G2019S fibroblasts.

We used two different cell models in this thesis; patient fibroblasts and iNPC-derived DA neuron-like cells. Fibroblasts have commonly been used to study LRRK2-G2019S PD (Papkovskaia *et al.*, 2012; Mortiboys, Aasly and Bandmann, 2013; Y. C. Su and Qi, 2013; Yakhine-Diop *et al.*, 2014; Mortiboys *et al.*, 2015), however this is the first study that uses iNPC-derived DA neuron-like cells for this purpose. To quote George E.P. Box, "*All models are wrong, but some are useful*". Both models used in this study have their advantages and disadvantages. For example, fibroblasts are easy to maintain and culture and retain the genotype of the patients. However, they are not the cell type that degenerates in PD, therefore may not have the same metabolic deficiencies. This was evidenced in part in this thesis as we observed differential changes in ATP and MMP between the same patient line, as well as a more exaggerated phenotype for SCO2-deficiency in the LRRK2-G2019S iNPC-derived DA neuron-like cells. On the other hand, iNPC-derived DA neuron-like cells are representative of the cell type that degenerates in PD and switch from OXPHOS throughout the differentiation (Schwartzentruber *et al.*, 2020), rather than needing to be directed to use OXPHOS by changing the cell media type. However, they are both costly and time consuming. Of course, one of the major disadvantages of both models used in this thesis is that they, for the most part, represent only a singular cell type. The human brain in reality is much more complex than this, and is composed of several different cell types, for example neurons, astrocytes and microglia. Future work could utilise a co-culture system to better represent these complexities. There has been evidence linking LRRK2 PD and neuroinflammation (Russo, Bubacco and Greggio, 2014; Russo, 2019; Schildt *et al.*, 2019). Therefore, it is important to take this into account. It would therefore be interesting to

explore the findings generated from this study in LRRK2-G2019S knock in mice (Yue *et al.*, 2015; Matikainen-Ankney *et al.*, 2018).

This thesis has focussed on mitochondrial dysfunction in LRRK2-G2019S PD, however there is a multitude of literature showing alterations in other pathways (Berwick *et al.*, 2019), and it is likely that the LRRK2-G2019S mutation affects multiple pathways. Evidence suggests that there is a convergence between the different pathways affected in LRRK2-G2019S PD (Berwick *et al.*, 2019). An example of this is the recently found link between Rab10 and mitochondrial dysfunction in LRRK2-G2019S PD. A subset of Rab GTP-ases have been previously discovered as substrates of LRRK2 (Steger *et al.*, 2016, 2017). Rabs are essential in the regulation of intracellular vesicle trafficking. Wauters *et al.* 2020 found that Rab10, a LRRK2 kinase substrate, accumulates on depolarised mitochondria and interacts with optineurin, which recruits to depolarised mitochondria and facilitates mitophagy. In LRRK2-G2019S patient fibroblasts there are reductions in Rab10 accumulation on depolarised mitochondria, Rab10 interaction with optineurin, and depolarisation-induced mitophagy. In this study, Wauters *et al.* stimulated mitophagy by depolarising cells with mitochondrial inhibitors such as CCCP. In our study, we explored basal mitophagy in iNPC-derived DA neuron-like cells, therefore it would be interesting to stimulate mitophagy with mitochondrial inhibitors to see determine whether these findings are replicated in our DA neuron-like model.

We hypothesise that mitochondrial dysfunction increases over time in iNPC-derived neuron-like cells, and this may be due to a reduction in mitophagy as the cells mature. Interestingly there is growing support that links mitochondrial biology to LRRK2. Firstly, there is the evidence that LRRK2 interacts with DRP1, which was discussed in Chapter 3. There is also evidence that LRRK2 affects mitophagy. For example, Singh *et al.* 2020 found that basal mitophagy was inversely correlated with LRRK2 kinase activity, and that using a LRRK2

kinase inhibitor rescued mitophagy defects in LRRK2-G2019S mice. Although we do not know at present if LRRK2-G2019S phosphorylation directly affects SCO2, one way to test this would be to also use a LRRK2 kinase inhibitor. This could potentially add further evidence to suggest an impact of LRRK2-G2019S on the mitochondria.

In this study, we did not observe any significant changes in the number of mitochondria per cell. However, we did not expose our cells to any mitochondrial stressors, which may be required to ascertain any differences. It will be interesting to determine whether mitochondrial biogenesis is altered in our cell models. Previous studies have shown a decrease in mitochondrial biogenesis in yeast cells and in mouse embryonic fibroblasts (Aufschnaiter *et al.*, 2018; Toyofuku *et al.*, 2020). It may be that there is build-up of dysfunctional mitochondria, but both mitophagy and biogenesis are impaired, meaning that there is not an overall change in mitochondrial number.

We also must consider how our findings relate to the LRRK2-kinase inhibitors that are undergoing clinical testing. LRRK2 kinase inhibitors were not tested in this study and could be a potential future avenue to explore. It will be interesting to assess whether kinase inhibition will affect the mitochondrial phenotype. Initial data from Katy Barnes in our group suggests that LRRK2 kinase inhibitor GSK2578215A does not affect MMP in LRRK2-G2019S fibroblasts but provides a mild increase in MMP in LRRK2-G2019S neuron-like cells. In addition, GSK2578215A treatment led to a significant reduction in lysosomal number, to below control levels. It will also be interesting to assess whether the LRRK2-G2019S iNPC-derived neuron-like cells used in this study have an increased kinase activity.

LRRK2-G2019S is not the only mutation in LRRK2 that leads to PD, therefore it will be important to explore whether mutations, such as those in the GTPase domain produce a similar mitochondrial phenotype. Other studies have found that in patient fibroblasts the R1441C mutation caused increased vulnerability of cells to valinomycin, heightened

mitophagy, and increased mitochondria fragmentation, as well as reduced oxygen consumption in iPSC-derived neurons and delayed mitophagy (Smith *et al.*, 2016; Wauters *et al.*, 2020), This suggests that there could be some overlap in mitochondrial dysfunction between mutations in different LRRK2 domains.

Finally, as a mitochondrial complex IV assembly deficient phenotype was observed in this thesis it is important that future studies explore this further. Our current evidence suggests that complex IV deficiencies are not specific to SCO2 as COX15 was decreased in LRRK2-G2019S manifesting fibroblasts compared to controls. Therefore, other mitochondrial complex IV subunits and assembly will need to be explored. As some evidence suggests that there is a complex IV deficiency in sporadic PD (Carling *et al.*, 2020) it will be interesting to see whether these findings are translatable beyond LRRK2-G2019S PD.

References

Ackerman, S. H. (2002) 'Atp11p and Atp12p are chaperones for F(1)-ATPase biogenesis in mitochondria.', *Biochimica et Biophysica Acta*, 1555(1–3), p. 101–5.

Aguer, C. et al. (2011) 'Galactose enhances oxidative metabolism and reveals mitochondrial dysfunction in human primary muscle cells.', *PloS One*, 6(12), p. e28536.

Ahlqvist, G., Landin, S. and Wroblewski, R. (1975) 'Ultrastructure of skeletal muscle in patients with Parkinson's disease and upper motor lesions.', *Laboratory Investigation; a Journal of Technical Methods and Pathology*, 32(5), p. 673–9.

Alegre-Abarrategui, J. et al. (2008) 'LRRK2 is a component of granular alpha-synuclein pathology in the brainstem of Parkinson's disease', *Neuropathology and Applied Neurobiology*, 34(3), p. 272-283.

Anand, R. et al. (2014) 'The i-AAA protease YME1L and OMA1 cleave OPA1 to balance mitochondrial fusion and fission', *The Journal of Cell Biology*, 204(6), p. 919-926.

Annesley, S. J. et al. (2016) 'Immortalized Parkinson's disease lymphocytes have enhanced mitochondrial respiratory activity', *DMM Disease Models and Mechanisms*, 9(11), p. 1295-1305.

Antonicka, H. et al. (2003) 'Mutations in COX15 produce a defect in the mitochondrial heme biosynthetic pathway, causing early-onset fatal hypertrophic cardiomyopathy', *American Journal of Human Genetics*, 72(1), p. 101-114.

Araki, M., Ito, G. and Tomita, T. (2018) 'Physiological and pathological functions of LRRK2: implications from substrate proteins', *Neuronal Signaling*, 2(4), p. NS20180005.

Ascherio, A. and Schwarzschild, M. A. (2016) 'The epidemiology of Parkinson's disease: risk factors and prevention', *The Lancet Neurology*, 15(12), p. 1257–1272.

Auburger, G. et al. (2012) 'Primary skin fibroblasts as a model of Parkinson's disease', *Molecular Neurobiology*, 46(1), p. 20–27.

Aufschnaiter, A. et al. (2018) 'The enzymatic core of the parkinson's disease-associated protein LRRK2 impairs mitochondrial biogenesis in aging yeast', *Frontiers in Molecular Neuroscience*, 11, p. 205.

Auten, R. L. and Davis, J. M. (2009) 'Oxygen toxicity and reactive oxygen species: The devil is in the details', *Pediatric Research*, 66(2), p. 121-127.

Ayano, G. (2016) 'Dopamine: Receptors, Functions, Synthesis, Pathways, Locations and Mental Disorders: Review of Literatures', *Journal of Mental Disorders and Treatment*, 2(2), p. 1–4.

Bailey, R. M. et al. (2013) 'LRRK2 phosphorylates novel tau epitopes and promotes tauopathy', *Acta Neuropathologica*, 126(6), p. 809-827.

Ban, T. et al. (2017) 'Molecular basis of selective mitochondrial fusion by heterotypic action between OPA1 and cardiolipin', *Nature Cell Biology*, 19(7), p. 856-863.

Ban, T. et al. (2018) 'Relationship between OPA1 and cardiolipin in mitochondrial inner-membrane fusion', *Biochimica et Biophysica Acta – Bioenergetics*, 1859(9), p. 951-957.

Bandmann, O., Weiss, K. H. and Kaler, S. G. (2015) 'Wilson's disease and other neurological copper disorders', *The Lancet Neurology*, 14(1), p. 103-113.

Barcia, G. et al. (2019) 'Cytochrome c oxidase deficiency caused by biallelic SCO2 mutations in two sibs with cerebellar ataxia and progressive peripheral axonal neuropathy', *Molecular Genetics and Metabolism Reports*, 21, p. 100528.

Barros, M. H. and Tzagoloff, A. (2002) 'Regulation of the heme A biosynthetic pathway in *Saccharomyces cerevisiae*.', *FEBS Letters*, 516(1–3), p. 119–23.

Bayreuther, K. et al. (1991) 'Differentiation of primary and secondary fibroblasts in cell culture systems.', *Mutation Research*, 256(2–6), p. 233–42.

Bedford, L. et al. (2008) 'Depletion of 26S Proteasomes in Mouse Brain Neurons Causes Neurodegeneration and Lewy-Like Inclusions Resembling Human Pale Bodies', *Journal of Neuroscience*, 28(33), p. 8189–8198.

Benamer, H. T. S. and De Silva, R. (2010) 'LRRK2 G2019S in the North African population: A review', *European Neurology*, 63(6), p. 321-5.

Bender, A. et al. (2006) 'High levels of mitochondrial DNA deletions in substantia nigra neurons in aging and Parkinson disease', *Nature Genetics*, 38(5), p. 515–517.

Berg, J. M., Tymoczko, J. L. and Stryer, L. (2012) *Biochemistry*. 7th edn. Basingstoke: W.H. Freeman.

Berwick, D. C. et al. (2019) 'LRRK2 Biology from structure to dysfunction: Research progresses, but the themes remain the same', *Molecular Neurodegeneration*, 14(1), p. 49.

Bhattacharjee, A., Chakraborty, K. and Shukla, A. (2017) 'Cellular copper homeostasis: Current concepts on its interplay with glutathione homeostasis and its implication in physiology and human diseases', *Metallomics*, 9(10), p. 1376-1388.

Bisaglia, M. and Bubacco, L. (2020) 'Copper ions and Parkinson's disease: Why is homeostasis so relevant?', *Biomolecules*, 10(2), p. 195.

Biskup, S. et al. (2006) 'Localization of LRRK2 to membranous and vesicular structures in mammalian brain', *Annals of Neurology*, 60(5), p. 557–569.

Bonello, F. et al. (2019) 'LRRK2 impairs PINK1/Parkin-dependent mitophagy via its kinase activity: Pathologic insights into Parkinson's disease', *Human Molecular Genetics*, 28(10), p. 1645–1660.

Bose, A. and Beal, M. F. (2016) 'Mitochondrial dysfunction in Parkinson's disease', *Journal of Neurochemistry*, 139, p. 216–231.

Braak, H. et al. (2003) 'Staging of brain pathology related to sporadic Parkinson's disease', *Neurobiology of Aging*, 24(2), p. 197–211.

Braak, H. et al. (2004) 'Stages in the development of Parkinson's disease-related pathology', *Cell and Tissue Research*, 318(1), p. 121–134.

Brüggemann, N. and Klein, C. (1993) Parkin Type of Early-Onset Parkinson Disease, GeneReviews®.

Busiello, R. A., Savarese, S. and Lombardi, A. (2015) 'Mitochondrial uncoupling proteins and energy metabolism.', *Frontiers in Physiology*, 6, p. 36.

Carling, P. J. et al. (2020) 'Deep phenotyping of peripheral tissue facilitates mechanistic disease stratification in sporadic Parkinson's disease', *Progress in Neurobiology*, 187, p. 101772.

Carroll, J. et al. (2006) 'Bovine Complex I Is a Complex of 45 Different Subunits', *Journal of Biological Chemistry*, 281(43), p. 32724–32727.

Cecchini, G. (2003) 'Function and Structure of Complex II of the Respiratory Chain', *Annual Review of Biochemistry*, 72(1), p. 77–109.

Chaban, Y., Boekema, E. J. and Dudkina, N. V. (2014) 'Structures of mitochondrial oxidative phosphorylation supercomplexes and mechanisms for their stabilisation', *Biochimica et Biophysica Acta (BBA) - Bioenergetics*, 1837(4), p. 418–426.

Chakrabarti, R. et al. (2018) 'INF2-mediated actin polymerization at the ER stimulates mitochondrial calcium uptake, inner membrane constriction, and division', *Journal of Cell Biology*, 217(1), p. 251-268.

Chan, D. C. (2006) 'Mitochondrial fusion and fission in mammals', *Annual Review of Cell and Developmental Biology*, 22, p. 79-99.

Cheng, H.-C., Ulane, C. M. and Burke, R. E. (2010) 'Clinical progression in Parkinson disease and the neurobiology of axons.', *Annals of Neurology*, 67(6), p. 715–25.

Cherra, S. J. et al. (2013) 'Mutant LRRK2 Elicits Calcium Imbalance and Depletion of Dendritic Mitochondria in Neurons', *The American Journal of Pathology*, 182(2), p. 474–484.

Chinnery, P. F. and Hudson, G. (2013) 'Mitochondrial genetics', *British Medical Bulletin*, 106(1) p. 135-59.

Cho, B. et al. (2017) 'Constriction of the mitochondrial inner compartment is a priming event for mitochondrial division', *Nature Communications*, 8, p. 15754.

Cipolat, S. et al. (2004) 'OPA1 requires mitofusin 1 to promote mitochondrial fusion', *Proceedings of the National Academy of Sciences of the United States of America*, 101(45), p. 15927-32.

Civiero, L. et al. (2012) 'Biochemical Characterization of Highly Purified Leucine-Rich Repeat Kinases 1 and 2 Demonstrates Formation of Homodimers', *PLoS One*, 7(8), p. e43472.

Clark, I. E. et al. (2006) 'Drosophila pink1 is required for mitochondrial function and interacts genetically with parkin', *Nature*, 441(7097), p. 1162–1166.

Cooper, O. et al. (2012) 'Pharmacological Rescue of Mitochondrial Deficits in iPSC-Derived Neural Cells from Patients with Familial Parkinson's Disease', *Science Translational Medicine*, 4(141), p. 141ra90-141ra90.

Corona, J. C. and Duchen, M. R. (2015) 'PPAR γ and PGC-1 α as therapeutic targets in Parkinson's.', *Neurochemical Research*, 40(2), p. 308–16.

Costas-Rodríguez, M. et al. (2019) 'Cellular and sub-cellular Cu isotope fractionation in the human neuroblastoma SH-SY5Y cell line: proliferating versus neuron-like cells', *Analytical and Bioanalytical Chemistry*, 411(19), p. 4963-4971

Coxhead, J. et al. (2016) 'Somatic mtDNA variation is an important component of Parkinson's disease', *Neurobiology of Aging*, 38, p. 217.e1-217.e6.

Dauer, W. and Przedborski, S. (2003) 'Parkinson's disease: mechanisms and models.', *Neuron*, 39(6), p. 889–909.

Davies, K. M. et al. (2013) 'Localization of copper and copper transporters in the human brain', *Metallomics*, 5(1), p. 43-51

Delcambre, S. et al. (2020) 'Mitochondrial Mechanisms of LRRK2 G2019S Penetrance', *Frontiers in Neurology*, 11, p. 881

Dennerlein, S. and Rehling, P. (2015) 'Human mitochondrial COX1 assembly into cytochrome c oxidase at a glance.', *Journal of Cell Science*, 128(5), p. 833–7.

Dexter, D. T. et al. (1989) 'Increased Nigral Iron Content and Alterations in Other Metal Ions Occurring in Brain in Parkinson's Disease', *Journal of Neurochemistry*, 52(6), p. 1830-1836.

Diot, A. et al. (2015) 'A novel quantitative assay of mitophagy: Combining high content fluorescence microscopy and mitochondrial DNA load to quantify mitophagy and identify novel pharmacological tools against pathogenic heteroplasmic mtDNA', *Pharmacological Research*, 100, p. 24–35.

Dodani, S. C. et al. (2011) 'A Targetable Fluorescent Sensor Reveals That Copper-Deficient SCO1 and SCO2 Patient Cells Prioritize Mitochondrial Copper Homeostasis', *Journal of the American Chemical Society*, 133(22), p. 8606–8616.

Dölle, C. et al. (2016) 'Defective mitochondrial DNA homeostasis in the substantia nigra in Parkinson disease.', *Nature Communications*, 7, p. 13548.

Doty, R. L., Deems, D. A. and Stellar, S. (1988) 'Olfactory dysfunction in parkinsonism: a general deficit unrelated to neurologic signs, disease stage, or disease duration.', *Neurology*, 38(8), p. 1237–44.

Ebrahim, A. S., Ko, L.-W. and Yen, S.-H. (2010) 'Reduced expression of peroxisome-proliferator activated receptor gamma coactivator-1alpha enhances alpha-synuclein oligomerization and down regulates AKT/GSK3beta signaling pathway in human neuronal cells that inducibly express alpha-synuclein.', *Neuroscience Letters*, 473(2), p. 120–5.

Engelender, S. and Isacson, O. (2017) 'The Threshold Theory for Parkinson's Disease', *Trends in Neurosciences*, 40(1), p. 4–14.

Ernster, L. and Schatz, G. (1981) 'Mitochondria: a historical review.', *The Journal of Cell Biology*, 91(3), p. 227s-255s.

Fernández-Vizarra, E., Tiranti, V. and Zeviani, M. (2009) 'Assembly of the oxidative phosphorylation system in humans: what we have learned by studying its defects.', *Biochimica et Biophysica Acta*, 1793(1), p. 200–11.

Flinn, L. et al. (2009) 'Complex I deficiency and dopaminergic neuronal cell loss in parkin-deficient zebrafish (*Danio rerio*)', *Brain*, 132(6), p. 1613–1623.

Flinn, L. J. et al. (2013) 'TigarB causes mitochondrial dysfunction and neuronal loss in PINK1 deficiency', *Annals of Neurology*, 74(6), p. 837–847.

Fraser, K. B. et al. (2016) 'Urinary LRRK2 phosphorylation predicts parkinsonian phenotypes in G2019S LRRK2 carriers', *Neurology*, 86(11), p. 994–999.

Freisinger, P. et al. (2004) 'Reversion of hypertrophic cardiomyopathy in a patient with deficiency of the mitochondrial copper binding protein Sco2: Is there a potential effect of copper?', *Journal of Inherited Metabolic Disease*, 27(1), p. 67–79.

Fu, X. et al. (2013) 'LRRK2 G2385R and LRRK2 R1628P increase risk of Parkinson's disease in a Han Chinese population from Southern Mainland China', *Parkinsonism and Related Disorders*, 19(3), p. 397–398.

Galligan, J. T. et al. (2015) 'Proteomic analysis and identification of cellular interactors of the giant ubiquitin ligase HERC2', *Journal of Proteome Research*, 14(2), p. 953–966.

García-Cano, J. et al. (2019) 'Hercing: Structural and functional relevance of the large herc ubiquitin ligases', *Frontiers in Physiology*, 10, p. 1014.

Gatto, N. et al. (2021) 'Directly converted astrocytes retain the ageing features of the donor fibroblasts and elucidate the astrocytic contribution to human CNS health and disease', *Aging Cell*, 20(1), p. e13281.

Genoud, S. et al. (2017) 'Subcellular compartmentalisation of copper, iron, manganese, and zinc in the Parkinson's disease brain', *Metallomics*, 9(10), p. 1447–1455.

Ghezzi, D. and Zeviani, M. (2012) 'Assembly Factors of Human Mitochondrial Respiratory Chain Complexes: Physiology and Pathophysiology', *Advances in Experimental Medicine and Biology*, 748, p. 65–106.

Giroto, S. et al. (2012) 'Dopamine-derived quinones affect the structure of the redox sensor DJ-1 through modifications at Cys-106 and Cys-53.', *The Journal of Biological Chemistry*, 287(22), p. 18738–49.

Godena, V. K. et al. (2014) 'Increasing microtubule acetylation rescues axonal transport and locomotor deficits caused by LRRK2 Roc-COR domain mutations', *Nature Communications*, 5, p. 5245.

Gómez-Suaga, P. et al. (2014) 'LRRK2 delays degradative receptor trafficking by impeding late endosomal budding through decreasing Rab7 activity', *Human Molecular Genetics*, 23(25), p. 6779–6796.

González-Casacuberta, I. et al. (2019) 'Mitochondrial and autophagic alterations in skin fibroblasts from Parkinson disease patients with Parkin mutations', *Aging*, 11(11), p. 3750–3767.

Gray, M. W. (2012) 'Mitochondrial evolution.', *Cold Spring Harbor Perspectives in Biology*, 4(9), p. a011403.

Greene, J. C. et al. (2003) 'Mitochondrial pathology and apoptotic muscle degeneration in *Drosophila parkin* mutants.', *Proceedings of the National Academy of Sciences of the United States of America*, 100(7), p. 4078–83.

Greggio, E. et al. (2006) 'Kinase activity is required for the toxic effects of mutant LRRK2/dardarin', *Neurobiology of Disease*, 23(2), p. 329–341.

Grünewald, A. et al. (2014) 'Does uncoupling protein 2 expression qualify as marker of disease status in LRRK2-associated Parkinson's disease?', *Antioxidants & Redox Signaling*, 20(13), p. 1955–60.

Guaitoli, G. et al. (2016) 'Structural model of the dimeric Parkinson's protein LRRK2 reveals a compact architecture involving distant interdomain contacts', *Proceedings of the National Academy of Sciences of the United States of America*, 113(30), p. E4357–E4366.

Haaxma, C. A. et al. (2007) 'Gender differences in Parkinson's disease.', *Journal of Neurology, Neurosurgery, and Psychiatry*, 78(8), p. 819–24.

Haddad, D. and Nakamura, K. (2015) 'Understanding the susceptibility of dopamine neurons to mitochondrial stressors in Parkinson's disease', *FEBS Letters*, 589(24PartA), p. 3702–3713.

Haehner, A. et al. (2009) 'Prevalence of smell loss in Parkinson's disease – A multicenter study', *Parkinsonism & Related Disorders*, 15(7), p. 490–494.

Hall, C. N. et al. (2012) 'Oxidative phosphorylation, not glycolysis, powers presynaptic and postsynaptic mechanisms underlying brain information processing', *Journal of Neuroscience*, 32(26), p. 8940–8951.

Halperin, D. et al. (2020) 'Phenotypic variability and mutation hotspot in COX15-related Leigh syndrome', *American Journal of Medical Genetics, Part A*, 182(6), p. 1506–1512.

Hames, B. and Hooper, N. (1997) *Instant notes in biochemistry*. 4th edn, Biochemical Education. Garland Science, Taylor & Francis Group.

Han, H. et al. (2020) 'PINK1 phosphorylates Drp1S616 to regulate mitophagy-independent mitochondrial dynamics'. *EMBO Reports*, 5;21(8), p. e48686.

Hanafi, N. I. et al. (2016) 'Ursodeoxycholic acid upregulates ERK and Akt in the protection of cardiomyocytes against CoCl₂', *Genetics and Molecular Research*, 15(2).

Harlalka, G. V. et al. (2013) 'Mutation of HERC2 causes developmental delay with angelman-like features', *Journal of Medical Genetics*, 50(2), p. 65–73.

Haugarvoll, K. et al. (2007) 'Variants in the LRRK1 gene and susceptibility to Parkinson's disease in Norway', *Neuroscience Letters*, 416(3), p. 299–301.

Healy, D. G. et al. (2008) 'Phenotype, genotype, and worldwide genetic penetrance of LRRK2-associated Parkinson's disease: a case-control study.', *The Lancet. Neurology*, 7(7), p. 583–90.

Henderson, M. X. et al. (2019) 'Alzheimer's disease tau is a prominent pathology in LRRK2 Parkinson's disease', *Acta Neuropathologica Communications*, 7(1), p. 183.

Henry, A. G. et al. (2015) 'Pathogenic LRRK2 mutations, through increased kinase activity, produce enlarged lysosomes with reduced degradative capacity and increase ATP13A2 expression', *Human Molecular Genetics*, 24(21), p. 6013–6028.

Heo, H. Y. et al. (2010) 'LRRK2 enhances oxidative stress-induced neurotoxicity via its kinase activity', *Experimental Cell Research*, 316(4), p. 649–656.

Heras-Garvin, A. and Stefanova, N. (2020) 'From Synaptic Protein to Prion: The Long and Controversial Journey of α -Synuclein', *Frontiers in Synaptic Neuroscience*, 12, p. 584536.

Herzig, M. C. et al. (2011) 'LRRK2 protein levels are determined by kinase function and are crucial for kidney and lung homeostasis in mice', *Human Molecular Genetics*, 20(21), p. 4209–4223.

Hill, S. et al. (2017) 'Sco2 deficient mice develop increased adiposity and insulin resistance', *Molecular and Cellular Endocrinology*, 455, p. 103–114.

Hinson, J. T. et al. (2007) 'Missense Mutations in the BCS1L Gene as a Cause of the Björnstad Syndrome', *New England Journal of Medicine*, 356(8), p. 809–819.

Hofhaus, G. et al. (1996) 'Respiration and growth defects in transmitochondrial cell lines carrying the 11778 mutation associated with Leber's hereditary optic neuropathy', *Journal of Biological Chemistry*, 271(22), p. 13155–13161.

Horng, Y.-C. et al. (2005) 'Human Sco1 and Sco2 Function as Copper-binding Proteins', *Journal of Biological Chemistry*, 280(40), p. 34113–34122.

Hsieh, C.-H. et al. (2016) 'Functional Impairment in Miro Degradation and Mitophagy Is a Shared Feature in Familial and Sporadic Parkinson's Disease', *Cell Stem Cell*, 19(6), p. 709–724.

Hui, K. Y. et al. (2018) 'Functional variants in the LRRK2 gene confer shared effects on risk for Crohn's disease and Parkinson's disease', *Science Translational Medicine*, 10(423), p. eaai7795.

Ilyechova, E. Y. et al. (2018) 'A low blood copper concentration is a co-morbidity burden factor in Parkinson's disease development', *Neuroscience Research*, 135, p. 54–62.

Imai, Y. et al. (2015) 'The Parkinson's Disease-Associated Protein Kinase LRRK2 Modulates Notch Signaling through the Endosomal Pathway', *PLoS Genetics*, 11(9), p. e1005503.

Imaizumi, Y. et al. (2012) 'Mitochondrial dysfunction associated with increased oxidative stress and α -synuclein accumulation in PARK2 iPSC-derived neurons and postmortem brain tissue', *Molecular Brain*, 5(1), p. 35.

Ito, G. et al. (2014) 'Lack of correlation between the kinase activity of LRRK2 harboring kinase-modifying mutations and its phosphorylation at Ser910, 935, and Ser955', *PLoS One*, 9(5), p. e97988.

Jaksch, M. et al. (2000) 'Mutations in SCO2 are associated with a distinct form of hypertrophic cardiomyopathy and cytochrome c oxidase deficiency', *Human Molecular Genetics*, 9(5), p. 795–801.

Jaksch, M. et al. (2001) 'Cytochrome c oxidase deficiency due to mutations in SCO2, encoding a mitochondrial copper-binding protein, is rescued by copper in human myoblasts.', *Human Molecular Genetics*, 10(26), p. 3025–35.

Jaleel, M. et al. (2007) 'LRRK2 phosphorylates moesin at threonine-558: Characterization of how Parkinson's disease mutants affect kinase activity', *Biochemical Journal*, 405(2), p. 307–317.

Jett, K. A. and Leary, S. C. (2018) 'Building the CuA site of cytochrome c oxidase: A complicated, redox-dependent process driven by a surprisingly large complement of accessory proteins', *Journal of Biological Chemistry*, 293(13), p. 4644–4652.

Jonckheere, A. I., Smeitink, J. A. M. and Rodenburg, R. J. T. (2012) 'Mitochondrial ATP synthase: architecture, function and pathology.', *Journal of Inherited Metabolic Disease*, 35(2), p. 211–25.

Jorgensen, N. D. et al. (2009) 'The WD40 domain is required for LRRK2 neurotoxicity', *PLoS One*, 4(12), p. e8463.

Juárez-Flores, D. L. et al. (2018) 'Exhaustion of mitochondrial and autophagic reserve may contribute to the development of LRRK2 G2019S -Parkinson's disease', *Journal of Translational Medicine*, 16(1), p. 160.

Kalia, L. and Lang, A. (2015) 'Parkinson's disease', *The Lancet*, 386(9996), p. 896–912.

Kalyanaraman, B. et al. (2012) 'Measuring reactive oxygen and nitrogen species with fluorescent probes: Challenges and limitations', *Free Radical Biology and Medicine*, 52(1), p. 1–6.

Kamerkar, S. C. et al. (2018) 'Dynamin-related protein 1 has membrane constricting and severing abilities sufficient for mitochondrial and peroxisomal fission', *Nature Communications*, 9(1), p. 5239.

Kaur, A. et al. (2015) 'Mitochondrially targeted redox probe reveals the variations in oxidative capacity of the haematopoietic cells', *Organic & Biomolecular Chemistry*, 13(24), p. 6686–6689.

Kaur, A. et al. (2016) 'Studies of Hematopoietic Cell Differentiation with a Ratiometric and Reversible Sensor of Mitochondrial Reactive Oxygen Species.', *Antioxidants & Redox Signaling*, 24(13), p. 667–79.

Klein, C. and Westenberger, A. (2012) 'Genetics of Parkinson's disease', *Cold Spring Harbor Perspectives in Medicine*, 2(1), p. a008888.

Korecka, J. A. et al. (2019) 'Mitochondrial clearance and maturation of autophagosomes are compromised in LRRK2 G2019S familial Parkinson's disease patient fibroblasts', *Human Molecular Genetics*, 28(19), p. 3232–3243.

Korecka, J. A. et al. (2020) 'Splice-Switching Antisense Oligonucleotides Reduce LRRK2 Kinase Activity in Human LRRK2 Transgenic Mice', *Molecular Therapy - Nucleic Acids*, 21, p. 623–635.

Koyano, F. et al. (2014) 'Ubiquitin is phosphorylated by PINK1 to activate parkin', *Nature*, 510(7503), p. 162–6.

Kühlbrandt, W. (2015) 'Structure and function of mitochondrial membrane protein complexes', *BMC Biology*, 13(1), p. 89.

Kuwahara, T. and Iwatsubo, T. (2020) 'The Emerging Functions of LRRK2 and Rab GTPases in the Endolysosomal System', *Frontiers in Neuroscience*, 14, p. 227.

Lach, B. et al. (1992) 'Caudate nucleus pathology in Parkinson's disease: ultrastructural and biochemical findings in biopsy material.', *Acta Neuropathologica*, 83(4), p. 352–60.

Lapiente-Brun, E. et al. (2013) 'Supercomplex Assembly Determines Electron Flux in the Mitochondrial Electron Transport Chain', *Science*, 340(6140), p. 1567–1570.

Latourelle, J. C. et al. (2008) 'The Gly2019Ser mutation in LRRK2 is not fully penetrant in familial Parkinson's disease: the GenePD study', *BMC Medicine*, 6(1), p. 32.

de Lau, L. M. and Breteler, M. M. (2006) 'Epidemiology of Parkinson's disease', *The Lancet Neurology*, 5(6), p. 525–535.

Leary, S. C. et al. (2007) 'The Human Cytochrome c Oxidase Assembly Factors SCO1 and SCO2 Have Regulatory Roles in the Maintenance of Cellular Copper Homeostasis', *Cell Metabolism*, 5(1), p. 9–20.

Leary, S. C. and Ralle, M. (2020) 'Advances in visualization of copper in mammalian systems using X-ray fluorescence microscopy', *Current Opinion in Chemical Biology*, 55, p. 19–25.

Lee, J. E. et al. (2016) 'Multiple dynamin family members collaborate to drive mitochondrial division', *Nature*, 540(7631), p. 139–143.

Lees, J. G., Gardner, D. K. and Harvey, A. J. (2018) 'Mitochondrial and glycolytic remodeling during nascent neural differentiation of human pluripotent stem cells', *Development (Cambridge)*, 145(20), p. dev168997.

Lenaz, G. et al. (2006) 'Mitochondrial Complex I: Structural and functional aspects', *Biochimica et Biophysica Acta (BBA) - Bioenergetics*, 1757(9), p. 1406–1420.

Li, H. et al. (2017) 'Real-time detection and imaging of copper(ii) in cellular mitochondria', *Organic and Biomolecular Chemistry*, 15(3), p. 598–604.

Lill, C. M. and Klein, C. (2017) 'The Neurogenetics of Parkinson's Disease and Putative Links to Other Neurodegenerative Disorders', in Parkinson's Disease: Molecular Mechanisms Underlying Pathology.

Lin, C. H. et al. (2010) 'LRRK2 G2019S mutation induces dendrite degeneration through mislocalization and phosphorylation of tau by recruiting autoactivated GSK3 β ', Journal of Neuroscience, 30(39), p. 13138–13149.

Liu, J. et al. (2019) 'Mitophagy in Parkinson's Disease: From Pathogenesis to Treatment', Cells, 8(7), p. 712.

Liu, L. et al. (2014) 'Receptor-mediated mitophagy in yeast and mammalian systems', Cell Research, 24(7), p. 787–795.

Lopez-Fabuel, I. et al. (2017) 'Mitochondrial respiratory chain disorganization in Parkinson's disease-relevant PINK1 and DJ1 mutants', Neurochemistry International, 109, p. 101–105.

Lowe, J. et al. (1988) 'Ubiquitin is a common factor in intermediate filament inclusion bodies of diverse type in man, including those of Parkinson's disease, Pick's disease, and Alzheimer's disease, as well as Rosenthal fibres in cerebellar astrocytomas, cytoplasmic bodies in muscle, and mallory bodies in alcoholic liver disease', The Journal of Pathology, 155(1), p. 9–15.

Ludtmann, M. H. R. et al. (2019) 'LRRK2 deficiency induced mitochondrial Ca²⁺ efflux inhibition can be rescued by Na⁺ /Ca²⁺ /Li⁺ exchanger upregulation', *Cell Death and Disease*, 10(4), p. 265.

Macdonald, R. et al. (2018) 'Mitochondrial abnormalities in Parkinson's disease and Alzheimer's disease: can mitochondria be targeted therapeutically?', *Biochemical Society Transactions*, 46(4), p. 891–909.

Madureira, M., Connor-Robson, N. and Wade-Martins, R. (2020) "LRRK2: Autophagy and Lysosomal Activity", *Frontiers in Neuroscience*, 14, p. 498.

Martinez-Ramirez, D. et al. (2015) 'Update on deep brain stimulation in Parkinson's disease', *Translational Neurodegeneration*, 4, p. 12.

Matikainen-Ankney, B. A. et al. (2018) 'Parkinson's disease-linked Irrk2-g2019s mutation alters synaptic plasticity and promotes resilience to chronic social stress in young adulthood', *Journal of Neuroscience*, 38(45), p. 9700–9711.

Meyer, K. et al. (2014) 'Direct conversion of patient fibroblasts demonstrates non-cell autonomous toxicity of astrocytes to motor neurons in familial and sporadic ALS.',

Proceedings of the National Academy of Sciences of the United States of America, 111(2), p. 829–32.

Miklossy, J. et al. (2006) 'LRRK2 expression in normal and pathologic human brain and in human cell lines', *Journal of Neuropathology and Experimental Neurology*, 65(10), p. 953–963.

Mills, R. D. et al. (2014) 'Prediction of the Repeat Domain Structures and Impact of Parkinsonism-Associated Variations on Structure and Function of all Functional Domains of Leucine-Rich Repeat Kinase 2 (LRRK2)', *Human Mutation*, 35(4), p. 395–412.

Montgomery, E. B. (1995) 'Heavy metals and the etiology of Parkinson's disease and other movement disorders', *Toxicology*, 97(1-3), p. 3–9.

Morgada, M. N. et al. (2015) 'Loop recognition and copper-mediated disulfide reduction underpin metal site assembly of CuA in human cytochrome oxidase', *Proceedings of the National Academy of Sciences of the United States of America*, 112(38), p. 11771–11776.

Mortiboys, H. et al. (2008) 'Mitochondrial function and morphology are impaired in parkin-mutant fibroblasts.', *Annals of Neurology*, 64(5), p. 555–65.

Mortiboys, H. et al. (2010) 'Mitochondrial impairment in patients with Parkinson disease with the G2019S mutation in LRRK2', *Neurology*, 75(22), p. 2017–2020.

Mortiboys, H. et al. (2015) 'UDCA exerts beneficial effect on mitochondrial dysfunction in LRRK2 G2019S carriers and in vivo', *Neurology*, 85(10), p. 846–852.

Mortiboys, H. et al. (2018) 'Translational approaches to restoring mitochondrial function in Parkinson's disease', *FEBS Letters*, 592(5), p. 776–792.

Mortiboys, H., Aasly, J. and Bandmann, O. (2013) 'Ursocholic acid rescues mitochondrial function in common forms of familial Parkinson's disease', *Brain*, 136(10), p. 3038–3050.

Müller, T. (2015) 'Catechol-O-methyltransferase inhibitors in Parkinson's disease', *Drugs*, 75(2), p. 157–174.

Muro, C. et al. (2003) 'Comparison of the TIM and TOM channel activities of the mitochondrial protein import complexes', *Biophysical Journal*, 84(5), p. 2981–2989.

Murray, J. et al. (2003) 'The Subunit Composition of the Human NADH Dehydrogenase Obtained by Rapid One-step Immunopurification', *Journal of Biological Chemistry*, 278(16), p. 13619–13622.

Neethling, A. et al. (2019) 'Wild-type and mutant (G2019S) leucine-rich repeat kinase 2 (LRRK2) associate with subunits of the translocase of outer mitochondrial membrane (TOM) complex', *Experimental Cell Research*, 375(2), p. 72–79.

Nguyen, A. P. T. et al. (2018) 'G2019S LRRK2 enhances the neuronal transmission of tau in the mouse brain', *Human Molecular Genetics*, 27(1), p. 120–134.

Nguyen, T. N., Padman, B. S. and Lazarou, M. (2016) 'Deciphering the Molecular Signals of PINK1/Parkin Mitophagy', *Trends in Cell Biology*, 26(10), p. 733–744.

Nishijima, H. and Tomiyama, M. (2016) 'What mechanisms are responsible for the reuptake of levodopa-derived dopamine in parkinsonian striatum?', *Frontiers in Neuroscience*, 10, p. 575.

Nixon-Abell, J. et al. (2016) 'Protective LRRK2 R1398H Variant Enhances GTPase and Wnt Signaling Activity.', *Frontiers in Molecular Neuroscience*, 9, p. 18.

Osellame, L. D. et al. (2016) 'Cooperative and independent roles of the Drp1 adaptors Mff, MiD49 and MiD51 in mitochondrial fission', *Journal of Cell Science*, 129(11), p. 2170–2181.

Oughtred, R. et al. (2019) 'The BioGRID interaction database: 2019 update', *Nucleic Acids Research*, 47(D1), p. D529–D541.

De Pablo-Fernandez, E. et al. (2018) 'Association between diabetes and subsequent Parkinson disease: A record-linkage cohort study', *Neurology*, 91(2), p. e139–e142.

De Pablo-Fernández, E. et al. (2019) 'Prognosis and Neuropathologic Correlation of Clinical Subtypes of Parkinson Disease', *JAMA Neurology*, 76(4), p. 470.

Pacelli, C. et al. (2015) 'Elevated Mitochondrial Bioenergetics and Axonal Arborization Size Are Key Contributors to the Vulnerability of Dopamine Neurons', *Current Biology*, 25(18), p. 2349–2360.

Pandey, S. and Srivanitchapoom, P. (2017) 'Levodopa-induced dyskinesia: Clinical features, pathophysiology, and medical management', *Annals of Indian Academy of Neurology*, 20(3), p. 190–198.

Papa, S. et al. (2012) 'The Oxidative Phosphorylation System in Mammalian Mitochondria', *Advances in Experimental Medicine and Biology*, 942, p. 3–37.

Papadopoulou, L. C. et al. (1999) 'Fatal infantile cardioencephalomyopathy with COX deficiency and mutations in SCO2, a COX assembly gene', *Nature Genetics*, 23(3), p. 333–337.

Papkovskaia, T. D. et al. (2012) 'G2019S leucine-rich repeat kinase 2 causes uncoupling protein-mediated mitochondrial depolarization.', *Human Molecular Genetics*, 21(19), p. 4201–13.

Park, J. et al. (2006) 'Mitochondrial dysfunction in *Drosophila* PINK1 mutants is complemented by parkin.', *Nature*, 441(7097), p. 1157–61.

Park, J. S., Davis, R. L. and Sue, C. M. (2018) 'Mitochondrial Dysfunction in Parkinson's Disease: New Mechanistic Insights and Therapeutic Perspectives', *Current Neurology and Neuroscience Reports*, 18(5), p. 21.

Park, J. T. et al. (2018) 'Adjustment of the lysosomal-mitochondrial axis for control of cellular senescence', *Ageing Research Reviews*, 47, p. 176–182.

Parker Jr, W. D., Boyson, S. J. and Parks, J. K. (1989) 'Abnormalities of the electron transport chain in idiopathic parkinson's disease', *Annals of Neurology*, 26(6), p. 719–723.

Parkinson, J. (1817) *An Essay on the Shaking Palsy*. London: Sherwood, Neely and Jones.

Parkkinen, L. et al. (2011) 'Disentangling the Relationship between Lewy bodies and nigral neuronal loss in Parkinson's disease', *Journal of Parkinson's Disease*, 1(3), p. 277–286.

Passmore, J. B. et al. (2020) 'Mitochondrial fission factor (MFF) is a critical regulator of peroxisome maturation', *Biochimica et Biophysica Acta - Molecular Cell Research*, 1867(7), p. 118709.

Payne, T. et al. (2020) 'Ursodeoxycholic acid as a novel disease-modifying treatment for Parkinson's disease: Protocol for a two-centre, randomised, double-blind, placebo-controlled trial, the "UP" study', *BMJ Open*, 10(8), p. e038911.

Pham, A. N. and Waite, T. D. (2014) 'Cu(II)-catalyzed oxidation of dopamine in aqueous solutions: Mechanism and kinetics', *Journal of Inorganic Biochemistry*, 137, p. 74–84.

Postuma, R. B. et al. (2019) 'Risk and predictors of dementia and parkinsonism in idiopathic REM sleep behaviour disorder: a multicentre study', *Brain*, 142(3), p. 744–759.

Prasuhn, J. et al. (2019) 'An omics-based strategy using coenzyme Q10 in patients with Parkinson's disease: concept evaluation in a double-blind randomized placebo-controlled parallel group trial', *Neurological Research and Practice*, 1, p. 31.

Ramonet, D. et al. (2011) 'Dopaminergic Neuronal Loss, Reduced Neurite Complexity and Autophagic Abnormalities in Transgenic Mice Expressing G2019S Mutant LRRK2', *PLoS One*. 6(4), p. e18568.

Rebelo, A. P. et al. (2018) 'SCO2 mutations cause early-onset axonal Charcot-Marie-Tooth disease associated with cellular copper deficiency', *Brain*, 141(3), p. 662–672.

Reynolds, A. et al. (2014) 'LRRK2 kinase activity and biology are not uniformly predicted by its autophosphorylation and cellular phosphorylation site status', *Frontiers in Molecular Neuroscience*, 7, p. 54.

Riederer, P. et al. (1989) 'Transition Metals, Ferritin, Glutathione, and Ascorbic Acid in Parkinsonian Brains', *Journal of Neurochemistry*, 52(2), p. 515–520.

Riederer, P. and Laux, G. (2011) 'MAO-inhibitors in Parkinson's Disease', *Experimental Neurobiology*, 20(1), p. 1–17.

Rietdijk, C. D. et al. (2017) 'Exploring Braak's Hypothesis of Parkinson's Disease', *Frontiers in Neurology*, 8, p. 37.

Rivero-Ríos, P. et al. (2019) 'The G2019S variant of leucine-rich repeat kinase 2 (LRRK2) alters endolysosomal trafficking by impairing the function of the GTPase RAB8A', *Journal of Biological Chemistry*, 294(13), p. 4738–4758.

Ross, G. W. et al. (2008) 'Association of olfactory dysfunction with risk for future Parkinson's disease', *Annals of Neurology*, 63(2), p. 167–173.

Rugbjerg, K. et al. (2013) 'Exposure to estrogen and women's risk for Parkinson's disease: A prospective cohort study in Denmark', *Parkinsonism & Related Disorders*, 19(4), p. 457–460.

Ruhoy, I. S. and Saneto, R. P. (2014) 'The genetics of leigh syndrome and its implications for clinical practice and risk management', *Application of Clinical Genetics*, 7, p. 221–234.

Russo, I. (2019) 'The role of LRRK2 on PKA-NFκB pathway in microglia cells: implications for Parkinson's disease', *Neural Regeneration Research*, 14(10), p. 1713–1714.

Russo, I., Bubacco, L. and Greggio, E. (2014) 'LRRK2 and neuroinflammation: Partners in crime in Parkinson's disease?', *Journal of Neuroinflammation*, 11, p. 52.

Sánchez, E. et al. (2013) 'LYRM7/MZM1L is a UQCRC1 chaperone involved in the last steps of mitochondrial Complex III assembly in human cells', *Biochimica et Biophysica Acta (BBA) - Bioenergetics*, 1827(3), p. 285–293.

Sanders, L. H. et al. (2014) 'Mitochondrial DNA damage: Molecular marker of vulnerable nigral neurons in Parkinson's disease', *Neurobiology of Disease*, 70, p. 214–223.

Schapansky, J. et al. (2018) 'Familial knockin mutation of LRRK2 causes lysosomal dysfunction and accumulation of endogenous insoluble α -synuclein in neurons', *Neurobiology of Disease*, 111, p. 26–35.

Schapira, A. H. et al. (1989) 'Mitochondrial complex I deficiency in Parkinson's disease.', *Lancet (London, England)*, 1(8649), p. 1269.

Schildt, A. et al. (2019) 'Single inflammatory trigger leads to neuroinflammation in LRRK2 rodent model without degeneration of dopaminergic neurons', *Journal of Parkinson's Disease*, 9(1), p. 121–139.

Schlossmacher, M. G. et al. (2002) 'Parkin Localizes to the Lewy Bodies of Parkinson Disease and Dementia with Lewy Bodies', *The American Journal of Pathology*, 160(5), p. 1655–1667.

Schwab, A. J. et al. (2017) 'Decreased Sirtuin Deacetylase Activity in LRRK2 G2019S iPSC-Derived Dopaminergic Neurons', *Stem Cell Reports*, 9(6), p. 1839–1852.

Schwartzentruber, A. et al. (2020) 'Oxidative switch drives mitophagy defects in dopaminergic parkin mutant patient neurons', *Scientific Reports*, 10(1), p. 15485.

Shanley, M. R. et al. (2015) 'LRRK2 Facilitates tau Phosphorylation through Strong Interaction with tau and cdk5', *Biochemistry*, 54(33), p. 5198–5208.

Shen, C. et al. (2016) 'A ratiometric fluorescent sensor for the mitochondrial copper pool', *Metallomics*, 8(9), p. 915–919.

Sheng, Z.-H. and Cai, Q. (2012) 'Mitochondrial transport in neurons: impact on synaptic homeostasis and neurodegeneration', *Nature Reviews Neuroscience*, 13(2), p. 77–93.

Sies, H. and Jones, D. P. (2020) 'Reactive oxygen species (ROS) as pleiotropic physiological signalling agents', *Nature Reviews Molecular Cell Biology*, 21(7), p. 363–383.

Signes, A. and Fernandez-Vizarra, E. (2018) 'Assembly of mammalian oxidative phosphorylation complexes I–V and supercomplexes', *Essays in Biochemistry*, 62(3), p. 255–270.

Singh, F. et al. (2020) 'Pharmacological rescue of impaired mitophagy in Parkinson's disease-related LRRK2 G2019S knock-in mice', *bioRxiv*, p. 2020.12.07.414359.

Smith, G. A. et al. (2016) 'Fibroblast Biomarkers of Sporadic Parkinson's Disease and LRRK2 Kinase Inhibition', *Molecular Neurobiology*, 53(8), p. 5161–5177.

Soma, S. et al. (2018) 'Elesclomol restores mitochondrial function in genetic models of copper deficiency', *Proceedings of the National Academy of Sciences of the United States of America*, 115(32), p. 8161–8166.

Soman, S. et al. (2017) 'Inhibition of the mitochondrial calcium uniporter rescues dopaminergic neurons in pink1^{-/-} zebrafish', *European Journal of Neuroscience*, 45(4), p. 528–535.

Spillantini, M. G. et al. (1997) 'α-Synuclein in Lewy bodies', *Nature*, 388(6645), p. 839–840.

Stafa, K. et al. (2014) 'Functional interaction of Parkinson's disease-associated LRRK2 with members of the dynamin GTPase superfamily.', *Human Molecular Genetics*, 23(8), p. 2055–77.

De Stefani, D., Rizzuto, R. and Pozzan, T. (2016) 'Enjoy the Trip: Calcium in Mitochondria Back and Forth', *Annual Review of Biochemistry*, 85, p. 161–192.

Steger, M. et al. (2016) 'Phosphoproteomics reveals that Parkinson's disease kinase LRRK2 regulates a subset of Rab GTPases', *eLife*, 5, p. e12813.

Steger, M. et al. (2017) 'Systematic proteomic analysis of LRRK2-mediated rab GTPase phosphorylation establishes a connection to ciliogenesis', *eLife*, 6, p. e31012.

Stowe, R. L. et al. (2008) 'Dopamine agonist therapy in early Parkinson's disease', *Cochrane Database of Systematic Reviews*, (2), p. CD006564.

Su, Y.-C., Guo, X. and Qi, X. (2015) 'Threonine 56 phosphorylation of Bcl-2 is required for LRRK2 G2019S-induced mitochondrial depolarization and autophagy.', *Biochimica et Biophysica Acta*, 1852(1), p. 12–21.

Su, Y.-C. and Qi, X. (2013) 'Inhibition of excessive mitochondrial fission reduced aberrant autophagy and neuronal damage caused by LRRK2 G2019S mutation', *Human Molecular Genetics*, 22(22), p. 4545–4561.

Sun, F. et al. (2005) 'Crystal Structure of Mitochondrial Respiratory Membrane Protein Complex II', *Cell*, 121(7), p. 1043–1057.

Takahashi, K. and Yamanaka, S. (2006) 'Induction of Pluripotent Stem Cells from Mouse Embryonic and Adult Fibroblast Cultures by Defined Factors', *Cell*, 126(4), p. 663–676.

Tan, E. K. et al. (2005) 'The G2019S LRRK2 mutation is uncommon in an Asian cohort of Parkinson's disease patients', *Neuroscience Letters*, 384(3), p. 327–329.

Tang, B. L. (2015) 'MIRO GTPases in Mitochondrial Transport, Homeostasis and Pathology', *Cells*, 5(1), p. 1.

Tapiero, H., Townsend, D. M. and Tew, K. D. (2003) 'Trace elements in human physiology and pathology. Copper', *Biomedicine and Pharmacotherapy*, 57(9), p. 386–398.

Toyofuku, T. et al. (2020) 'LRRK2 regulates endoplasmic reticulum–mitochondrial tethering through the PERK -mediated ubiquitination pathway', *The EMBO Journal*, 39(2), p. e100875.

Tran-Viet, K. N. et al. (2013) 'Mutations in SCO2 are associated with autosomal-dominant high-grade myopia', *American Journal of Human Genetics*, 92(5), p. 820–826.

Tu, L. N. et al. (2016) 'Translocator protein (TSPO) affects mitochondrial fatty acid oxidation in steroidogenic cells', *Endocrinology*, 157(3), p. 1110–1121.

Tucker, E. J. et al. (2013) 'Mutations in the UQCC1-Interacting Protein, UQCC2, Cause Human Complex III Deficiency Associated with Perturbed Cytochrome b Protein Expression', *PLoS Genetics*, 9(12), p. e1004034.

Ugalde, C. et al. (2004) 'Human mitochondrial complex I assembles through the combination of evolutionary conserved modules: a framework to interpret complex I deficiencies', *Human Molecular Genetics*, 13(20), p. 2461–2472.

Umair, M. and Alfadhel, M. (2019) 'Genetic Disorders Associated with Metal Metabolism', *Cells*, 8(12), p. 1598.

Uo, T. et al. (2009) 'Drp1 levels constitutively regulate mitochondrial dynamics and cell survival in cortical neurons', *Experimental Neurology*, 218(2), p. 274–285.

Vincent, A. et al. (2012) 'parkin-induced defects in neurophysiology and locomotion are generated by metabolic dysfunction and not oxidative stress', *Human Molecular Genetics*, 21(8), p. 1760–1769.

Wakabayashi, K. et al. (2013) 'The Lewy Body in Parkinson's Disease and Related Neurodegenerative Disorders', *Molecular Neurobiology*, 47(2), p. 495–508.

Wallings, R., Manzoni, C. and Bandopadhyay, R. (2015) 'Cellular processes associated with LRRK2 function and dysfunction.', *The FEBS Journal*, 282(15), p. 2806–26.

Wang, C. and Youle, R. J. (2009) 'The role of mitochondria in apoptosis', *Annual Review of Genetics*, 43, p. 95–118.

Wang, H. et al. (2011) 'Parkin Ubiquitinates Drp1 for Proteasome-dependent Degradation', *Journal of Biological Chemistry*, 286(13), p. 11649–11658.

Wang, X. et al. (2010) 'Copper binding regulates intracellular alpha-synuclein localisation, aggregation and toxicity', *Journal of Neurochemistry*, 113(3), p. 704–714.

Wang, X. et al. (2011) 'PINK1 and Parkin Target Miro for Phosphorylation and Degradation to Arrest Mitochondrial Motility', *Cell*, 147(4), p. 893–906.

Wang, X. et al. (2012) 'LRRK2 regulates mitochondrial dynamics and function through direct interaction with DLP1.', *Human Molecular Genetics*, 21(9), p. 1931–44.

Warren, P. J., Earl, C. J. and Thompson, R. H. S. (1960) 'THE DISTRIBUTION OF COPPER IN HUMAN BRAIN', *Brain*, 83(4), p. 709–717.

Wauters, F. et al. (2020) 'LRRK2 mutations impair depolarization-induced mitophagy through inhibition of mitochondrial accumulation of RAB10', *Autophagy*, 16(2), p. 203–222.

Weindel CG, Bell SL, Vail KJ, West KO, Patrick KL, Watson RO (2020). LRRK2 maintains mitochondrial homeostasis and regulates innate immune responses to *Mycobacterium tuberculosis*. *eLife*. 9, p. e51071.

Weiskirchen, S., Kim, P. and Weiskirchen, R. (2019) 'Determination of copper poisoning in Wilson's disease using laser ablation inductively coupled plasma mass spectrometry', *Annals of Translational Medicine*, 7(Suppl 2), p. S72.

Westermann, B. (2010) 'Mitochondrial fusion and fission in cell life and death', *Nature Reviews Molecular Cell Biology*, 11(12), p. 872–884.

Weykopf, B. et al. (2019) 'Induced pluripotent stem cell-based modeling of mutant LRRK2-associated Parkinson's disease', *European Journal of Neuroscience*, 49(4), p. 561–589.

Wiemerslage, L., Ismael, S. and Lee, D. (2016) 'Early alterations of mitochondrial morphology in dopaminergic neurons from Parkinson's disease-like pathology and time-dependent neuroprotection with D2 receptor activation', *Mitochondrion*, 30, p. 138–147.

Williams, C. L. et al. (2019) 'Measuring intracellular metal concentration via ICP-MS following copper exposure', *Methods in Molecular Biology*, 1946, p. 195–205.

Wojtovich, A. P. et al. (2013) 'Physiological consequences of complex II inhibition for aging, disease, and the mKATP channel.', *Biochimica et Biophysica Acta*, 1827(5), p. 598–611.

Wooten, G. F. et al. (2004) 'Are men at greater risk for Parkinson's disease than women?', *Journal of Neurology, Neurosurgery & Psychiatry*, 75(4), p. 637–639.

Xie, L., Shi, F., Li, Y. et al. (2020) 'Drp1-dependent remodeling of mitochondrial morphology triggered by EBV-LMP1 increases cisplatin resistance', *Signal Transduction and Targeted Therapy*, 5(1), p. 56.

Yakes, F. M. and Van Houten, B. (1997) 'Mitochondrial DNA damage is more extensive and persists longer than nuclear DNA damage in human cells following oxidative stress.', *Proceedings of the National Academy of Sciences of the United States of America*, 94(2), p. 514–9.

Yakhine-Diop, S. M. S. et al. (2014) 'G2019S LRRK2 mutant fibroblasts from Parkinson's disease patients show increased sensitivity to neurotoxin 1-methyl-4-phenylpyridinium dependent of autophagy.', *Toxicology*, 324, p. 1–9.

Yakhine-Diop, S. M. S. et al. (2019) 'Impaired Mitophagy and Protein Acetylation Levels in Fibroblasts from Parkinson's Disease Patients', *Molecular Neurobiology*, 56(4), p. 2466–2481.

Yang, H. et al. (2010) 'Analysis of mouse models of cytochrome c oxidase deficiency owing to mutations in Sco2', *Human Molecular Genetics*, 19(1), p. 170–180.

Ye, Q. et al. (2016) 'Overexpression of PGC-1 α Influences Mitochondrial Signal Transduction of Dopaminergic Neurons', *Molecular Neurobiology*, 53(6), p. 3756–3770.

Yeow, J. et al. (2014) 'A novel flavin derivative reveals the impact of glucose on oxidative stress in adipocytes', *Chemical Communications*, 50(60), p. 8181–8184.

Youle, R. J. and Narendra, D. P. (2011) 'Mechanisms of mitophagy', *Nature Reviews Molecular Cell Biology*, 12(1), p. 9–14.

Yue, M. et al. (2015) 'Progressive dopaminergic alterations and mitochondrial abnormalities in LRRK2 G2019S knock-in mice.', *Neurobiology of Disease*, 78, p. 172–95.

Zheng, X. et al. (2016) 'Metabolic reprogramming during neuronal differentiation from aerobic glycolysis to neuronal oxidative phosphorylation', *eLife*, 5, p. e13374.

Zhu, P. P. et al. (2004) 'Intra- and intermolecular domain interactions of the C-terminal GTPase effector domain of the multimeric dynamin-like GTPase Drp1', *Journal of Biological Chemistry*, 279, p. 35967–74.

Zimprich, A. et al. (2004) 'Mutations in LRRK2 cause autosomal-dominant parkinsonism with pleomorphic pathology', *Neuron*, 44(4), p. 601–607.

Zorov, D. B., Juhaszova, M. and Sollott, S. J. (2014) 'Mitochondrial reactive oxygen species (ROS) and ROS-induced ROS release', *Physiological Reviews*, 94(3), p. 909–950.

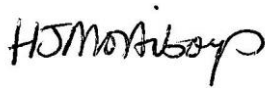
Appendix A

Permission to use article content in PhD thesis

I hereby consent for Ruby Macdonald to use text extracts from the following article in their PhD thesis:

Mortiboys, H., Macdonald, R., Payne, T., Sassani, M., Jenkins, T. and Bandmann, O. (2018) 'Translational approaches to restoring mitochondrial function in Parkinson's disease', *FEBS Letters*, pp. 776–792.

This thesis will be available in print and an electronic copy deposited in the White Rose eTheses Online repository.



Dr Heather Mortiboys



Ruby Macdonald



Dr Thomas Payne



Dr Thomas Jenkins



Dr Matilde Sassani



Professor Oliver Bandmann

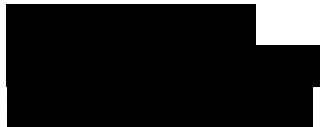
JOHN WILEY AND SONS LICENSE
TERMS AND CONDITIONS

Jun 11, 2021

This Agreement between Ruby Macdonald ("You") and John Wiley and Sons ("John Wiley and Sons") consists of your license details and the terms and conditions provided by John Wiley and Sons and Copyright Clearance Center.

| | |
|---------------------------------|---|
| License Number | 5067510928371 |
| License date | May 14, 2021 |
| Licensed Content Publisher | John Wiley and Sons |
| Licensed Content Publication | FEBS Letters |
| Licensed Content Title | Translational approaches to restoring mitochondrial function in Parkinson's disease |
| Licensed Content Author | Heather Mortiboys, Ruby Macdonald, Thomas Payne, et al |
| Licensed Content Date | Dec 17, 2017 |
| Licensed Content Volume | 592 |
| Licensed Content Issue | 5 |
| Licensed Content Pages | 17 |
| Type of use | Dissertation/Thesis |
| Requestor type | Author of this Wiley article |
| Format | Print and electronic |
| Portion | Text extract |
| Number of Pages | 4 |
| Will you be translating? | No |
| Title | Mitochondrial dysfunction in LRRK2 G2019S Parkinson's disease |
| Institution name | University of Sheffield |
| Expected presentation date | Dec 2020 |
| Order reference number | 1 |
| Portions | Text under the heading 'Experimental evidence for mitochondrial dysfunction in PD' |

Requestor Location



Publisher Tax ID

EU826007151

Total

0.00 GBP

Terms and Conditions

TERMS AND CONDITIONS

This copyrighted material is owned by or exclusively licensed to John Wiley & Sons, Inc. or one of its group companies (each a "Wiley Company") or handled on behalf of a society with which a Wiley Company has exclusive publishing rights in relation to a particular work (collectively "WILEY"). By clicking "accept" in connection with completing this licensing transaction, you agree that the following terms and conditions apply to this transaction (along with the billing and payment terms and conditions established by the Copyright Clearance Center Inc., ("CCC's Billing and Payment terms and conditions"), at the time that you opened your RightsLink account (these are available at any time at <http://myaccount.copyright.com>).

Terms and Conditions

- The materials you have requested permission to reproduce or reuse (the "Wiley Materials") are protected by copyright.
- You are hereby granted a personal, non-exclusive, non-sub licensable (on a stand-alone basis), non-transferable, worldwide, limited license to reproduce the Wiley Materials for the purpose specified in the licensing process. This license, **and any CONTENT (PDF or image file) purchased as part of your order**, is for a one-time use only and limited to any maximum distribution number specified in the license. The first instance of republication or reuse granted by this license must be completed within two years of the date of the grant of this license (although copies prepared before the end date may be distributed thereafter). The Wiley Materials shall not be used in any other manner or for any other purpose, beyond what is granted in the license. Permission is granted subject to an appropriate acknowledgement given to the author,

title of the material/book/journal and the publisher. You shall also duplicate the copyright notice that appears in the Wiley publication in your use of the Wiley Material. Permission is also granted on the understanding that nowhere in the text is a previously published source acknowledged for all or part of this Wiley Material. Any third party content is expressly excluded from this permission.

- With respect to the Wiley Materials, all rights are reserved. Except as expressly granted by the terms of the license, no part of the Wiley Materials may be copied, modified, adapted (except for minor reformatting required by the new Publication), translated, reproduced, transferred or distributed, in any form or by any means, and no derivative works may be made based on the Wiley Materials without the prior permission of the respective copyright owner. **For STM Signatory Publishers clearing permission under the terms of the [STM Permissions Guidelines](#) only, the terms of the license are extended to include subsequent editions and for editions in other languages, provided such editions are for the work as a whole in situ and does not involve the separate exploitation of the permitted figures or extracts,** You may not alter, remove or suppress in any manner any copyright, trademark or other notices displayed by the Wiley Materials. You may not license, rent, sell, loan, lease, pledge, offer as security, transfer or assign the Wiley Materials on a stand-alone basis, or any of the rights granted to you hereunder to any other person.
- The Wiley Materials and all of the intellectual property rights therein shall at all times remain the exclusive property of John Wiley & Sons Inc, the Wiley Companies, or their respective licensors, and your interest therein is only that of having possession of and the right to reproduce the Wiley Materials pursuant to Section 2 herein during the continuance of this Agreement. You agree that you own no right, title or interest in or to the Wiley Materials or any of the intellectual property rights therein. You shall have no rights hereunder other than the license as provided for above in Section 2. No right, license or interest to any trademark, trade name, service mark or other branding ("Marks") of WILEY or its licensors is granted hereunder, and you agree that you shall not assert any such right, license or interest with respect thereto
- NEITHER WILEY NOR ITS LICENSORS MAKES ANY WARRANTY OR REPRESENTATION OF ANY KIND TO YOU OR ANY THIRD PARTY, EXPRESS, IMPLIED OR STATUTORY, WITH RESPECT TO

THE MATERIALS OR THE ACCURACY OF ANY INFORMATION CONTAINED IN THE MATERIALS, INCLUDING, WITHOUT LIMITATION, ANY IMPLIED WARRANTY OF MERCHANTABILITY, ACCURACY, SATISFACTORY QUALITY, FITNESS FOR A PARTICULAR PURPOSE, USABILITY, INTEGRATION OR NON-INFRINGEMENT AND ALL SUCH WARRANTIES ARE HEREBY EXCLUDED BY WILEY AND ITS LICENSORS AND WAIVED BY YOU.

- WILEY shall have the right to terminate this Agreement immediately upon breach of this Agreement by you.
- You shall indemnify, defend and hold harmless WILEY, its Licensors and their respective directors, officers, agents and employees, from and against any actual or threatened claims, demands, causes of action or proceedings arising from any breach of this Agreement by you.
- IN NO EVENT SHALL WILEY OR ITS LICENSORS BE LIABLE TO YOU OR ANY OTHER PARTY OR ANY OTHER PERSON OR ENTITY FOR ANY SPECIAL, CONSEQUENTIAL, INCIDENTAL, INDIRECT, EXEMPLARY OR PUNITIVE DAMAGES, HOWEVER CAUSED, ARISING OUT OF OR IN CONNECTION WITH THE DOWNLOADING, PROVISIONING, VIEWING OR USE OF THE MATERIALS REGARDLESS OF THE FORM OF ACTION, WHETHER FOR BREACH OF CONTRACT, BREACH OF WARRANTY, TORT, NEGLIGENCE, INFRINGEMENT OR OTHERWISE (INCLUDING, WITHOUT LIMITATION, DAMAGES BASED ON LOSS OF PROFITS, DATA, FILES, USE, BUSINESS OPPORTUNITY OR CLAIMS OF THIRD PARTIES), AND WHETHER OR NOT THE PARTY HAS BEEN ADVISED OF THE POSSIBILITY OF SUCH DAMAGES. THIS LIMITATION SHALL APPLY NOTWITHSTANDING ANY FAILURE OF ESSENTIAL PURPOSE OF ANY LIMITED REMEDY PROVIDED HEREIN.
- Should any provision of this Agreement be held by a court of competent jurisdiction to be illegal, invalid, or unenforceable, that provision shall be deemed amended to achieve as nearly as possible the same economic effect as the original provision, and the legality, validity and enforceability of the remaining provisions of this Agreement shall not be affected or impaired thereby.

- The failure of either party to enforce any term or condition of this Agreement shall not constitute a waiver of either party's right to enforce each and every term and condition of this Agreement. No breach under this agreement shall be deemed waived or excused by either party unless such waiver or consent is in writing signed by the party granting such waiver or consent. The waiver by or consent of a party to a breach of any provision of this Agreement shall not operate or be construed as a waiver of or consent to any other or subsequent breach by such other party.
- This Agreement may not be assigned (including by operation of law or otherwise) by you without WILEY's prior written consent.
- Any fee required for this permission shall be non-refundable after thirty (30) days from receipt by the CCC.
- These terms and conditions together with CCC's Billing and Payment terms and conditions (which are incorporated herein) form the entire agreement between you and WILEY concerning this licensing transaction and (in the absence of fraud) supersedes all prior agreements and representations of the parties, oral or written. This Agreement may not be amended except in writing signed by both parties. This Agreement shall be binding upon and inure to the benefit of the parties' successors, legal representatives, and authorized assigns.
- In the event of any conflict between your obligations established by these terms and conditions and those established by CCC's Billing and Payment terms and conditions, these terms and conditions shall prevail.
- WILEY expressly reserves all rights not specifically granted in the combination of (i) the license details provided by you and accepted in the course of this licensing transaction, (ii) these terms and conditions and (iii) CCC's Billing and Payment terms and conditions.
- This Agreement will be void if the Type of Use, Format, Circulation, or Requestor Type was misrepresented during the licensing process.
- This Agreement shall be governed by and construed in accordance with the laws of the State of New York, USA, without regards to such state's conflict of law rules. Any legal action, suit or proceeding arising out of or relating to these Terms and Conditions or the breach thereof shall be instituted in a court of competent jurisdiction in New York County in the State of New York in the United States of America and each party hereby

consents and submits to the personal jurisdiction of such court, waives any objection to venue in such court and consents to service of process by registered or certified mail, return receipt requested, at the last known address of such party.

WILEY OPEN ACCESS TERMS AND CONDITIONS

Wiley Publishes Open Access Articles in fully Open Access Journals and in Subscription journals offering Online Open. Although most of the fully Open Access journals publish open access articles under the terms of the Creative Commons Attribution (CC BY) License only, the subscription journals and a few of the Open Access Journals offer a choice of Creative Commons Licenses. The license type is clearly identified on the article.

The Creative Commons Attribution License

The [Creative Commons Attribution License \(CC-BY\)](#) allows users to copy, distribute and transmit an article, adapt the article and make commercial use of the article. The CC-BY license permits commercial and non-

Creative Commons Attribution Non-Commercial License

The [Creative Commons Attribution Non-Commercial \(CC-BY-NC\) License](#) permits use, distribution and reproduction in any medium, provided the original work is properly cited and is not used for commercial purposes.(see below)

Creative Commons Attribution-Non-Commercial-NoDerivs License

The [Creative Commons Attribution Non-Commercial-NoDerivs License](#) (CC-BY-NC-ND) permits use, distribution and reproduction in any medium, provided the original work is properly cited, is not used for commercial purposes and no modifications or adaptations are made. (see below)

Use by commercial "for-profit" organizations

Use of Wiley Open Access articles for commercial, promotional, or marketing purposes requires further explicit permission from Wiley and will be subject to a fee.

Further details can be found on Wiley Online
Library <http://olabout.wiley.com/WileyCDA/Section/id-410895.html>

Other Terms and Conditions:

v1.10 Last updated September 2015

Questions? customercare@copyright.com or +1-855-239-3415 (toll free in the US) or +1-978-646-2777.

Appendix B

Table 1. Summary table of individual assay results of LRRK2-G2019S manifesting and non-manifesting fibroblasts from Chapters 3 and 5. Data are presented as mean \pm SD. Control data is the combined data of all control cell lines for that assay. Each cell marked orange is representative of the mean of the individual cell line being lower than the mean of the controls of the same assay, while each cell marked in green has a higher mean value than the mean of the controls. The assays tabulated in this graph are ATP levels (Figure 3.1a), MMP short mitos (Figure 3.2c), Mito ROS (Figure 3.3c), Cyto ROS (Figure 3.4b), TSPO protein expression (Figure 3.13b), complex IV subunit protein expression (Figure 3.5b), BCS1L protein expression (Figure 3.6b), SCO2 protein expression (Figure 3.7b), COX15 protein expression, Mito copper probe intensity (Figure 5.5b), and Cyto copper probe intensity (Figure 5.8b). C, control; M, LRRK2-G2019S manifesting; NM, LRRK2-G2019S non-manifesting; gal, galactose; MMP, mitochondrial membrane potential; mito, mitochondria; cyto, cytoplasmic; ROS, reactive oxygen species.

| | Disease status | ATP (gal) | MMP (short mito gal) | Mito ROS (FRR2) | Cyto ROS | TSPO | Complex IV | BCS1L | SCO2 | COX15 | Mito copper | Cyto copper |
|-----------------|----------------|-----------|----------------------|-----------------|----------|--------|------------|--------|--------|--------|-------------|-------------|
| Controls | C | 120±22 | 97±2 | 100 | 100 | 98±17 | 98±26 | 99±7 | 100±12 | 111±26 | 100 | 100 |
| TRD03 | M | - | - | - | - | 102±65 | 35±12 | 95±69 | 49±11 | - | - | - |
| TRD04 | M | - | - | 113±9 | 102±1 | 137±89 | 86±31 | 44±24 | 55±24 | 62±10 | - | 118±17 |
| TRD07 | M | - | - | 107±19 | 100±0 | 68±13 | 82±34 | 104±52 | 60±9 | 25±27 | - | 90±5 |
| TRD11 | M | - | - | - | - | 86±48 | 69±41 | 154±55 | 37±16 | - | - | - |
| NPFC-008 | M | - | - | 103±11 | 95±3 | 122±61 | 74±36 | 137±69 | 20±8 | 62±33 | 102±3 | 81±4 |
| NPFC-028 (M2) | M | 114±15 | 105±4 | 69±24 | - | 93±18 | 103±73 | 117±66 | 131±28 | - | 84±12 | - |
| NPFC-071 (M1) | M | 84±18 | 129±15 | 89±3 | - | 92±11 | 85±8 | 106±50 | 83±29 | - | - | - |
| ND34198 | M | - | - | 124±4 | 101±1 | - | - | - | - | - | 104±4 | - |
| TRD05 | NIM | - | - | - | - | - | 69±15 | 84±29 | 108±4 | - | - | - |
| TRD12 | NIM | - | - | - | - | 57±31 | 71±41 | 93±42 | 97±22 | 68±25 | - | - |
| NPFC-005 | NIM | - | - | - | - | 148±28 | 93±36 | 88±35 | 201±22 | - | - | - |
| NPFC-025 | NIM | - | - | 106±9 | 96±4 | - | - | - | - | - | 96±6 | 92±3 |
| NPFC-046 (NIM3) | NIM | 112±21 | 100±5 | 73±12 | - | 82±12 | 120±37 | 101±3 | 104±41 | - | 88±5 | - |
| NPFC-048 (NIM2) | NIM | 107±14 | 118±10 | - | - | - | - | - | - | - | - | - |
| NPFC-061 (NIM1) | NIM | 126±25 | 97±7 | 84±7 | - | - | 134±55 | 69±48 | 193±52 | - | - | - |
| NPFC-068 (NIM4) | NIM | 54±37 | 100±5 | 94±9 | 102±0 | 87±5 | 86±50 | 102±37 | 107±3 | 19±22 | - | 117±22 |

Table 2. Summary table of individual mitochondrial morphology assay results of LRRK2-G2019S manifesting and non-manifesting fibroblasts from Chapters 3 and 5.

Data are presented as mean \pm SD. Control data is the combined data of all control cell lines for that assay. Each cell marked orange is representative of the mean of the individual cell line being lower than the mean of the controls of the same assay, while each cell marked in green has a higher mean value than the mean of the controls. The assays tabulated in this graph are normalised mito area (Figure 3.8c), normalised mito count (Figure 3.8a), normalised % perinuclear mitos (Figure 3.8b), normalised % short mitos (Figure 3.8d), OPA1 upper and lower band protein expression (Figure 3.9b), DRP1 subunit protein expression (Figure 3.10b), and normalised DRP1 spots in mitos per total number of DRP1 spots (Figure 3.12b). C, control; M, LRRK2-G2019S manifesting; NM, LRRK2-G2019S non-manifesting; gal, galactose; mitos, mitochondria.

| Number | Disease status | Mito area (gal) | Mito count (gal) | Perinuclear mitos (gal) | Short mitos (gal) | OPA1 upper band | OPA1 lower band | DRP1 | DRP1 spots in mitos (gal) |
|----------------|----------------|-----------------|------------------|-------------------------|-------------------|-----------------|-----------------|--------|---------------------------|
| Controls | C | 104±2 | 98±6 | 93±2 | 97±3 | 101±15 | 102±15 | 96±33 | 101±2 |
| TRD03 | M | - | - | - | - | 132±35 | 64±39 | 118±60 | - |
| TRD04 | M | - | - | - | - | 106±33 | 82±30 | 94±38 | 109±1 |
| TRD07 | M | - | - | - | - | 106±62 | 190±129 | 50±18 | - |
| TRD11 | M | - | - | - | - | 46±16 | 30±18 | 109±41 | - |
| NPFC-008 | M | - | - | - | - | 131±77 | 183±93 | 91±24 | 104±7 |
| NPFC-028 (M2) | M | 94±17 | 111±22 | 105±13 | 88±3 | 94±54 | 84±28 | 49±23 | - |
| NPFC-071 (M1) | M | 79±8 | 115±8 | 125±13 | 121±10 | 147±42 | 126±45 | 107±58 | 96±4 |
| ND34198 | M | - | - | - | - | - | - | - | - |
| TRD05 | NM | - | - | - | - | 125±20 | 88±18 | 133±55 | - |
| TRD12 | NM | - | - | - | - | 94±42 | 90±46 | 79±26 | - |
| NPFC-005 | NM | - | - | - | - | 137±40 | 79±15 | 35±25 | - |
| NPFC-025 | NM | - | - | - | - | - | - | - | 104±1 |
| NPFC-046 (NM3) | NM | 96±14 | 117±19 | 116±13 | 94±4 | 96±41 | 115±59 | 23±26 | - |
| NPFC-048 (NM2) | NM | 76±22 | 112±20 | 128±23 | 115±13 | - | - | - | - |
| NPFC-061 (NM1) | NM | 98±14 | 110±18 | 122±31 | 97±3 | 77±20 | 135±89 | 46±20 | 100±1 |
| NPFC-068 (NM4) | NM | 91±8 | 117±15 | 112±13 | 103±5 | 153±67 | 135±54 | 52±16 | 101±7 |